UNIVERSITY OF CALIFORNIA

Los Angeles

Simulation of Charge Generation and Transport in Semiconductors Under Energetic Particle Bombardment

A dissertation submitted in partial satisfaction

of the requirements for the degree

Doctor of Philosophy in Engineering

by

Rodger Carl Martin

1990

© Copyright by

Rodger Martin

1990

The dissertation of Rodger Carl Martin is approved.

Mohamed A. Abdou

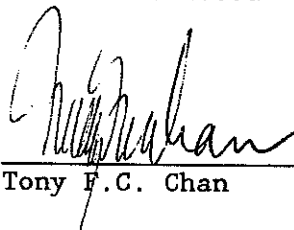

Tony F.C. Chan

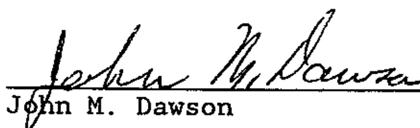

John M. Dawson

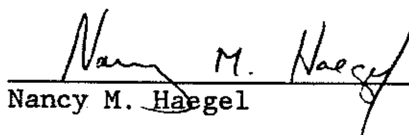

Nancy M. Haegel

Nasr M. Ghoniem, Committee Chair

University of California, Los Angeles

1990

Dedication

This dissertation is dedicated
to my mother, Anna Gantz Martin,
who supported me although she never understood,
and to my wife, Madhavi Zope Martin,
who supported me because she understood.

TABLE OF CONTENTS

Dedication iii

List of Figures viii

List of Tables xiv

List of Symbols xv

Acknowledgements xix

Vita xx

Abstract xxiii

1 Introduction 1

2 Space Radiation Effects on Microelectronic Systems 7

2.1 The Space Radiation Environment 7

2.2 The Single Event Upset Phenomenon 10

2.3 Technological Features and Radiation Hardening 13

2.4 References 17

3 Review of Theoretical and Experimental Studies of Single Event Upsets 20

3.1 Modeling of the Charge Track 20

3.2 Charge Transport Modeling 22

3.2.1 Analytical Models 22

3.2.2 Computational Models 25

3.3 Limitations of Previous Models 27

3.4 Experimental Efforts 29

3.5 Effects of External Circuit 31

3.6 References 31

4 Ion Track Formation Model **34**

4.1 Introduction 34

4.2 Mechanisms of Ion Track Formation 35

4.2.1 Electronic Energy Loss 35

4.2.2 Elastic Scattering 37

4.2.3 Core Electron Ionization 41

4.2.4 Dielectric Energy Losses 43

4.2.5 Higher-Energy Electron Transport 44

4.3 Modeling Methodology 44

4.4 Results 56

4.4.1 Secondary Electron Distributions 56

4.4.2 Electron-Hole Pair Distributions 59

4.5 Conclusions 69

4.6 References 70

5 Transport of Electron-Hole Pairs **73**

5.1 Introduction to Semiconductor Device Modeling 73

5.2 Introduction to the Hybrid Finite Element/Particle Simulation Method 74

5.3 The Finite Element Solution to Poisson's Equation . . 77

5.3.1 The Finite Element Formulation 77

5.3.2 Solution Methods for Systems of Linear Equations 87
5.4 The Particle Simulation Method 90
5.4.1 Introduction 90
5.4.2 Formulation of the Method 92
5.4.3 Particle Transport 94
5.5 The Combined Finite Element/Particle Simulation Method 100
5.5.1 Computational Considerations 100
5.5.2 Summary of Potential Advantages of the FE/PS Method 107
5.6 References 109

6 Assessment of the Finite Element/Particle Simulation Method 113

6.1 Introduction 113
6.2 One-Dimensional Comparison with Analytical Potential Profiles 113
6.3 One-Dimensional Comparison with an Iterative Self-Consistent Finite Element Code 119
6.4 Current-Voltage Characteristics 127
6.5 Three-Dimensional Potential and Density Profiles . . 130
6.6 Summary 137
6.7 References 138

7 Numerical Simulation of Single Event Upsets **140**

7.1 Comparison with Previous Single Event Upset Simulations 140

7.2 Effect of Time Step on Charge Collection 152

7.3 Modeling of the Transient Current Pulse 153

7.4 Effects of Track Structure 159

7.5 Simulation of Alpha Particle Effects 164

7.6 References 167

8 Summary and Conclusions **168**

LIST OF FIGURES

2.1 Differential cosmic ray flux for protons, helium, carbon, oxygen, and iron nuclei for solar minimum [2.7] 9

2.2 Estimate of the daily upset rate per kilobit as a function of critical charge, for several groups of cosmic ray elements [2.8] 13

2.3 Critical charge for single event upset as a function of device feature size for several device technologies [2.12] 17

4.1 Flowchart of electron slowing-down interactions 38

4.2 Relative cross section for energy transfer 46

4.3 Cumulative distribution functions as a function of the cutoff energy for secondary electron generation, for an incident 270 MeV krypton ion 49

4.4 Flowchart for secondary electron generation within the ion transport code TRIPOS-E 50

4.5 Dielectric loss function for silicon [4.24] 53

4.6 Comparison of electron mean-range formulations in silicon . 55

4.7 Two-dimensional profile of secondary electron ranges in silicon as a function of track depth for (a) 100 MeV proton, (b) 180 MeV argon, and (c) 270 MeV krypton ions . . 57

4.8 Radial volumetric charge density in silicon due to high-energy secondary electrons using T_{cut} = 1000 eV for (a) 270 MeV krypton, (b) 180 MeV argon, and (c) 1 GeV iron ions 60

4.9 270 MeV krypton ion incident on silicon, at 5 μm depth, using T_{cut} = 1000 eV: (a) radial charge surface density due to high-energy secondary electrons, obtained from TRIPOS-E; (b) comparison of the analytical formula to the computational results 64

4.10 Radial volumetric charge-density profiles as a function of depth for 270 MeV krypton ion, given by the analytical formula, equation (4.39) 65

4.11 Track width parameters for different cutoff energies, at depths of 5 and 10 μm for (a) 270 MeV krypton, and (b) 180 MeV argon ions 67

5.1 Area coordinates for linear triangular elements [5.7] . . . 80

5.2 Linear triangular elements in finite element analysis, showing (a) the element and its nodes, and (b) the linear shape function for each node [5.17] 81

5.3 Quadratic triangular elements in finite element analysis, showing (a) the element and its nodes, and (b) the quadratic shape function for each node [5.17] 82

5.4 Cloud-in-cell charge assignment for linear two-dimensional weighting [5.30] 92

5.5 Flowchart for the finite element/particle simulation code 101

6.1 Axisymmetric 1-D device geometry showing geometry of the open-circuit silicon diode 115

6.2 Comparison of calculated potential profiles to analytical results 116

6.3 Calculated potential profile across open-circuit p-n junction, with 10^{15} cm^{-3} doping, for (a) 5 μm device (0.31 μm elements), and (b) 1.2 μm device (0.08 μm elements) . . 117
6.4 Dependence of the relative average radial error in the electric field on grid size and axial distance across the 2.5 μm device 118
6.5 Comparison of calculated potential profile to self-consistent finite element results 120
6.6 Evolution of density and potential profiles with time, after applying 3 volts reverse-bias to a 6 μm long, 1-D silicon diode 122
6.7 Effect of grid element size (in μm) on steady-state profiles 124
6.8 Steady-state profiles for 3-volt reverse-bias, 5 μm silicon diode with n^+ doping of 10^{17} cm^{-3} and p doping of 10^{15} cm^{-3} 126
6.9 Comparison of calculated current-voltage characteristics of a 6 μm silicon diode to the self-consistent FE code results 129
6.10 Axisymmetric 3-D device simulation showing geometry of the reverse-biased silicon diode 131
6.11 Axisymmetric 3-D device simulation at steady-state showing (a) potential, (b) electron, and (c) hole profiles 133
6.12 Contour plots for axisymmetric 3-D device simulation at steady-state showing (a) potential, (b) electron, and (c) hole profiles 134

6.13 Steady-state profiles from Kreskovsky and Grubin 3-D simulation [6.5], showing (a) 3-D potential profile, and contour plots for (b) potential, (c) electron, and (d) hole profiles 135

6.14 Reduction in relative computational error as a function of the element size 137

7.1 Evolution of 3-D electron profile with time after introduction of ion track at t = 0 141

7.2 Evolution of electron density contours with time, similar to Figure 7.1 142

7.3 Evolution of 3-D potential profile with time after introduction of ion track 144

7.4 Contour plots of potential profile evolution with time, similar to Figure 7.3 145

7.5 Evolution of 3-D potential profile with time for Kreskovsky and Grubin simulation [7.1] 147

7.6 Integrated collection of track charge at n^+-contact vs. time for electrons (n) and holes (p) 148

7.7 Integrated collection of track charge at ground contact vs. time for electrons (n) and holes (p) 148

7.8 Integrated collection of track electron charge at n^+-contact vs. time for (a) 3-D simulation [7.1], (b) axisymmetric 3-D FE/PS simulation, and (c) 2-D simulation [7.1] 149

7.9 Track electron current at n^+-contact vs. time for (a) 3-D simulation [7.1], (b) axisymmetric 3-D FE/PS simulation, and (c) 2-D simulation [7.1] 149

7.10 Integrated collection of track electron charge at n^+-contact vs. time for time steps of 0.05 ps, 0.10 ps, 0.20 ps, 0.40 ps, and 0.80 ps 154

7.11 Maximum and minimum potential values as a function of time step for simulations of Figure 7.10 154

7.12 Comparison of results for integrated collection of track electron charge at n^+-contact vs. time, from (a) computational results, (b) radioactive decay model [7.8], and (c) Messenger model [7.7] 157

7.13 Comparison of results for electron current at n^+-contact vs. time, using (a) radioactive decay model [7.8], and (b) Messenger model [7.7] 157

7.14 Integrated collection of track electron charge (n) and hole charge (p) at n^+-contact vs. time, for uniform track densities of (a) 10^{18} cm^{-3}, (b) 10^{19} cm^{-3}, and (c) 10^{20} cm^{-3} 160

7.15 Fraction of total track charge collected at n^+-contact vs. time, for uniform track densities of (a) 10^{18} cm^{-3}, (b) 10^{19} cm^{-3}, and (c) 10^{20} cm^{-3} 163

7.16 Fraction of total track charge recombined vs. time, for uniform track densities of (a) 10^{18} cm^{-3}, (b) 10^{19} cm^{-3}, and (c) 10^{20} cm^{-3} 163

7.17 Track electron current vs. time at n^+-contact for 5 MeV alpha particle 166

7.18 Experimental current pulses from 5 MeV alpha particle [7.10] 166

LIST OF TABLES

4.1 Analytical track parameters for different cutoff energies . 68

4.2 Analytical track parameters at several depths 68

5.1 Constants used in mobility calculations [5.40] 98

7.1 Comparison of FE/PS simulation results with experimental results for 5 MeV alpha particles 165

LIST OF SYMBOLS

a,b	constants used in equations (5.25) and (5.29)
A,B	constants used in equation (5.27)
cdf	cumulative distribution function
CMOS	complementary metal-oxide-semiconductor
$c_n(c_p)$	Auger electron (hole) recombination coefficient ($cm^6\ s^{-1}$)
cpu	central processing unit
$d_a(d_d)$	spatial extent of the depletion zone from an abrupt p-n junction into the acceptor (donor) doping region
$D_n(D_p)$	electron (hole) diffusivity ($cm^2\ s^{-1}$)
DRAM	dynamic random access memory
$\vec{E}$	electric field ($V\ cm^{-1}$)
E_c	electric field parameter used in equation (5.29) ($V\ cm^{-1}$)
EDAC	error detection and correction
e-h	electron-hole
FD	finite difference
FE	finite element
FE/PS	finite element/particle simulation
FFT	fast Fourier transform
G	carrier generation rate ($cm^{-3}\ s^{-1}$)
G_α	ion track generation rate ($cm^{-3}\ s^{-1}$)
h	computational cell size (cm)
IC	integrated circuit
IMSL	International Mathematical and Statistical Libraries, Inc.
I^2L	integrated injection logic

I_o	maximum transient current from the ion track (mA)
I_t	transient current from the ion track (mA)
I-V	current-voltage
$\vec{J}_n(\vec{J}_p)$	electron (hole) current density (A cm^{-2})
LET	linear energy transfer (MeV/μm)
L_i	local shape function at node i
$L_n(L_p)$	electron (hole) diffusion lengths
M	number of nodes in the computational mesh
MBU	multiple-bit upset
MC	Monte Carlo
MOS	metal-oxide-semiconductor
n	electron carrier density (cm^{-3})
n^+	heavily-doped n-type semiconductor
$N_a^-(N_d^+)$	ionized acceptor (donor) dopant atom density (cm^{-3})
$N_a(N_d)$	acceptor (donor) dopant atom density (cm^{-3})
N_{dop}	net local dopant concentration (cm^{-3})
n_i	intrinsic carrier density (cm^{-3})
N_i	global shape function at node i
N_α	volumetric e-h pair profile within the ion track (cm^{-3})
N_ℓ	line e-h pair density along the ion track (cm^{-1})
NMOS	n-channel metal-oxide-semiconductor
p	hole carrier density (cm^{-3})
pdf	probability distribution function
p_n	equilibrium hole density within n-doped region (cm^{-3})
p-n	p-doped/n-doped (junction)
PS	particle simulation

PWM	partial waves method
q	electronic charge (C)
Q_c	critical charge for device upset (pC)
Q_i	charge assigned to node i (C)
Q_o	total initial charge of electrons (holes) within ion track (fC)
Q(t)	integrated charge collected from track over time (fC)
R	carrier recombination rate (cm^{-3} s^{-1})
r_t	initial ion track radius (μm)
RAM	random access memory
SE	secondary electron
SEC/DED	single-bit error correction/double-bit error detection
SEU	single event upset
SMDA	static-mobility diffusion approximation
SOS	silicon-on-sapphire
SRAM	static random access memory
t	time (s)
T	temperature (K)
v	carrier velocity (cm s^{-1})
V_a	applied voltage (V)
VHSIC	very high speed integrated circuit
VLSI	very large scale integration
W	width of depletion zone (μm)
X	parameter used in mobility calculations in equation (5.26)
α	inverse of the collection time constant of the p-n junction, equation (3.3) (s^{-1})

β	inverse of the generation time constant for the ion track, equation (3.3) (s^{-1})
Δt	computational time step (s)
ϵ	silicon permittivity (F cm^{-1})
ϵ_M	L^2-norm error measure
ℓ	semiconductor device feature size (μm)
$\mu_n(\mu_p)$	effective electron (hole) mobility (cm^2 V^{-1} s^{-1})
μ_L	lattice mobility (cm^2 V^{-1} s^{-1})
μ_I	impurity mobility (cm^2 V^{-1} s^{-1})
μ_{ccs}	carrier-carrier scattering mobility (cm^2 V^{-1} s^{-1})
$\rho(r,z)$	net charge density at coordinates (r,z) (C cm^{-3})
τ_α	ion track generation time constant (ps)
$\tau_n(\tau_p)$	electron (hole) lifetime (s)
ϕ	electrostatic potential (V)
Φ_i	potential at node i (V)
Φ_o	built-in potential at a p-n junction (V)
χ	dimensionless distance used in equation (6.6)
1-D	one-dimensional
2-D	two-dimensional
3-D	three-dimensional

ACKNOWLEDGEMENTS

I would like to thank all the members of my dissertation committee for their help and support: Professor Mohamed Abdou, Professor Tony Chan, Professor John Dawson, Professor Nancy Haegel, and Professor Nasr Ghoniem. Special thanks are given to my committee chairman, Professor Nasr Ghoniem, for his continuing advice, guidance, and support during my stay at U.C.L.A.

I would like to gratefully acknowledge the interest and advice of Dr. Yeong Song of TRW Corporation, who generously donated his time and acted as a partner in this effort along with Professor Ghoniem.

The continuing advice of my fellow researchers and partners in crime provided much support during my efforts: Philip Chou, Chuck Stone, Martin Vicanek, and Joan George. Together we fought off many a dreaded squealer.

My appreciation for the love and support of my wife Madhavi during this effort cannot be expressed in words. Our partnership gave meaning to Ph.D. research beyond mere academics.

Finally, I would like to express my appreciation to the University of California, Los Angeles for enticing me to continue Ph.D. research with a Chancellor's Fellowship, and to the State of California and TRW Corporation for providing my support during the remaining years as part of the MICRO Project.

VITA

Rodger Carl Martin

July 17, 1953	Born, Hershey, Pennsylvania
1981	B.S. in Chemistry, Magna Cum Laude Lebanon Valley College Annville, Pennsylvania
1981	Student Honor Award American Institute of Chemists
1985	Tau Beta Pi Engineering Honor Society University of Illinois at Urbana
1985	Alpha Nu Sigma Honor Society American Nuclear Society
1985-1986	Chancellor's Fellowship University of California, Los Angeles
1986	M.S., Nuclear Engineering University of Illinois at Urbana Urbana, Illinois

PUBLICATIONS AND PRESENTATIONS

P. I. H. Cooke, P. Gierszewski, M. Z. Hasan, R. C. Martin, S. Sharafat, D.-K. Sze, and C. P.-C. Wong, "Properties of Concentrated Aqueous Lithium Nitrate Solutions and Applications to Fusion Reactor Design," presented at the International Symposium on Fusion Nuclear Technology, Tokyo, Japan, April 10-19, 1988.

P. J. Gierszewski, R. C. Martin, K. Kalyanam, J. Bartlit, and D.-K. Sze, "Aqueous Salt Blanket Tritium Systems for the TITAN-II Reversed-Field Pinch Fusion Reactor Design," Fusion Technology, 14 (1988) 671-676.

M. Z. Hasan and R. C. Martin, "Use of Dissociating Gases as Primary Coolants and Working Fluids in Power Cycles for Fusion Reactors," presented at the Tenth International Conference on Structural Mechanics in Reactor Technology, Anaheim, CA, August 14-18, 1989.

Ph. K. Hopke, R. C. Martin, and M. A. Evins, "The Interpretation of Multielemental INAA Data Using Pattern Recognition Methods," J. Radioanalytical and Nuclear Chemistry, 112 (1987) 215-222.

R. C. Martin and N. M. Ghoniem, "Modeling of Tritium Transport in a Fusion Reactor Pin-type Solid Breeder Blanket Using the DIFFUSE Code," J. Nuclear Materials, 141-143 (1986) 244-248.

R. C. Martin and N. M. Ghoniem, "Modeling of Tritium Transport in a Pin-Type Solid Breeder Blanket," University of California, Los Angeles report UCLA-ENG-8608/PPG-934, Feb. 1986.

R. C. Martin and N. M. Ghoniem, "Monte Carlo Simulation of Coupled Ion-Electron Transport in Semiconductors," Physica Status solidi(a), 104 (1987) 743-754.

R. C. Martin, N. M. Ghoniem, Y. Song, and J. S. Cable, "The Size Effect of Ion Charge Tracks on Single Event Multiple-Bit Upset," IEEE Trans. Nuclear Science, NS-34 (1987) 1305-1309.

R. C. Martin and N. M. Ghoniem, "Coupled Ion-Electron Transport in Semiconductors," University of California, Los Angeles report UCLA-ENG-87-8/PPG-1024, March 1987.

R. C. Martin, D.-K. Sze, J. R. Bartlit, and P. J. Gierszewski, "Tritium Systems for the TITAN Reversed-Field Pinch Fusion Reactor Design," Proc. 12th Symposium on Fusion Engineering, Monterey, CA, Oct. 12-16, 1987, pp. 739-742.

R. C. Martin, N. M. Ghoniem, and Y. Song, "Monte Carlo Simulation of Electron-Hole Pair Generation Profiles Along Heavy-Ion Tracks in

Semiconductors," presented at the 5th Annual Symposium on Single Event Effects, Los Angeles, CA, April 7-8, 1987.

R. C. Martin and N. M. Ghoniem, "Higher Order Axisymmetric Finite Element Solution of Poisson's Equation for Semiconductor Device Simulation," University of California, Los Angeles report UCLA-ENG-8835/PPG-1195, Nov. 1988.

R. Najmabadi et al., "The TITAN Reversed-Field Pinch Fusion Reactor Study; The Final Report," University of California, Los Angeles report UCLA-PPG-1200, 1990, to be published.

T. J. Riley, Ph. K. Hopke, R. C. Martin, and J. J. Porter, "Provenance of Selected Middle Mississippian Vessel Forms from the Central Mississippi Valley, U.S.A. Using Hierarchical and Nonhierarchical Clustering of INAA Results," in Instrumental Techniques in Archaeological Research, S. U. Wisseman et al., eds., U.S. Army Construction Engineering Research Laboratory, Champaign, IL, 1988, pp. 87-113.

S. Sharafat, N. M. Ghoniem, E. Cheng, P. I. H. Cooke, S. Grotz, R. C. Martin, F. Najmabadi and C. P.-C. Wong, "Structure and Insulator Material Choices for the TITAN Reversed-Field-Pinch Reactor Study," Proc. 12th Symposium on Fusion Engineering, Monterey, CA, Oct. 12-16, 1987, pp. 1046-1053.

Y. Song, K. N. Vu, J. S. Cable, A. A. Witteles, W. A. Kolasinski, R. Koga, J. H. Elder, J. V. Osborn, R. C. Martin, and N. M. Ghoniem, "Experimental and Analytical Investigation of Single Event, Multiple Bit Upsets in Poly-silicon Load, 64K x 1 NMOS SRAMs," IEEE Trans. Nuclear Science, NS-35 (1988) 1673-1677.

Y. Song, K. N. Vu, J. S. Cable, A. A. Witteles, R. C. Martin, and N. M. Ghoniem, "Analysis of Single Event Effects Including Multiple Bit Upsets (MBUs)," presented at the 6th Annual Symposium of Single Event Effects, Los Angeles, CA, April 5-6, 1988.

C. P.-C. Wong et al., "Blanket Design for the ARIES-I Tokamak Reactor," presented at the Thirteenth Symposium on Fusion Engineering, Knoxville, TN, Oct. 2-6, 1989.

ABSTRACT OF THE DISSERTATION

Simulation of Charge Generation

and Transport in Semiconductors

Under Energetic Particle Bombardment

by

Rodger Carl Martin

Doctor of Philosophy in Engineering

University of California, Los Angeles, 1990

Professor Nasr M. Ghoniem, Chair

The passage of energetic ions through semiconductor devices generates excess charge which can produce logic upset, memory change, and device damage. This "single event upset" (SEU) phenomenon is increasingly important for satellite communications. Experimental and numerical simulation of SEUs is difficult because of the subnanosecond times and large charge densities within the ion track.

The objective of this work is twofold: (1) the determination of the track structure and electron-hole pair generation profiles following the passage of an energetic ion; (2) the development and application of a new numerical method for transient charge transport in semiconductor devices.

A secondary electron generation and transport model, based on the Monte Carlo method, is developed and coupled to an ion transport code to simulate ion track formation in silicon. The results provide more realistic charge density profiles than those used in previous SEU simulations. Charge profiles obtained for cosmic ion tracks are found to differ significantly from those of cyclotron ions used in cosmic-effect simulations.

A new numerical method is developed for the study of transient charge transport. The numerical method combines an axisymmetric quadratic finite-element formulation for the solution of the potential with particle simulation methods for electron and hole transport. Carrier transport, recombination, and thermal generation of both majority and minority carriers are included. To assess the method, transient one-dimensional solutions for silicon diodes are compared to a fully iterative finite-element method. Simulations of charge collection from ion tracks in three-dimensional axisymmetric devices are presented and compared to previous work.

The results of this work for transient current pulses following charged ion passage are in agreement with recent experimental data. Ion track densities larger than previously reported are simulated, which permits study of more realistic track profiles and evaluation of recombination effects. The numerical simulation results are used in developing simple analytical equations for circuit design to represent the current pulse and integrated charge collection from the ion track. The effects of processing and device variables on the SEU response can be addressed with the present method.

Chapter 1

INTRODUCTION

Interest in the effects of radiation on semiconductors has grown significantly for space and defense applications (e.g., satellite communications), integrated circuit (IC) processing using ion beams and ion implantation, packaging of semiconductor devices, and fission and fusion radiation effects on diagnostics and circuitry. Radioactive impurities (thorium and uranium) in silicon and IC packaging materials first raised concerns about radiation effects on semiconductors. The spontaneous decay of these nuclei generated errors in device performance, but this problem was mitigated by careful purification of the semiconductor material.

A new and more serious concern arose with observation of anomalies in spacecraft performance over the last decade, with the unexpected triggering of electronic components and the sudden generation of erroneous data. Radiation passing through the ICs causes these errors by generating transient charge which is collected at p-n junctions. Information is stored in binary form within circuits, so the energy deposited by radiation can generate enough spurious charge to alter the binary information state from 0 to 1 or vice versa, producing logic upset and memory change. This phenomenon is called a single event upset (SEU). SEUs take two forms: soft errors represent erroneous data which does not affect the device's continuing operation, and hard errors cause a circuit element to "latch-up" in a fixed logic state, inhibiting the device's continued

operation. Hard errors can destroy a device if significant current surges are generated.

The ability of a charged particle to generate SEUs is dependent on its linear energy transfer (LET) within the semiconductor material. LET is defined as the amount of energy deposited by a particle per unit distance travelled within the material. The transient charge generated is proportional to the particle's LET. Heavy ions such as iron have the largest LET and raise the greatest concern in space. The amount of charge required to generate an SEU is defined as the critical charge (Q_c), and is a function of the device geometry and the size of the depletion zone at a p-n junction. The depletion zone is the high-field region which rapidly removes excess charge within its domain, generating a current pulse at the contact. The "funneling" phenomenon increases SEU concerns by increasing the volume of the sensitive region for field-induced transient charge collection: the dense charge track pulls the electric field lines down into the bulk of the device, increasing the magnitude of the prompt collected charge.

Microelectronic components aboard spacecraft are exposed to significant radiation fields which vary with the spacecraft's location in space. The earth's magnetic field acts to shield the spacecraft in near-earth orbit from high-energy cosmic ions, so exposure to protons and electrons trapped within the Van Allen belt predominates. In very high altitude orbits and deep space, cosmic ray exposure is dominant. Cosmic protons have too low an LET to generate soft errors directly, but they can generate soft errors by

inducing nuclear reactions when captured by heavier nuclei within the semiconductor material. The cross sections for such nuclear reactions are small enough that heavy cosmic ions remain the greatest concern, although the substantial alpha particle flux in space can raise problems for SEU-sensitive devices.

Cosmic ions can have very high energies, with GeV energies common and energies well beyond the TeV range observable. Earth-based simulation of such energies is impossible, but cyclotrons can accelerate heavy ions such as argon and krypton up to 300 MeV, until the LET of these ions is comparable to the LET of cosmic ions. ICs are bombarded with these cyclotron ions, and the number and frequency of upsets is recorded to approximate the cross section for device upset. A critical evaluation of the differences between cyclotron and cosmic ion tracks has not been made, so the assumption of comparable electronic effects for comparable LET must be taken for granted. This assumption is valid in terms of the magnitude of energy deposition over a few microns, but the comparability of the axial and radial energy deposition profiles with respect to the ion path is less certain, and is evaluated in more detail in this study.

An important development which impacts the significance of ion-induced upsets is the profound reduction in semiconductor device geometries in recent years, as typified by today's Very Large Scale Integration (VLSI) circuitry and its extension to the Very High Speed Integrated Circuits (VHSIC) of tomorrow. Size reductions increase circuit speed, memory, and capabilities, and greatly enhance satellite performance, but with device feature sizes now comparable

to the width of heavy ion tracks, memory circuits and microprocessors have become more susceptible to ion-induced upset. Another driving force for microminiaturization is the defense establishment's needs for computerization of weapons systems. Modern warplanes are flying computers with information-processing capabilities limited only by the bulk of electronics feasible for inclusion in a lightweight aerospace system.

As microminiaturization advances, understanding of the scaling laws for SEU rates as a function of device size is needed. As devices become smaller, Q_c also becomes smaller. A tradeoff exists between the reduced area (i.e., reduced cross section for ion interaction) and the smaller Q_c. As devices are packed closer and closer, the ability of a single ion to upset multiple elements raises serious concerns for state-of-the-art ICs in space.

SEU problems can be mitigated by either applying error detection and correction (EDAC) software methodologies, by improving the design and resistance to radiation of the device element, or by a combination of the two. To develop radiation-resistant devices, we need to understand the fundamental processes involved in ion-induced charge collection. Development of experimental programs and simple analytical models are helpful, but the complexity and ultrafast time-dependence of the phenomena involved require detailed numerical simulations of specific devices for quantitative evaluations.

This study considers two aspects of the SEU problem: simulation of charge track formation along an ions's path in silicon, and simulation of the collection of this transient charge at the p-n

junction by developing a novel numerical technique. In Chapter 2 the space radiation environment and SEU phenomenon is described in more detail, as well as approaches used to overcome SEU problems. Chapter 3 discusses previous efforts in SEU modeling and experimentation, and discusses modeling of both the ion charge track profiles and charge collection from ion tracks. The initial charge track size and density profile are important for SEU numerical simulations, but most previous efforts assume simplified initial charge track profiles of uniform densities over a fixed radius, without the peak densities expected for heavy ion tracks. Effects of more detailed and realistic track structures on subsequent charge collection has not been analyzed. To avoid these simplified assumptions we have implemented a more realistic Monte Carlo-based analysis of secondary electron generation and transport and track formation within an ion transport code. The methodology and results will be discussed in Chapter 4.

Chapter 5 discusses our approach to the numerical simulation of transient device behavior, based on a hybrid finite element/particle simulation method. The particle simulation (PS) techniques are similar to those used in plasma simulations. To solve Poisson's equation we use an axisymmetric finite element (FE) formulation with quadratic interpolation of potential.

Chapter 6 assesses the accuracy, strengths, and limitations of our method compared to analytical device equations and more traditional FE device simulation codes. Chapter 7 shows results of our simulations of SEU effects and comparisons with previous SEU

simulations, presents our capabilities for simulating high-density ion tracks and more realistic track structures than have previously been attempted, and discusses the strengths of our method for detailed charge collection and current pulse evaluations. We present the conclusions we have drawn from our study in Chapter 8.

In summary, this work attempts to provide an accurate description of the physics involved in SEU phenomena by developing a numerical method that holds potential for simulation of fast transients and non-equilibrium carrier transport in devices as well as future studies of other radiation-induced phenomena.

Chapter 2

SPACE RADIATION EFFECTS ON MICROELECTRONIC SYSTEMS

2.1 The Space Radiation Environment

Semiconductor devices are potentially exposed to a variety of radiation sources, e.g., the cosmic environment, nuclear reactors, nuclear explosions, and IC processing. This study emphasizes the cosmic environment and damage by heavy ions. An introduction to radiation effects on semiconductor devices can be obtained from a number of sources, e.g., [2.1-2.5].

The radiation environment in space consists of three components: (1) photons such as x-rays and γ-rays, (2) charged particles such as electrons, protons, alpha particles (i.e., helium nuclei), and heavy ions, and (3) neutrons. Displacement damage and ionization effects constitute the primary radiation effects on semiconductors in space. Displacement damage is caused by neutron and heavy ion collisions, which generate induced defect states, increase the number of scattering centers, generate more energy levels in the band gap, and degrade carrier lifetimes and transistor gain. Ionization effects consist of total dose effects or transient ionization effects: the gradual buildup of excess charge generates total dose effects such as voltage offsets, leakage currents, and mobility degradation in transistors, while photocurrents and charged-particle-induced currents are examples of transient ionization effects.

We are concerned with the transient effects induced by rapid ionization within the bulk of the semiconductor and the resulting electron-hole (e-h) pair generation, such as occurs with ion passage. Charged particles slow down in matter either by nuclear collisions or by ionization of the material. Nuclear collisions are less significant for the slowing down of high-energy ions. Silicon requires 3.6 eV to form one e-h pair during ion slowing down, more than three times the energy required for equilibrium e-h pair generation. Individual ions generate single event upsets (SEUs) when the excess charge deposited in the device reverses the logic state of the p-n junction and gives erroneous data or induces current latchup.

In typical metal-oxide-semiconductor (MOS) devices, LETs of a few MeV/μm are required to cause an upset [2.6], i.e., particles with atomic number $\geq$ 2 and energies in the MeV range or above. The natural environment only generates a significant flux of such particles in exoatmospheric cosmic rays. For satellites in near-earth orbit, the largest flux of relativistic ions is that of protons, which only raises SEU concerns if nuclear collisions generate displacements or nuclear transformations. The alpha particle flux is about an order of magnitude less than the proton flux, and the flux of all heavier ions is another order of magnitude less. The relative fluxes decrease rapidly for ions heavier than iron. The cosmic ion spectrum is isotropic, with energies typically in the MeV range and above, with a very small flux of particles with TeV energies and above. Figure 2.1 shows the relative cosmic differential fluxes for 5 ions as a function of energy [2.7]. Solar

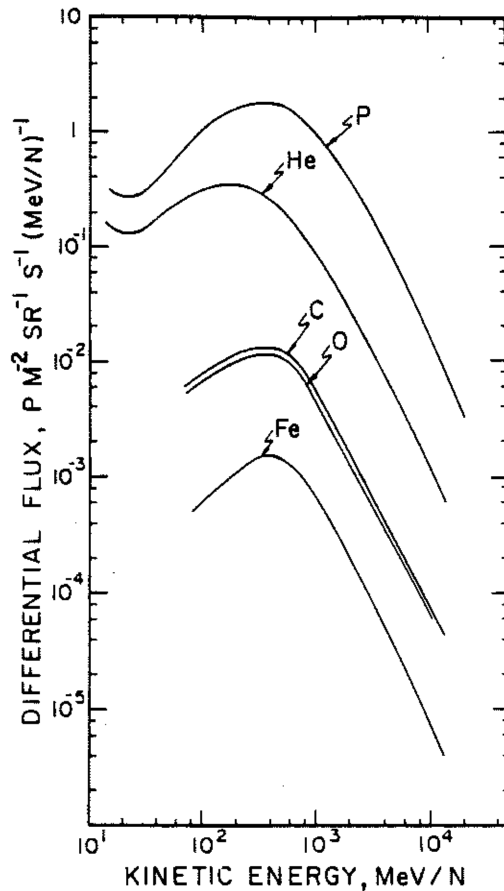

Figure 2.1: Differential cosmic ray flux for protons, helium, carbon, oxygen, and iron nuclei for solar minimum [2.7].

flare activity increases SEU dangers by significantly increasing the heavy ion flux [2.8].

The orientation of a satellite or high-flying aircraft relative to the earth's magnetic field has a major impact on radiation exposure. The earth's magnetic field deflects charged particles such as cosmic rays, and objects in low earth orbit tend to be protected from the cosmic flux. This protection is greatest at the equator, lowest at the poles, and decreases with altitude. In near-earth orbit the spacecraft is primarily exposed to protons and electrons

trapped within the Van Allen belt. In deeper space (10,000 km or more), the earth has no effect and the predominant exposure is due to cosmic rays.

Cosmic rays originate from two sources, the continuous solar wind with ion energies predominantly below 1 MeV, and solar flares which emit higher-energy ions. Extraterrestrial cosmic rays interact with the atmosphere and generate secondary cosmic particles which reach the earth; although the flux is much reduced at the earth's surface, interactions with semiconductor components are observable, e.g., in supercomputer memories.

The structure of the surrounding spacecraft does not alleviate SEU concerns by reducing the cosmic flux. Nuclear and charged-particle interactions with the surrounding material can actually increase the total radiation flux by creating additional secondary particles. Lower-energy particles often have a larger cross section for interaction, depositing more energy and causing more damage than their higher-energy precursors. Shielding is also not a practical solution for SEU problems [2.9]. Only thick shielding is effective against large ion energies, but weight limitations and present-day costs of about $8000 per kilogram to put hardware into orbit make such shielding impractical.

2.2 The Single Event Upset Phenomenon

Cosmic-ion-induced random bit errors in satellite memories were first postulated in 1962 [2.10]. Evidence of this phenomenon was

presented in 1975 in the form of an anomalous triggering of a bipolar flip-flop in a communications satellite [2.11]. In 1978 cosmic-ray-induced anomalies observed in n-channel metal-oxide semiconductor (NMOS) dynamic random access memories (RAMs) in a satellite system were evaluated [2.9]. Between 1970 and 1982 over 40 upsets have been reported in satellite operations [2.12]. By 1979 soft errors due to alpha particles emitted by natural radioactive decay of silicon and packaging impurities had been reported, along with phenomenological modeling of these errors [2.13,2.14]. The potential for cosmic-ray-induced upsets is now a very real concern for satellite operations; e.g. the Tracking Data Relay Satellite Systems (TDRSS) satellite experiences upsets every 1.5 days and the Galileo project required a crash program to harden its circuitry against cosmic effects [2.12]. About 1% of the TDRSS upsets were reported to involve more than one bit [2.15].

An energetic ion can traverse a typical semiconductor device active region in a fraction of a picosecond. The most important factor in a charged particle's ability to generate SEUs is its linear energy transfer (LET) in the semiconductor material, i.e., the amount of energy deposited per unit distance travelled, with the transient charge generated proportional to the LET. The resultant transient current consists of two components: a prompt component from e-h pairs formed within the depletion zone of the p-n junction, and a delayed component due to carriers generated within a diffusion length of the junction. The magnitude of the prompt component can be enhanced by field "funneling," i.e. the dense e-h plasma along the ion track

forces the junction field lines down into the device substrate. Funneling effectively increases the volume of the sensitive region for field-induced transient charge collection and increases the transient current pulse, as well as altering device operating characteristics. For soft errors, device operation can return to normal after the excess charge is collected at the contacts or recombines. Memory devices are particularly susceptible to transient charge effects, as their operation is based on the storage of charge at each bit, and collection and storage of spurious charge takes the form of erroneous data. SEUs do not permanently damage the device unless current latchup damages or burns out the circuit before it can be turned off. SEUs are more difficult to detect and correct in microprocessors than in memory circuits.

The amount of charge required to generate an SEU is defined as the critical charge (Q_c), and is a function of the device geometry and the size of the depletion zone at a p-n junction. The depletion zone defines the high-field region within the device which rapidly removes excess charge within its domain, generating a burst of current at the contact. As devices become smaller and the sensitive regions become smaller, the magnitude of Q_c required for upset becomes smaller. For present device geometries on the order of a few microns, Q_c is typically on the order of a picocoulomb or less. A heavy ion can easily generate a picocoulomb or more of transient charge in passing through several microns of silicon. Figure 2.2 shows an estimate of the upset rate as a function of critical charge for different components of the cosmic spectrum [2.8]; only heavier

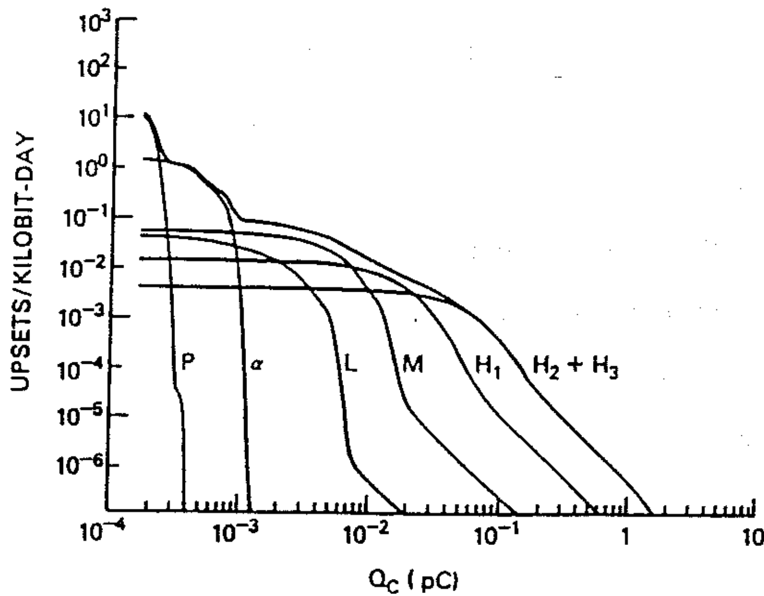

Figure 2.2: Estimate of the daily upset rate per kilobit as a function of critical charge, for several groups of cosmic ray elements. Labels P, α, L, M, H_1, and H_2+H_3 refer to the atomic number groups of 1, 2, 3-5, 6-9, 10-15, and 16-26, respectively [2.8]. Altitude of 75,000 feet is assumed.

ions can upset those junctions more resistant to upset. IC feature sizes range from 3 to 10 μm for standard VLSI devices, and the new VHSIC devices aim for micron and submicron feature sizes. The larger 10 μm bulk circuits are only upset by heavy cosmic ions, while the 3 μm circuits can be upset by lighter ions [2.16].

2.3 Technological Features and Radiation Hardening

The sensitivity of an electronic device to SEUs is given by its cross section and threshold for upset. The cross section represents the fraction of upsets generated by a flux of ions over time, although parameters such as the angle of the beam with respect to the

device and the LET of the ions must also be considered. The threshold for upset is the lower limit for ion LET at which the number of upsets becomes significant. These SEU parameters are measured by placing a device within a cyclotron or other source of ions and measuring the number and rate of upsets as a function of energy and type of ion. Memory circuits are relatively easy to test, with the data periodically checked for accuracy. Microprocessors and other complex devices require specialized software for checking errors, as a soft error in different components may manifest itself in a variety of ways and may not be immediately apparent in device operation.

Two generic approaches are used to mitigate SEU problems. The first is a fault-tolerant logic design and the second is hardware-related such as device or circuit design. Fault-tolerant logic design such as the use of error detection and correction (EDAC) techniques increases the nonproductive circuit overhead, so the overall system performance is degraded as upset rates increase unless hardware-related corrective measures are also employed.

The use of EDAC techniques mitigates problems arising from an SEU in a single memory bit [2.17]. Within a 16-bit word, 6 extra bits are required for single-bit EDAC [2.18]. Continuing device microminiaturization reduces junction separations and increases the probability of multiple-bit upset (MBU) by single ions. Double-bit upset rates in satellite memory cells as high as several percent of total upsets have been reported [2.20]. High MBU rates pose a major problem for SEU mitigation. A double-bit error in one word requires

several additional bits for EDAC. A simpler solution is the use of redundant memory cells. Neither solution is practical, so the present solution is limited to single-bit error correction/double-bit error detection (SEC/DED). Double-bit errors can be mitigated by spatially dispersing those memory cells representing a single word, but layout efficiencies and high-speed operation are penalized. With satellites costing $100 million or more, MBU mitigation incurs heavy penalties.

Several approaches have been suggested for physically hardening devices and circuits [2.16], such as reducing minority carrier lifetimes, adding a barrier insulating layer below the junction to reduce funneling, increasing the doping density to reduce the impact of SEUs, and inserting protective circuitry within the feedback paths of memory and logic cells.

All microelectronic circuitry is sensitive to radiation-induced errors to some degree. CMOS (complementary metal-oxide semiconductor) devices which employ silicon-on-sapphire (SOS) technologies reduce the significance of charge funneling and sensitivity to upset by isolating the depletion regions from the bulk of the device by use of an aluminum oxide substrate. However, for very small devices these buried layer designs are not simple to fabricate. The CMOS/SOS technologies tend to be less sensitive to upset than bulk CMOS devices, which exhibit the greatest potential for latchup [2.12].

With transient charge collection often faster than a nanosecond, carrier lifetime reduction in silicon is typically limited to longer

time frames and thus cannot be a successful hardening technique by itself. Increasing doping density can significantly improve resistance to upset by reducing carrier lifetimes and by reducing the relative magnitude of transient charge densities and the resulting funnel effect, but other electrical parameters are affected such as increased electric field across the smaller depletion zone. Soft errors can be mitigated by circuit engineering, e.g., increasing a cell's critical charge using resistive decoupling. CMOS memory cells can be hardened by insertion of a delay mechanism such as a resistor within the feedback path; with the element speed reduced below the nanosecond time frame for SEUs, the memory cell cannot flip states until the SEU pulse is dissipated. Such hardening penalizes the performance of circuits with subnanosecond device speeds.

As microminiaturization advances, understanding of the scaling laws for SEU rates as a function of device dimensions is needed. Although the reduced device area reduces the cross section for interaction with radiation, the device Q_c for upset is also reduced. Figure 2.3 shows Q_c as a function of feature size for different device technologies [2.12]. Major problems will result if Q_c ever becomes small enough that the abundant cosmic protons can cause upsets. The closer proximity of device components will increasingly make neighboring components susceptible to upset by single ions, and some sensitive memory components have demonstrated remarkably large cross sections under cyclotron test conditions because of MBUs [2.20]. These concerns need to be evaluated in detail as state-of-the-art ICs are placed into space now and in the future.

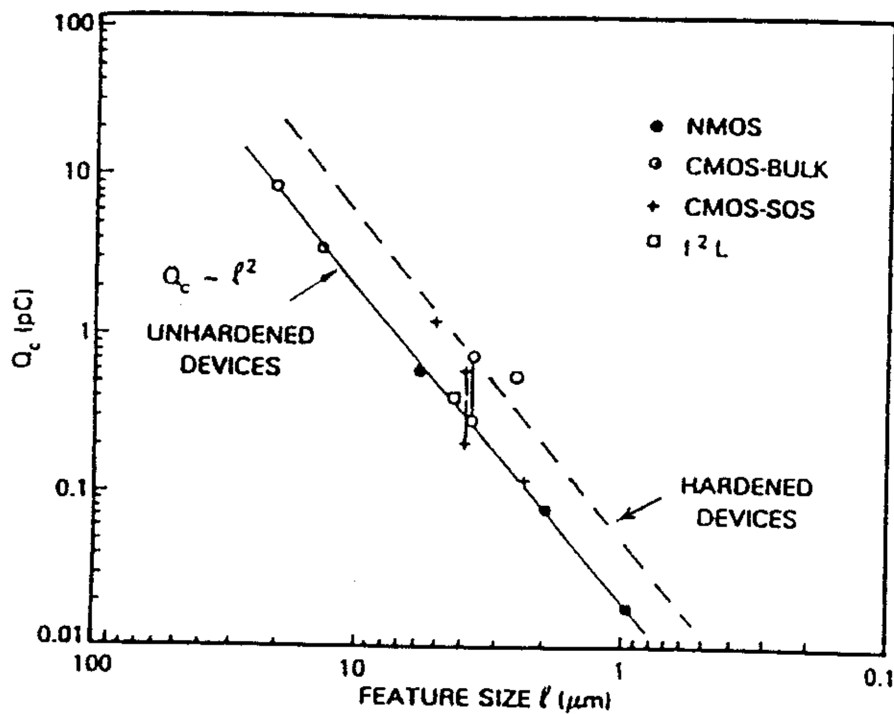

Figure 2.3: Critical charge for single event upset as a function of device feature size for several device technologies [2.12]. I^2L refers to integrated injection logic device.

2.4 References

[2.1] G. C. Messenger and M. S. Ash, The Effects of Radiation on Electronic Systems, Van Nostrand Reinhold, N.Y. 1986.

[2.2] J. R. Srour, D. M. Long, D. G. Millward, R. L. Fitzwilson, and W. L. Chadsey, Radiation Effects on and Dose Enhancement of Electronic Materials, Noyes Publications, Park Ridge, N.J. 1984.

[2.3] V. A. J. van Lint, T. M. Flanagan, R. E. Leadon, J. A. Naber,

and V. C. Rogers, Mechanisms of Radiation Effects in Electronic Materials, Vol. 1, Wiley-Interscience, N.Y. 1980.

[2.4] R. J. Chaffin, Microwave Semiconductor Devices: Fundamentals and Radiation Effects, Wiley-Interscience, N.Y. 1973.

[2.5] F. Larin, Radiation Effects in Semiconductor Devices, John Wiley, N.Y. 1968.

[2.6] J. C. Pickel and J. T. Blandford, Jr. IEEE Trans. Nucl. Sci., NS-27 (1980) 1006.

[2.7] M. A. Shea, "Assessment of the Energetic Particle Environment," presented at 4th Ann. Symp. on Single Event Effects (Los Angeles, CA, April 1986).

[2.8] R. Silberberg, C. H. Tsao, and J. H. Adams, Jr., IEEE Trans. Nucl. Sci., NS-30 (1983) 4405.

[2.9] J. C. Pickel and J. T. Blandford, Jr., IEEE Trans. Nucl. Sci., NS-25 (1978) 1166.

[2.10] J. T. Wallmark and S. M. Marcus, Proc. IRE, 50 (1962) 286.

[2.11] D. Binder, E. C. Smith, and A. B. Holman, IEEE Trans. Nucl. Sci., NS-22 (1975) 2675.

[2.12] L. Adams, Microelectronics J., 16 (1985) 17.

[2.13] T. C. May and M. H. Woods, IEEE Trans. Electron Devices, ED-26 (1979) 2.

[2.14] D. S. Yaney, J. T. Nelson, and L. L. Vanskike, IEEE Trans. Electron Devices, ED-26 (1979) 10.

[2.15] R. J. Moore, "TDRSS RAM Hit Fix is on the Way," presented at 5th Ann. Symp. on Single Event Effects (Los Angeles, CA, April 1987).

[2.16] G. C. Messenger, "Techniques for Minimizing Soft Error Upset Rate for Large Scale Integrated Circuits," Doctoral Thesis (February 1987).

[2.17] J. P. Retzler, IEEE Trans. Nucl. Sci., NS-28 (1981) 3998.

[2.18] R. C. Martin, N. M. Ghoniem, Y. Song, and J. S. Cable, IEEE Trans. Nucl. Sci., NS-34 (1987) 1305.

[2.19] J. B. Blake and R. Mandel, IEEE Trans. Nucl. Sci., NS-33 (1986) 1616.

[2.20] Y. Song et al., IEEE Trans. Nucl. Sci., NS-35 (1988) 1673.

Chapter 3

REVIEW OF THEORETICAL AND EXPERIMENTAL STUDIES OF SINGLE EVENT UPSETS

3.1 Modeling of the Charge Track

The initial width and density profile of the ion track is an important initial condition for SEU calculations. Initial assumptions of ion track parameters will impact the final simulation results. An early discussion (1978) by Bradford [3.1] of the impact of ion tracks on VLSI radiation testing discussed phenomenologically the track profiles. With maximum secondary electron energies about 10 keV having a range of 1.4 μm in silicon, Bradford postulated non-trivial energy deposition as far as 1 μm from the ion path in silicon. He reported on previous results indicating a r^{-2} dependence on energy deposition as a function of radius, r, from the ion's path, and concluded an ion track would consist of a central core about 20 Å in radius with very large charge densities, and the densities decreasing as r^{-2} out to about 1 μm.

An analytical evaluation of transient charge collection by Messenger in 1982 [3.2] assumed a Gaussian-shaped track profile with an initial peak density exceeding 10^{18} cm^{-3} and decreasing radially with a dependence of $\exp(-r^2)$, an initial track radius of less than 0.1 μm, and a track formation time on the order of picoseconds. Subsequent efforts in modeling transient SEU charge collection from alpha-like tracks usually assumed an initial cylindrical track of 0.1 μm radius and constant excess carrier density [3.3,3.4].

Grubin, Kreskovsky, and Weinberg [3.5] did 2-D parametric studies of charge collection for track densities, N_α, of 10^{17} to 10^{19} cm^{-3}. They assumed a charge track of 0.1 μm radius and a track generation rate G_α given by:

$$G_\alpha = \frac{N_\alpha}{\tau_\alpha} \exp(-t/\tau_\alpha) \quad , \tag{3.1}$$

with the time constant τ_α assumed to be 3 ps. This expression generates 95% of the track carriers in 9 ps. Other discussions of alpha track formation suggest the track e-h plasma thermalizes on the order of picoseconds in a cylindrical track with radius about 0.1 μm and density of 10^{18} to 10^{19} cm^{-3} [3.6].

More recent SEU simulations by Zoutendyk et al. [3.7] mention core densities within the ion track in excess of 10^{18} cm^{-3} and apparently use a track of 0.5 μm radius for 40 MeV bromine, but no radial density profiles are mentioned so uniform track densities on the order of 10^{18} cm^{-3} are probably used. For heavy ions with large LET, initial e-h pair densities within the track should be in the range of 10^{20} cm^{-3} [3.8].

Evidence for larger track sizes is given by cosmic ray passage through photographic emulsions, resulting in track diameters on the order of microns [3.9]. Although the physics of track formation in emulsions is different from that in semiconductors, such evidence raises questions about the track diameters usually postulated for SEU simulations.

2-D simulations must assume that all physical quantities are constant in the unmodeled dimension (i.e., the device width), so the

charge track must be approximated as a 2-D slab. The resulting noncylindrical track shape requires normalization of the track density to maintain the same total transient charge in 2-D vs. 3-D simulations, impacting the rate of carrier recombination and the rate of radial spreading of the track with time.

3.2 Charge Transport Modeling

3.2.1 Analytical Models

By 1978 phenomenological models for cosmic-ray-induced errors in MOS memory cells had been postulated [3.10], which considered each node's critical charge for upset and a sensitive volume for charge collection from both the depletion region and a region within one diffusion length of the junction. The error rate was based on the relationship between an ion's LET, the critical charge, the sensitive volume, and the ion's average path length through the sensitive volume.

After the concern of the funnel effect was raised in 1981, Hu emphasized an axial charge separation mechanism along the track to phenomenologically evaluate the funneling depth as extending beyond the depletion zone by a factor of $(1 + \mu_n/\mu_p)$ [3.3]. Although his results were comparable to a previous numerical simulation, they showed maximum current at time equals zero and thus did not provide details of the initial current pulse.

The next phenomenological model was developed by McLean and Oldham [3.6]; by emphasizing a radial charge separation mechanism, they approximated the total collected charge as a function of applied voltage, initial plasma line density N_ℓ (e-h pairs per cm track length), carrier mobility, and approximate effective funnel length and charge collection time. They concluded that collected charge has a dependency on N_ℓ to the 4/3 power. Their calculated results agreed qualitatively with experimental results but quantitative agreement was not always good. This model was extended to better handle high density tracks by including an additional term with a stronger dependency on ambipolar diffusion; this adjustment gave better agreement with experiment for ions heavier than helium, but had trouble accurately evaluating charge collection for ions heavier than oxygen [3.8].

Extensions of these models have been attempted, e.g. by Gilbert who introduced an additional plasma screening consideration [3.11], and Oldham et al. who introduced a term for the average field along the track [3.12], but these phenomenological models are limited by their approximations in quantitative evaluations of charge collection, and are weak in providing information on the time-dependence of the current pulse.

In 1982 Messenger presented a detailed analytical evaluation of temporal and spatial track evolution [3.2]; he assumed an initial Gaussian track profile as hypothesized by Jaffe [3.13]:

$$N_\alpha = (N_\ell/\pi r_t^2) \exp(-r^2/r_t^2) \quad , \qquad (3.2)$$

with N_α the volumetric e-h pair profile along the ion path, r_t the assumed track radius at t = 0, and N_ℓ the line density typically 10^7 to 10^{11} e-h pairs/cm. He notes the initial N_α will exceed 10^{18} cm^{-3}, but assumes an initial track radius of less than 0.1 μm. By comparing drift and diffusive components, Messenger concluded that field motion typically starts after the ion track has expanded from an initial radius of 0.1 μm to about 1 μm after 500 ps, with field effects not dominant until ambipolar diffusion reduces N_α to values comparable to the doping concentration, N_{dop}.

Messenger also postulated an analytical solution for the time-dependence of the transient current pulse (I_t) amplitude in the form:

$$I_t(t) = I_o \, [\exp(-\alpha t) - \exp(-\beta t)] \quad , \tag{3.3}$$

in which he defines I_o to approximate the maximum current, α^{-1} to represent the collection time constant of the junction, and β^{-1} to represent the time constant for generation of the ion track. He derived the junction time constant to be:

$$\alpha^{-1} = \epsilon / q \bar{\mu} N_{dop} \quad , \tag{3.4}$$

with ϵ the material permittivity, q the electronic charge, $\bar{\mu}$ an average high-field-adjusted carrier mobility, and N_{dop} the doping concentration of the silicon substrate. The value for β is assumed to be $>10^{11}$ s^{-1}.

Phenomenological models are still frequently used and updated (see e.g., [3.14]), but for detailed calculations computer simulation

has been increasingly employed in recent years to avoid the approximations which limit these models.

3.2.2 Computational Models

SEU effects on a 2-D diode structure were first computationally evaluated by Hsieh, Murley, and O'Brien in 1981 [3.15]. They reported from both experiment and finite element modeling that the field-funneling effect can occur with alpha-particle hits on a junction, collapsing the junction field into the device substrate, increasing the prompt component of the transient current, and increasing concerns about single ion hits on junctions. The field was restored to equilibrium after about 1 ns in their simulations.

More detailed charge collection calculations from alpha particles were again performed by Hsieh et al. in 1983, again using FE methods [3.4]. They compared 2-D and axisymmetric 3-D results for a junction hit, and concluded the duration of funneling is shorter and less charge is collected in 3-D because of increased outward diffusion relative to 2-D simulations. Their transient currents peaked at about 300 μA after a few tens of picoseconds. They also simulated the near miss of the junction by an ion and saw delayed and reduced funneling. These simulations used a track radius of 0.1 μm.

In 1986 and 1987 Kreskovsky and Grubin addressed the relative accuracy of 2-D and 3-D simulations in silicon [3.16]; they normalized N_α to simulate a 2-D slab. 3-D field restoration to equilibrium was much faster than in 2-D, and 3-D charge collection

was about four times faster although total collected charge was comparable. The 2-D current pulse was maximum at time equals zero, while the maximum 3-D pulse occurred at about 20 ps. For similar simulations in GaAs they found poorer quantitative agreement, which they explained on non-linear transport behavior [3.17]. They reported their 3-D analysis required 3.4 CPU hours on a CRAY-1 computer for 17,500 grid points over 350 time steps, using linearized block implicit methods applied to a finite difference formulation [3.18].

J. A. Zoutendyk et al. have more recently been using an axisymmetric version of the PISCES II device simulation code for SEU simulations of ion hits on IC memory circuits such as static and dynamic random access memories (SRAMs and DRAMs), to assist in the interpretation of cyclotron SEU cross section results [3.7,3.19]. They are simulating the effects of heavy ions such as 40 MeV bromine and 100 MeV oxygen, and have obtained current pulse curves and looked at the effects of lateral charge transport on multiple-bit errors in memory circuits. Although their initial ion tracks are wider than those used in previous simulations, up to 0.5 μm in radius but of apparently uniform densities, their results are device specific. They have apparently not pursued analyses with more detailed ion track profiles or pursued an in-depth comparative study of the effects of various heavy ions of different initial energies and track density profiles.

3.3 Limitations of Previous Models

Although they serve as a good starting point, phenomenological models are not very accurate for initial current transients. Too many variables are inherent in the SEU process and the field distortion for such models to be quantitatively accurate, and the time dependence of the SEU current pulse becomes very difficult to postulate. These models have not taken carrier recombination into account at high densities, and their agreement with experiment becomes poorer with heavier ions.

Use of simplified track profiles for SEU simulations can only provide parametric results. Assumptions about the initial track may underestimate its actual size because they do not take into account the effect of energetic secondary electrons, as mentioned by Bradford [3.1]. Quantification of the transient current pulse depends on the assumptions used for initial ion track profiles. Peak charge density, effective track width, and spatial density profile may significantly affect the final results. As an example, N_α on the order of 10^{20} cm^{-3} can be expected [3.8]. In such a plasma-like state, carrier mobilities are reduced to their ambipolar values, and Auger recombination becomes very significant in reducing peak carrier densities. Use of tracks with 10^{18} cm^{-3} density may miss such details. Only Zoutendyk et al. simulated high-LET, heavy-ion tracks, but their track densities remained well under 10^{19} cm^{-3} [3.7]. Only Grubin et al. [3.5] report one simulation with track densities of 10^{19} cm^{-3}, but their detailed calculations use densities of 10^{18} cm^{-3}

to simplify the simulation. The high rate of MBUs observed in space raises questions as to the size and profile of the charge tracks used in these simulations.

A limitation of the 2-D simulations is the inherent assumption that all physical quantities are constant in the third dimension, so the charge track is approximated as a 2-D slab. The resulting noncylindrical track shape alters the charge track density and reduces the magnitude of the high-density Auger recombination in 2-D vs. 3-D modeling. For example, Fu et al. increased the Auger coefficients by a factor of 100 for more realistic recombination rates in 2-D modeling [3.20].

Even with N_α normalized to approximate 3-D effects, a significant difference between 2-D and 3-D results is apparent [3.16], with poor representation of the initial current pulse (maximum at time equal zero) and a time frame several times longer for 2-D charge collection. These differences are explained by the greater lateral spreading of the track in axisymmetric geometry compared with the 2-D spreading confined to planar geometry, plus the geometrical effects of the different relative sizes of the contacts in the 2-D and 3-D simulations with respect to the ion track cross section.

Messenger's analytical model of field motion after 500 ps is too long a time frame compared with experiment, and simulations frequently indicate peak currents occur at tens of picoseconds, shorter than experiment indicates. No numerical simulations have yet accurately reproduced the experiments discussed below.

3.4 Experimental Efforts

Experimental SEU simulations fall under two categories: the conventional cyclotron simulations to determine device cross section and threshold for SEU, and detailed studies of the time-dependence of the charge collection process after an ion hit. Much effort has gone into cyclotron simulations to evaluate susceptibility to upset for a variety of devices [3.21]. Generation of relativistic cosmic-like ions such as iron is only feasible in the Lawrence Berkeley Laboratory Bevalac, which can generate ions with energies approaching 1 GeV/nucleon. Although a few simulations have been performed with the Bevalac [3.22], they are expensive so damage simulation is typically obtained using cyclotrons which can generate ions with energies up to a few MeV/nucleon, to a maximum of about 300 MeV. For iron, such energies will not provide the LET of interest for cosmic SEU effects, so ions such as argon and krypton are accelerated until their LET characteristics are similar to cosmic iron. The 88 inch cyclotron at the University of California at Berkeley is often used for such simulations, although its use is also not inexpensive. Inexpensive heavy-ion simulations can be performed with fission decay products of californium-252, but a spectrum of ions is obtained which gives less specific SEU information. Van de Graaff machines and smaller cyclotrons can be employed for light ion and proton SEU simulations.

One weakness of cyclotron simulations using non-cosmic ions is the assumption that comparable electronic effects for ions with

comparable LETs should be expected. This assumption is valid in terms of the magnitude of energy deposition within the first few microns of device penetration, but the comparability of the axial and radial energy deposition profiles is less certain. Any differences between these tracks may make accurate quantitative evaluations difficult and impact the reliability of such testing. A critical evaluation of the differences has not been made.

Detailed experimental studies of SEU current transients after an ion hit have been underway at Los Alamos National Laboratory. Early SEU simulations over a nanosecond time scale provided information on total collected charge as a function of applied device voltage, but Wagner et al. have done experiments with an ultrafast 70 GHz sampling oscilloscope which uses superconducting Josephson junction technology and a superconducting delay line, reducing the rise time to 6 ps [3.23]. Wagner et al. have observed the transient current pulses in silicon and GaAs diodes for ions ranging from 5 MeV alpha to 100 MeV iron. The measured times to peak current typically range from 100 to 200 ps, longer than that postulated by most numerical simulations with suggest peaks occurring after a few tens of picoseconds. Wagner et al. have attempted to adapt Messenger's model [3.2] to their transient data with some success, but simplifying assumptions are required and the leading edge of the pulse cannot be simulated [3.23]. Other computational attempts at reproducing these experimental results have not been reported.

3.5 Effects of External Circuit

After a device is struck by an ion, a transient current pulse is generated which can also affect other devices within the circuit, altering their operating voltages and characteristics. To simulate these circuit effects a general circuit simulation code such as SPICE or PISCES must be employed. For the initial SEU effect, either an assumed current pulse is input into one component of the circuit, or the output from an actual SEU device simulator is used as input into, e.g., the SPICE code.

The circuit effects of SEUs is beyond the scope of this study. As examples of circuit modeling of SEU effects, Song et al. used results from our study of several ion track profiles as input into the PISCES code, to simulate MBU effects on NMOS SRAMs as a function of ion LET [3.24]. Zoutendyk, Secrest, and Berndt used an axisymmetric version of PISCES to simulate transistor response to an oxygen ion hit, for subsequent coupling to the SPICE circuit simulator to evaluate SEU effects on a silicon bipolar test device [3.19].

3.6 References

[3.1] J. N. Bradford, IEEE Trans. Nucl. Sci., NS-25, (1978) 1144.

[3.2] G. C. Messenger, IEEE Trans. Nucl. Sci., NS-29 (1982) 2024.

[3.3] C. Hu, IEEE Electron Device Letters, EDL-3 (1982) 31.

[3.4] C. M. Hsieh, P. C. Murley, and R. R. O'Brien, IEEE Trans. Electron Devices, ED-30 (1983) 686.

[3.5] H. L. Grubin, J. P. Kreskovsky, and B. C. Weinberg, IEEE Trans. Nucl. Sci., NS-31 (1984) 1161.

[3.6] F. B. McLean and T. R. Oldham, IEEE Trans. Nucl. Sci., NS-29 (1982) 2018.

[3.7] J. A. Zoutendyk, L. S. Smith, G. A. Soli, and R. Y. Lo, IEEE Trans. Nucl. Sci., NS-34 (1987) 1292.

[3.8] T. R. Oldham and F. B. McLean, IEEE Trans. Nucl. Sci., NS-30 (1983) 4493.

[3.9] E. J. Kobetich and R. Katz, Phys. Rev., 170 (1969) 405.

[3.10] J. C. Pickel and J. T. Blandford, Jr., IEEE Trans. Nucl. Sci., NS-25 (1978) 1166.

[3.11] R. M. Gilbert, G. K. Ovrebo, and J. Schifano, IEEE Trans. Nucl. Sci., NS-32 (1985) 4098.

[3.12] T. R. Oldham, F. B. McLean, and J. M. Hartman, IEEE Trans. Nucl. Sci., NS-33 (1986) 1646.

[3.13] G. Jaffe, Ann. Phys., 42 (1913) 303.

[3.14] W. G. Abdel-Kader, P. J. McNulty, S. El-Teleaty, and J. E. Lynch, IEEE Trans. Nucl. Sci., NS-34 (1987) 1300.

[3.15] C. M. Hsieh, P. C. Murley, and R. R. O'Brien, IEEE Electron Device Letters, EDL-2 (1981) 103.

[3.16] J. P. Kreskovsky and H. L. Grubin, Solid-St. Electron., 29 (1986) 505.

[3.17] J. P. Kreskovsky and H. L. Grubin, "Simulation of the Response of GaAs JFET to Single Particle Radiation in Two and

Three Dimensions," presented at 6th Ann. Symp. on Single Event Effects (Los Angeles, CA, April 1988).

[3.18] J. P. Kreskovsky and H. L. Grubin, J. Comput. Phys., 68 (1987) 420.

[3.19] J. A. Zoutendyk, E. C. Secrest, and D. F. Berndt, IEEE Trans. Nucl. Sci., NS-35 (1988) 1573.

[3.20] J. S. Fu, H. T. Weaver, R. Koga, and W. A. Kolasinski, IEEE Trans. Nucl. Sci., NS-32 (1985) 4145.

[3.21] D. K. Nichols, W. E. Price, and C. J. Malone, IEEE Trans. Nucl. Sci., NS-30 (1983) 4520.

[3.22] T. L. Criswell, D. L. Oberg, J. L. Wert, P. R. Measel, and W. E. Wilson, IEEE Trans. Nucl. Sci., NS-34 (1987) 1316.

[3.23] R. S. Wagner, N. Bordes, J. M. Bradley, C. J. Maggiore, A. R. Knudson, and A. B. Campbell, IEEE Trans. Nucl. Sci., NS-35 (1988) 1578.

[3.24] Y. Song, K. N. Vu, J. S. Cable, A. A. Witteles, W. A. Kolasinski, R. Koga, J. H. Elder, J. V. Osborn, R. C. Martin, and N. M. Ghoniem, IEEE Trans. Nucl. Sci., NS-35 (1988) 1673.

Chapter 4

ION TRACK FORMATION MODEL

4.1 Introduction

Simulation of the ion-induced transient current pulse depends on assumptions used for initial ion track profiles such as peak charge density, effective track width, and spatial density profile. Most previous efforts assume simplified initial charge track profiles of uniform 10^{18} cm^{-3} densities over a fixed radius. Such assumptions miss details such as the significance of Auger recombination as a charge removal mechanism for realistic peak densities of 10^{20} cm^{-3}, and may underestimate the actual track size because the effect of energetic secondary electrons created in the wake of ion passage are not considered.

In cyclotron simulations of device upset, use of non-cosmic ions to simulate cosmic ions with comparable LETs assumes that comparable electronic effects should be expected. Unfortunately, the comparability of the axial and radial energy deposition profiles and the resulting track structure is less certain. If significant differences exist, the accuracy of such testing may be compromised.

To evaluate the impact of these assumptions on SEU computer and cyclotron simulation results, and to avoid these assumptions in our simulations, we have implemented a more realistic Monte Carlo-based analysis of secondary electron (SE) generation and transport and track formation within an ion transport code. The SEs are generated

using the binary collision approximation and transported with an electron slowing-down subroutine following the method of Fitting and Reinhardt [4.1]. Electron transport involves both elastic and inelastic scattering, and includes core electron ionization and dielectric energy loss mechanisms. These SEs, with keV energies, can travel far from the ion track and significantly increase the track size. As a result of this effort, the ion transport code TRIPOS [4.2,4.3] was extended to a new version, TRIPOS-E [4.4,4.5], which can solve the coupled ion-electron transport problem to analyze charge generation and track size in SEUs.

4.2 Mechanisms of Ion Track Formation

4.2.1 Electronic Energy Loss

The slowing down of ions within the target material consists of two components: interaction with the target electrons and interaction with the nuclei. Electronic stopping is the dominant mechanism. At high ion velocities $v > v_o Z_1^{2/3}$ (where $v_o \simeq c/137$ with c the speed of light) the electronic stopping power can be represented by the Bethe-Bloch formula:

$$[S_e(E)]_{BB} = \frac{\Delta E}{\Delta x} = \frac{\pi Z_1^2 Z_2 q^4 N}{E} \log\left[\frac{T_{max}}{T_{min}}\right] \frac{eV}{\mathring{A}} . \tag{4.1}$$

Z_1 and Z_2 are the atomic numbers of the incident and target atoms respectively, q is the electronic charge, N is the target atom

density, E is the incident ion energy, T_{min} corresponds to the mean ionization energy of the target atoms, and T_{max} represents the maximum kinetic energy transferable to a target particle:

$$T_{max} = \frac{4m_1 m_2}{(m_1 + m_2)^2} E \quad . \tag{4.2}$$

The electronic energy loss is then given by:

$$\Delta E = S_e \cdot \Delta x \tag{4.3}$$

along any path length Δx between successive scatterings of the incident ion. At low velocities $v \ll v_o Z_1^{2/3}$, the electonic stopping power is represented by the Lindhard-Scharff formula:

$$[S_e(E)]_{LS} = \frac{1.212\ Z_1^{7/6}\ Z_2\ N}{(Z_1^{2/3} + Z_2^{2/3})^{3/2}\ M_1^{1/2}} E^{1/2} \quad , \tag{4.4}$$

and in the intermediate regime by the Biersack interpolation scheme:

$$(S_e)^{-1} = (S_e)^{-1}_{LS} + (S_e)^{-1}_{BB} \quad . \tag{4.5}$$

In the Bethe-Bloch regime, the cross section for electronic energy transfer is represented by the Rutherford cross section:

$$d\sigma = \pi \left[\frac{b}{2}\right]^2 T_{max} \frac{dT}{T^2} \quad , \tag{4.6}$$

where b is the impact parameter and T represents the kinetic energy transferred to the target particle.

The Bethe-Bloch theory, which considers energy loss to be a continuous process through interaction with the electron cloud of the medium, accurately accounts for the transport of electrons with kinetic energies above 10 keV. However, as energies decrease from 10 keV, agreement between the Bethe-Bloch analysis and experimental results becomes poorer [4.6]. For this reason, we need to model low-energy electron transport by individual interaction mechanisms rather than a continuous energy-loss process.

Electron transport interaction mechanisms are divided into elastic and inelastic collisions. Elastic collisions, or Rutherford scattering, involve scattering of the electron by the atomic nuclei with no kinetic energy lost by the electron. Inelastic interactions involve energy loss by the electron, and consist of either ionization of core electrons or dielectric interaction with the valence electrons. The dielectric energy loss can be further divided into individual or collective electron-electron interactions (i.e., generation of either e-h pairs or plasmons). This is schematically shown in Figure 4.1.

4.2.2 Elastic Scattering

Two standard approaches are applied to the elastic scattering of electrons: Rutherford scattering and the partial waves method (PWM). For electrons with energies of 10 keV and above, the screened Rutherford interaction potential can be used for Coulombic scattering [4.1]. This potential incorporates a screening parameter which

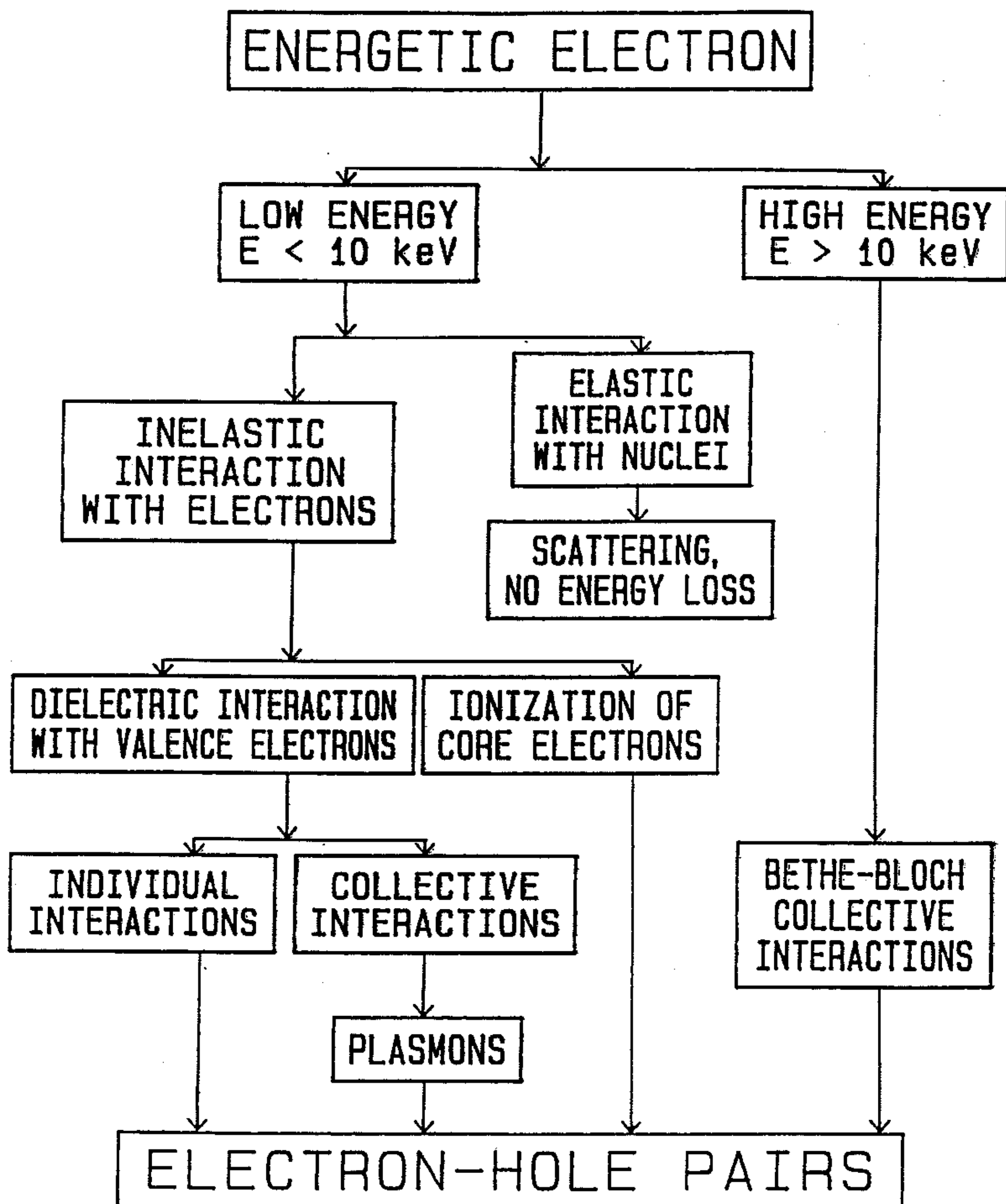

Figure 4.1: Flowchart of electron slowing-down interactions.

reflects the screening of the nuclear charge by the surrounding bound electrons as a function of distance from the nucleus. The screened Rutherford potential is given by reference [4.1]:

$$V(r) = - \frac{Ze}{4\pi\epsilon_o} \frac{1}{r} \exp\left[- \frac{r}{r_s} \right] , \tag{4.7}$$

with Z the atomic number of the target nucleus. The screening radius r_s is proportional to $Z^{-1/3}$. The angular distribution for elastic scattering is given by reference [4.1]:

$$\frac{d\sigma_{e\ell}}{d\Omega} = \frac{Z^2 e^4}{(4\pi\epsilon_o)^2} \frac{1}{4E^2} \frac{1}{(1 - \cos\alpha + 2a_s)^2} , \tag{4.8}$$

where E is the incident energy and α the polar scattering angle of the scattered electron. The screening parameter a_s is given by reference [4.1]:

$$a_s = \frac{\hbar^2}{8m_e E} \frac{1}{r_s^2} . \tag{4.9}$$

Integration of equation (12) gives the total scattering cross section:

$$\sigma_{e\ell}(E) = \frac{2\pi Z^2 e^4}{(4\pi\epsilon_o)^2} \frac{1}{4E^2} \frac{1}{2a_s(1 + a_s)} . \tag{4.10}$$

The mean-free path for Rutherford scattering is simply given by:

$$\lambda_{e\ell} = [N\sigma_{e\ell}]^{-1} , \tag{4.11}$$

with N the atomic density. Different expressions for the screening parameter a_s are available (e.g. Nigam et al. [4.7] and Wentzel [4.8]). Although calculations are straightforward, these equations give increasing error at low electron energies of a few keV or less; Akkerman and Chernov [4.6] compare these results with those of the PWM.

The PWM employs a quantum mechanical approximation for elastic scattering [4.9,4.10]. The concept of wave-particle duality allows the incident particles to be considered as waves. The incident particle flux is then considered as a superposition of plane waves, and the scattering center is considered to be the source of a weak spherical reflected wave. Superposition of the incident plane waves and outgoing spherical waves represents the effect of scattering. The perturbation becomes smaller with distance from the scattering center, and the superimposed waves asymptotically approach a plane wave. The magnitude of initial propagation constant k is the same, but the wave has a different direction and a different phase shift δ_ℓ after scattering. For elastic scattering of electrons by aluminum, Ganachaud and Cailler [4.11] used a muffin-tin potential evaluated by Smrčka [4.12] to obtain the principal phase shifts. Akkerman and Gibrekhterman [4.13] employed a PWM analysis for scattering by Aℓ, Au, Ge, Si, and Be using an independent-particle-model potential obtained by Green et al. [4.14]. Ichimura, Aratama, and Shimizu [4.15] used the Thomas-Fermi-Dirac potential in a PWM analysis of scattering by Aℓ, Cu, Ag, and Au.

Fitting and Reinhardt [4.1] also performed PWM analyses for Au, Si, SiO_2, and PMMA, but then compared the results to those of Rutherford scattering using the screening parameter

$$\tau(E) \simeq 0.9 + \exp(-E/E_\tau) \quad , \qquad (4.12)$$

which is related to the screening radius r_s of equations (4.7) and (4.9) by:

$$r_s = \frac{a_B}{Z^{1/3}} \left[\frac{0.885}{\tau}\right] \quad , \qquad (4.13)$$

where a_B is the Bohr radius. By choosing appropriate values of E_τ, they obtained good agreement between the two methods of calculation. We employed the formulas of Fitting et al. for elastic scattering cross sections in this analysis to reduce computational effort.

4.2.3 Core Electron Ionization

Ionization of core electrons within a material can be a significant energy loss mechanism for an energetic electron. A semi-classical approach for core ionization cross sections is given by Gryzinski [4.16]:

$$\sigma_j(E) = \frac{\pi e^4 n_j}{E_j^2} \frac{1}{\xi} \left[\frac{\xi - 1}{\xi + 1}\right]^{1.5} \left\{1 + \frac{2}{3}\left(1 - \frac{1}{2\xi}\right) \ell n[2.7 + (\xi - 1)^{0.5}]\right\}, \qquad (4.14)$$

where $\xi = E/E_j$ with E_j the binding energy for each j-shell and n_j the number of electrons in the jth shell. The total ionization cross

section is obtained by summing over all j-shells. This expression for core ionization cross section was used by Akkerman et al. [4.13], Ichimura and Shimizu [4.17], and others. Fitting et al. [4.1] note that the core ionization stopping power can be represented in a form similar to the Bethe-Bloch equation:

$$- \frac{dE}{ds} = A \frac{1}{E^p} \ell n \left[B \frac{E}{I_C} \right] \quad . \tag{4.15}$$

The effective mean-free path for core ionization is then given by:

$$\lambda_c = - \frac{\Delta E_c}{dE/ds} \quad . \tag{4.16}$$

Fitting et al. note that the constants B and p in equation (4.15) approximately equal 1. By ignoring any kinetic energy transfer to the ionized core electrons, ΔE_c of equation (4.16) is then approximately equal to the mean core-ionization energy, I_C. Equation (4.16) then takes the form:

$$\lambda_c = \frac{I_C \; E}{A \; \ell n(E/I_C)} \quad . \tag{4.17}$$

For silicon, Fitting et al. give values of 100 eV for I_C and 300 $eV^2/\text{Å}$ for the constant A. The mean-free path for core ionization can then be directly calculated as a function of incident electron energy. The polar scattering angle can be approximated by a free collision momentum transfer:

$$\sin^2 \alpha \simeq I_C/E \quad . \tag{4.18}$$

4.2.4 Dielectric Energy Losses

An energetic electron can transfer energy to valence-band electrons by either plasmon production or creation of e-h pairs. Some previous modeling of electron transport uses detailed analytical expressions for dielectric energy losses by both mechanisms. For example, Akkerman et al. [4.13] uses expressions given by Ferrell [4.18] and Ritchie [4.19]. Rather than performing calculations as detailed as those above, Fitting et al. use a simple scheme based on the previously defined core ionization mean-free path and an empirical expression for inelastic mean-free path:

$$\lambda_{in} \simeq 0.25\ E^{0.6} + 1 \quad , \tag{4.19}$$

applicable for electron energies between 70 eV and 10 keV. With λ_{in} and λ_C previously calculated, the equality:

$$\frac{1}{\lambda_{in}} = \frac{1}{\lambda_C} + \frac{1}{\lambda_D} \quad , \tag{4.20}$$

allows the mean-free path for dielectric interaction, λ_D, to be obtained directly.

4.2.5 Higher-Energy Electron Transport

Transport of secondary electrons with energies above 10 keV can be accurately represented by a Bethe-Bloch formulation similar to equation (4.1). A continuous energy-loss mechanism to the bulk electrons between elastic scatterings is assumed. The elastic scattering cross section is again given by equation (4.10), but now the screening parameter τ of equation (4.12) is set equal to 1. A typical Bethe-Bloch energy-loss equation for electrons is that used by Shimizu et al. [4.20]:

$$\frac{dE}{dx} = -2\pi e^4 \frac{NZ}{E} \ell n \frac{1.166E}{J} , \qquad (4.21)$$

where the mean ionization potential J can be given by [4.21]:

$$J = Z\left[14(1 - e^{-0.1Z}) + \frac{75.5}{Z^{Z/7.5}} - \frac{Z}{100 + Z}\right] . \qquad (4.22)$$

Other formulas for J exist but give similar results (e.g. [4.13]).

4.3 Modeling Methodology

TRIPOS was developed by Chou and Ghoniem to study ion transport in solids using the Monte Carlo (MC) technique for the solution of the transport equation [4.2,4.3]. The MC technique uses random determination of the interaction parameters as defined by the governing equations. A sufficiently large collection of simulated

particles should give a statistically valid average which is representative of actual behavior. TRIPOS is distinguished from other ion transport codes by its use of the power-law approximation to the Thomas-Fermi potential in the region between high ion energy (pure Coulombic interaction) and low ion energy (represented by a Born-Mayer interaction potential), by its use of a number of variance reduction techniques, and its extension to applications such as surface sputtering.

Details of the calculation of individual scattering probabilities and scattering angles are given in more detail by Martin and Ghoniem in references [4.4] and [4.22]. The Monte Carlo approach is used for both generation and transport of these high-energy secondary electrons. The basic MC scheme is as follows. One random number is chosen to represent the energy transfer to the SE according to equation (4.6), while another gives the position of SE generation along the ion path. The path length of the SE between subsequent collisions is given by [4.13]:

$$\lambda = - \lambda_{tot} \ln(\xi) = - (\Sigma\lambda_i^{-1})^{-1} \ln(\xi) \quad , \qquad (4.23)$$

with λ_i and λ_{tot} the individual and total mean-free paths, respectively, and ξ a random number between 0 and 1. The choice of interaction i is determined by their relative probabilities, using another random number. Most energy loss and scattering angle determinations also employ random numbers.

The rate of energy loss by energetic ions to electrons is given by the Bethe-Bloch equation [equation (4.1)]. The energy transfer

mechanism from an ion to electrons is represented by the Rutherford cross section of equation (4.6), with the probability of energy transfer inversely proportional to the square of the amount of kinetic energy transferred to the secondary electrons. Figure 4.2 shows that most SEs receive lower kinetic energies with a small but significant fraction receiving energies of a few keV. To evaluate the distances traveled by the high energy fraction, an arbitrary cutoff energy T_c is used to separate the secondary electrons into two groups: those receiving kinetic energies of magnitude greater than T_c and those with energies less than T_c. T_c is typically chosen to be 0.5 to 1.0 keV. Energy transfers greater than T_c are viewed as

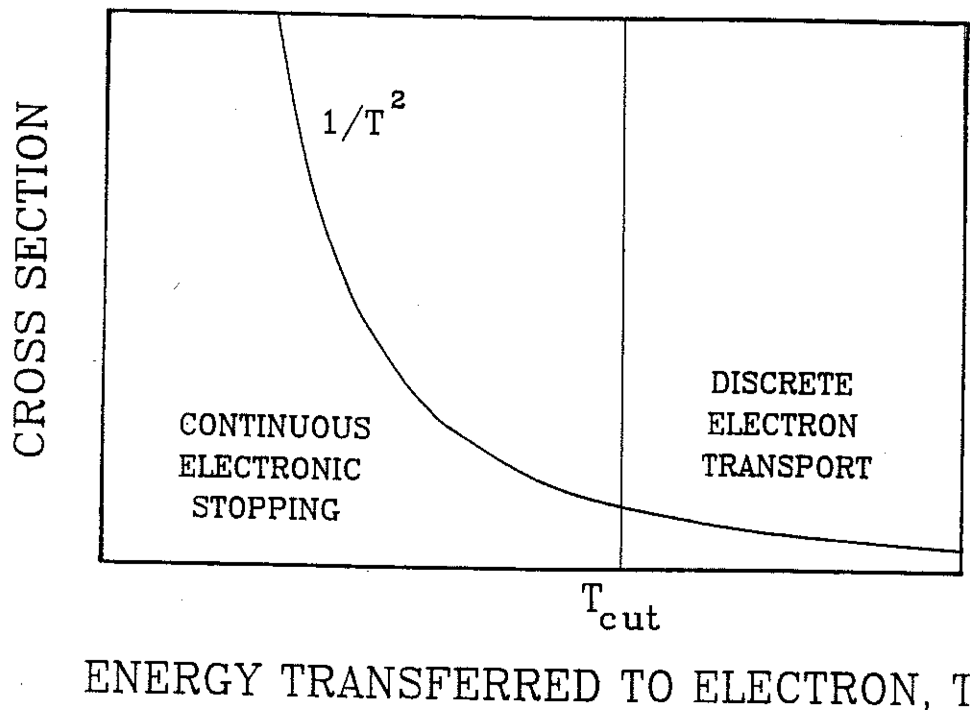

Figure 4.2: Relative cross section for energy transfer.

discrete energy transfers to electrons. These SEs can dissipate their energy far from the ion path. Energy transfers less than T_c are considered to represent continuous energy transfer, localized to e-h pairs close to the ion path.

The Bethe-Bloch theory accurately accounts for the transport of electrons with kinetic energies above 10 keV. TRIPOS-E contains a subroutine for those few SEs with energies above 10 keV, similar to the Bethe-Bloch formulation for ions of equation (4.1); a continuous energy-loss mechanism to the bulk electrons between elastic scatterings is assumed. At lower energies, better results are obtained using individual interaction mechanisms rather than a continuous energy-loss process. In the keV regime of SEs, four mechanisms must be considered: elastic Rutherford scattering and the inelastic interactions of core electron ionization, plasmon generation, and e-h pair generation. These slowing-down mechanisms are shown in the flowchart of Figure 4.1.

An additional routine is included for secondary electrons with energies above 10 keV, similar to A continuous energy-loss mechanism to the bulk electrons between elastic scatterings is assumed.

Use of T_c allows the Bethe-Bloch equation [equation (4.1)] to be modified as follows:

$$S_e = C \log\left[\frac{T_{max}}{T_{min}}\right] = C \log\left[\frac{T_{max}}{T_{cut}} \cdot \frac{T_{cut}}{T_{min}}\right] ,$$

or (4.24)

$$S_e = C \log\left[\frac{T_{max}}{T_{cut}}\right] + C \log\left[\frac{T_{cut}}{T_{min}}\right] ,$$

where C is the collection of constants in equation (4.1). TRIPOS calculates S_e for the ion from one scattering event to the next. This equation gives the relative contributions of each energy regime to the electronic stopping of the ion.

The probability distribution function (pdf) for kinetic energy transfer to electrons is given by equation (4.6) and Figure 4.2. Integration between T_{max} and T_{cut} gives the cumulative distribution function (cdf):

$$cdf = \left[\frac{T_{max} \cdot T_{cut}}{T_{max} - T_{cut}}\right] \left[\frac{1}{T_{cut}} - \frac{1}{T}\right] , \qquad (4.25)$$

where T is the actual kinetic energy transferred to the electron. Curves of the cdf are shown in Figure 4.3 for a typical krypton-silicon interaction for different values of T_{cut}. By choosing a random number between zero and one and equating it with the cdf, the corresponding energy transfer is calculated directly. Another random number is generated to represent the position of secondary-electron generation along the ion path between successive nuclear collisions. The kinetic energy of the generated electron is compared to the magnitude of the discrete component of the electronic energy loss (to secondary electrons) between the successive nuclear scatterings. This comparison gives the relative weight of each electron (i.e. the discrete energy component divided by the electron energy):

$$weight = \Delta E_d / E_{el} \quad . \qquad (4.26)$$

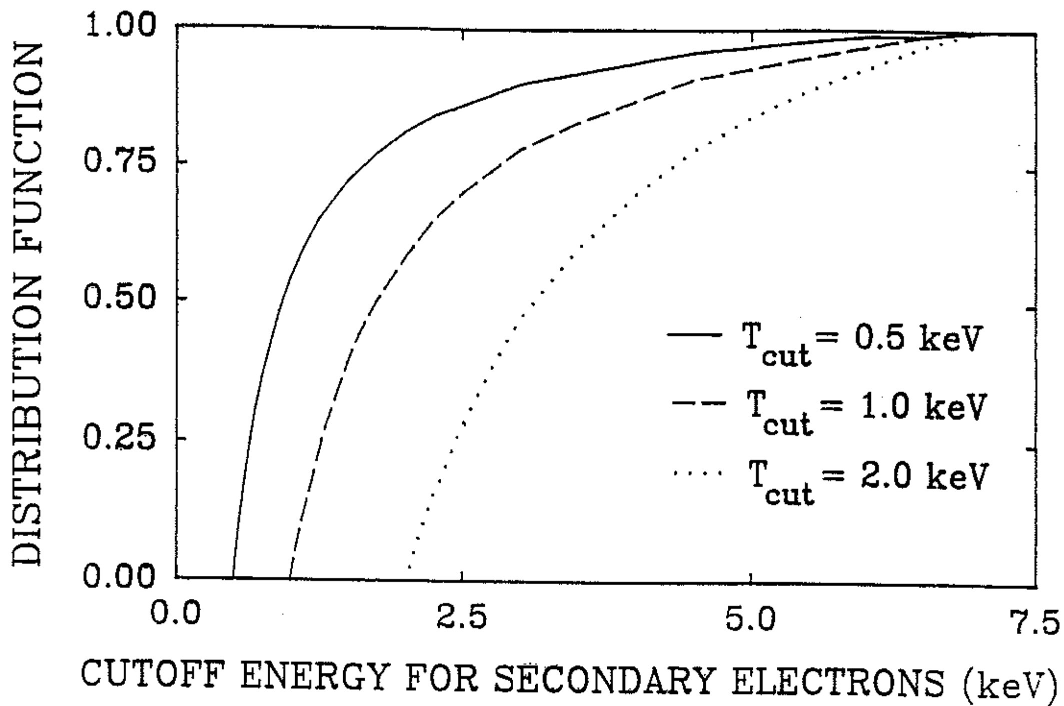

Figure 4.3: Cumulative distribution functions as a function of the cutoff energy for secondary electron generation, for an incident 270 MeV krypton ion.

If this weight is less than 1.0, the discrete component of electronic energy loss between the two scatterings is not sufficient for secondary-electron generation, and this electron is discarded. If sufficient discrete energy exists for generation of additional electrons, they are created based on the conservation of discrete energy transfer. A flowchart for SE creation within the ion transport code is given in Figure 4.4.

After creation of the electrons, each one moves according to an electron transport scheme similar to that proposed by Fitting et al. [4.1]. The routine of Fitting et al. was implemented with alterations in path-length and inelastic mean-free path

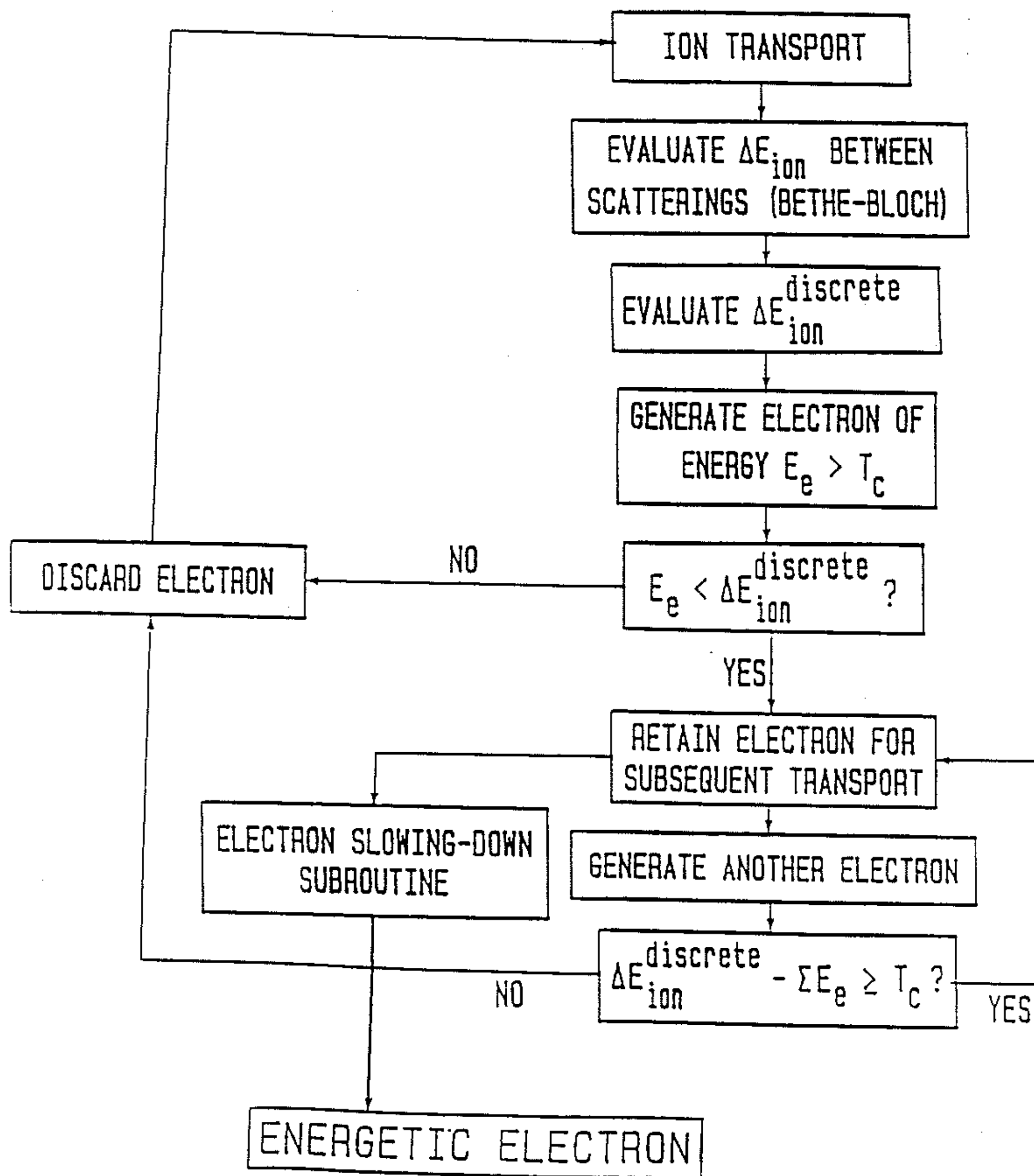

Figure 4.4: Flowchart for secondary electron generation within the ion transport code TRIPOS-E.

determinations. To determine the path length between electron interactions, Fitting et al. propose the following scheme:

$$\left| \frac{\Delta s}{\lambda_{e\ell}} \left| \frac{\Delta s}{\lambda_c} \right| \frac{\Delta s}{\lambda_D} \right| \text{ no interaction } \Big| \quad , \qquad 0 \longleftarrow R_i \longrightarrow 1 \tag{4.27}$$

where the random number R_i determines which interaction of the energetic electron, if any, occurs. The path length between interactions, Δs, is taken to be:

$$\Delta s \approx 0.7 \cdot \lambda_{tot} = 0.7(\Sigma\, \lambda_i^{-1})^{-1} \quad . \tag{4.28}$$

For each electron traversing a path length Δs, this approach results in a 70% probability of collision. We use the more traditional Monte Carlo approach is the use of a random number determination for both path length and interaction mechanism. The path length is given by [4.13]:

$$\lambda = -\lambda_{tot}\, \ell n(\xi) = -(\Sigma\, \lambda_i^{-1})^{-1}\, \ell n(\xi) \quad , \tag{4.29}$$

with ξ some random number between 0 and 1. The type of interaction i is determined from:

$$P_{i-1} \le \xi \le P_i \quad , \tag{4.30}$$

where $P_0 = 0$, $P_1 = \lambda_{tot}/\lambda_{e\ell}$, $P_2 = \lambda_{tot}(\lambda_{e\ell}^{-1} + \lambda_D^{-1})$, and $P_3 = \lambda_{tot}(\lambda_{e\ell}^{-1} + \lambda_D^{-1} + \lambda_C^{-1}) = 1$. This scheme is computationally more efficient by having a collision at the end of each path length. It was found to give results for electron range as a function of energy

similar to those of the scheme of Fitting et al. This random number scheme was therefore integrated into the present modeling effort.

For each interaction, both the energy lost by the electron and its polar scattering angle α_i must be determined. Elastic scattering results in no loss of kinetic energy; the angle of scattering is determined by another random number, $\xi_{e\ell}$ [4.1]:

$$\alpha_{e\ell} = \cos^{-1}\left[1 - \frac{2\, a_s\, \xi_{e\ell}}{1 + a_s - \xi_{e\ell}}\right] . \tag{4.31}$$

Core ionizations involve an energy loss of 100 eV and an angle of scattering given by equation (4.18).

Dielectric energy loss and scattering angle determinations are more involved. The approach of Fitting et al. is incorporated here. The magnitude of the dielectric energy loss is represented by the dielectric loss function, which for silicon is given in Figure 4.5 [4.24]. A random number gives the dielectric energy loss ΔE by application of the following equation:

$$R_D = \frac{\int_0^{\Delta E} \mathrm{Im}(-1/\epsilon)\, dE}{\int_0^{100eV} \mathrm{Im}(-1/\epsilon)\, dE} , \tag{4.32}$$

where the denominator represents the area under the curve in Figure 4.5. This integrated area was obtained as a function of ΔE, and a fit of this data allowed use of the random number scheme.

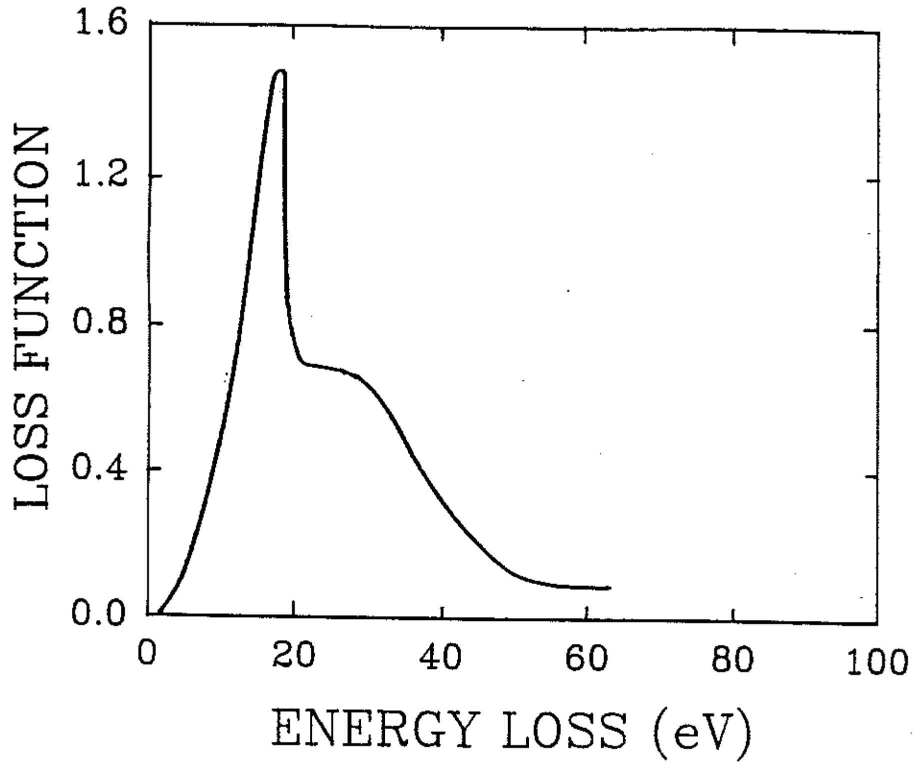

Figure 4.5: Dielectric loss function for silicon [4.24].

After ΔE is evaluated for each dielectric interaction, the dielectric scattering angle is obtained. A random number can be related to the dielectric scattering angle α_D by [4.1]:

$$R_\alpha = \frac{\ell n \dfrac{E + E' - 2(EE')^{0.5} \cos \alpha_D}{E + E' - 2(EE')^{0.5}}}{\ell n \dfrac{E + E' - 2(EE')^{0.5} \cos \alpha_f}{E + E' - 2(EE')^{0.5}}} , \qquad (4.33)$$

where E' is the energy of the electron after collision (equal to $E - \Delta E$) and α_f is a cutoff angle limited by the maximum wave vector:

$$\cos \alpha_f = \frac{2E - \Delta E - (h^2 q_{max}^2/2m_e)}{2E[1 - (\Delta E/E)]^{0.5}} , \qquad (4.34)$$

with $h^2 q_{max}^2/2m_e \simeq 20$ eV. The cutoff angle α_f is evaluated from equation (4.34). α_D is finally evaluated as:

$$\cos \alpha_D = \frac{E + E'}{2(EE')^{0.5}} (1 - B) + B , \qquad (4.35)$$

where B is given by:

$$B = \frac{E + E' - 2(EE')^{0.5} \cos \alpha_f}{E + E' - 2(EE')^{0.5}} . \qquad (4.36)$$

The above scattering angles represent deviations from the original trajectory of the electron. The azimuthal scattering angle is also determined randomly between 0 and 2π.

Fitting et al. state that equation (4.19) is largely material independent. Ashley and Tung [4.25] obtained material-specific equations for inelastic mean-free paths by analyzing experimental data. For silicon, they report the following:

$$\begin{aligned} \lambda_{in} &= 0.200\ E^{0.665} , && 200 < E < 400 \text{ eV} , \\ \lambda_{in} &= 0.108\ E^{0.768} , && 400 < E < 2000 \text{ eV} , \qquad (4.37) \\ \lambda_{in} &= 0.0611\ E^{0.843} , && 2000 < E < 10000 \text{ eV} , \end{aligned}$$

with the mean-free path λ given in Å and the energy E in eV. We found the results of Ashley et al. to give electron ranges in better agreement with an empirical range formula than those of Fitting et

al. A comparison between equation (4.19) of Fitting et al. for total mean-free path as a function of energy was compared to calculations by Akkerman et al. [4.23] and Ashley et al. [4.25] in Figure 4.6. To test the validity of the two mean-free path formulas, the routine of Fitting et al. was used to model electron penetration at a surface with normal angle of incidence, and the mean range of all non-backscattered electrons was compared to an empirical formula for mean projected range of electrons in silicon as a function of energy given by [4.26]:

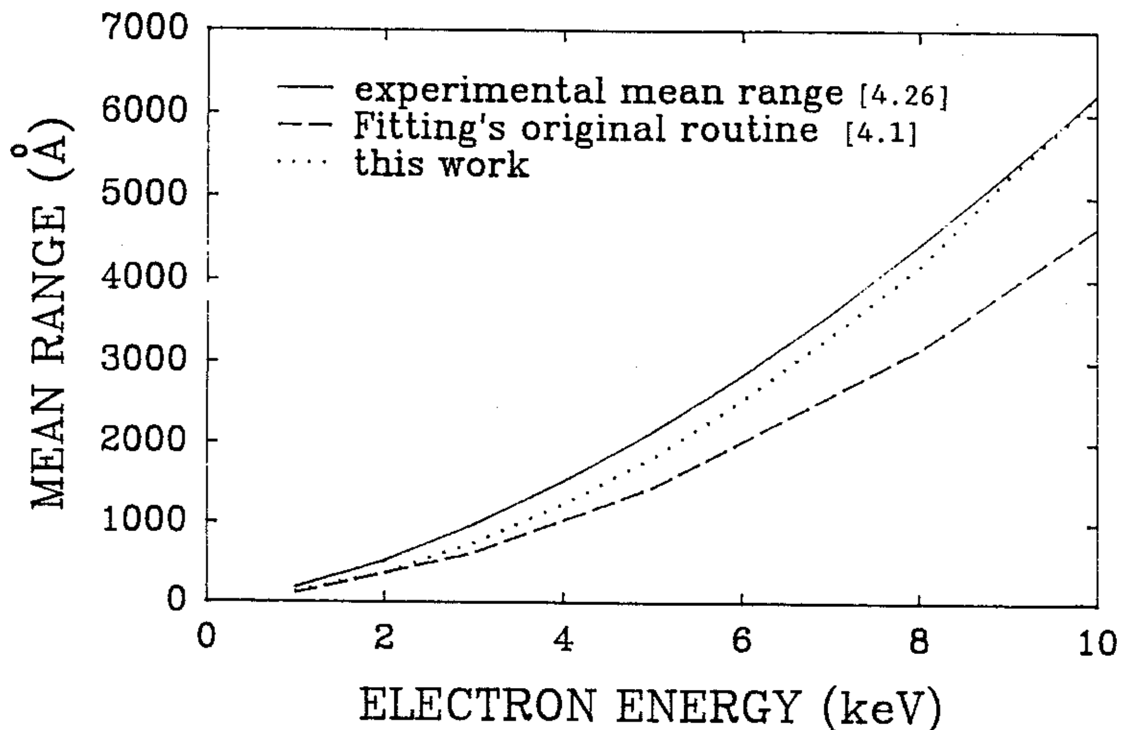

Figure 4.6: Comparison of electron mean-range formulations in silicon.

$$R = 180\ E^{1.54} \quad , \tag{4.38}$$

with R given in Å and E in keV. Figure 4.6 shows that the original routine of Fitting et al. gives mean ranges significantly lower than those determined experimentally. Equation (4.37) of Ashley et al. was then incorporated into the routine, and the range results give significantly better agreement (also Figure 4.6). Because of this, we used the equations of Ashley et al. in TRIPOS-E.

Different energy minima at which tracking of the electron was halted were compared. Because a minimum of 200 eV gives better agreement with equation (4.38) than lower energies, this minimum energy value is used. This choice also adheres to the lower limit of validity of equation (4.37).

4.4 Results

4.4.1 Secondary Electron Distributions

Four different incident high-energy ions of current interest are studied: 100 MeV proton, 180 MeV argon, 270 MeV krypton, and 1 GeV iron. Figure 4.7 shows typical tracks for the first three ions, where the endpoint of each generated secondary electron (i.e., the point where the kinetic energy falls below 200 eV) is plotted with respect to the ion path. Changes in the direction of the ion path because of collisions are not shown; a straight line path is simulated to better show the radial distribution.

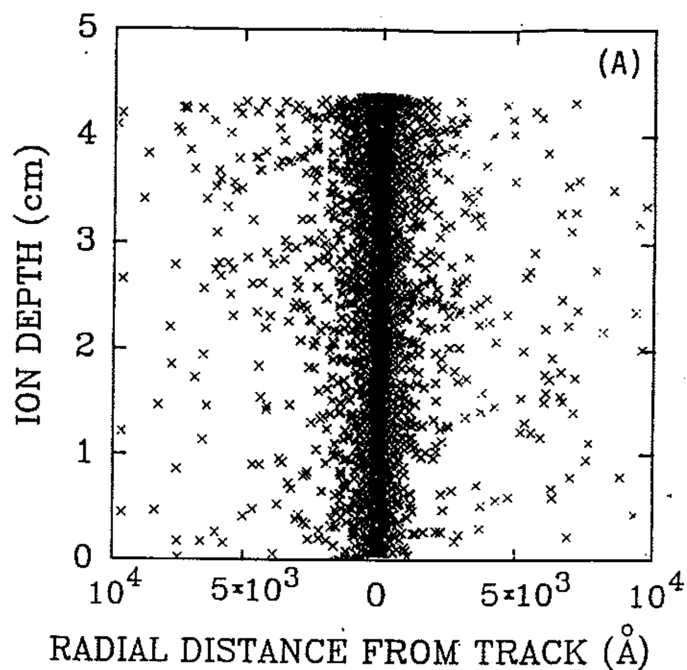

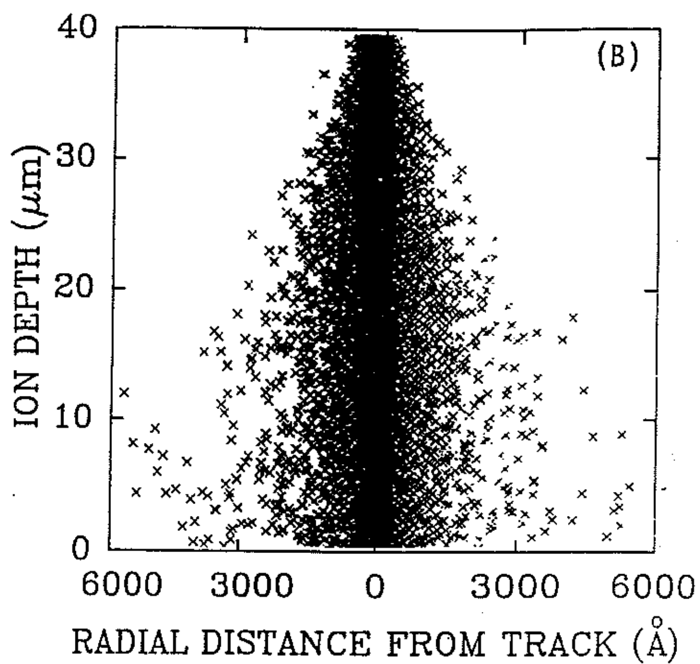

Figure 4.7: Two-dimensional profile of secondary electron ranges in silicon as a function of track depth for (a) 100 MeV proton, (b) 180 MeV argon, and (c) 270 MeV krypton ions.

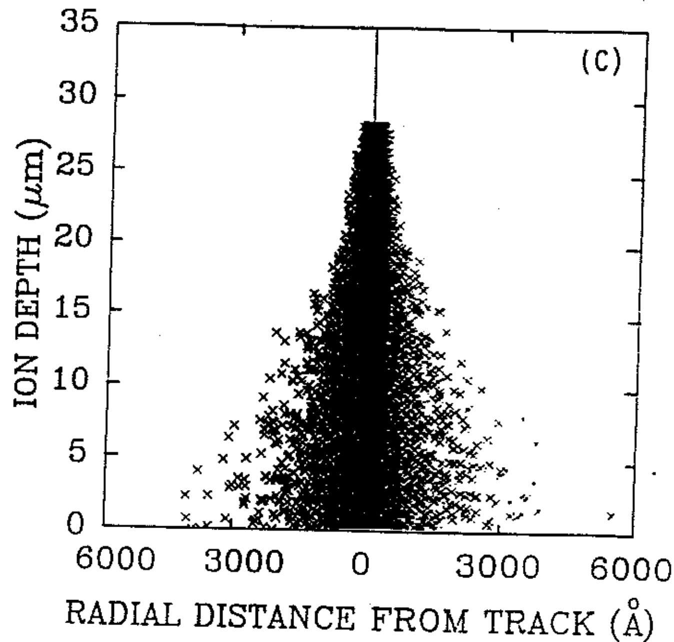

Figure 4.7: Two-dimensional profile of secondary electron ranges in silicon as a function of track depth for (a) 100 MeV proton, (b) 180 MeV argon, and (c) 270 MeV krypton ions.

The minimum energy of generated SEs is assumed to be 1 keV. As the ion loses energy it reaches a point toward the end of its track where it can no longer generate 1 keV secondaries. This point is particularly evident for the heavier ions. This phenomenon is in agreement with equation (4.2), which is used as the basis for this binary collision model of ion-electron collision and resultant secondary-electron generation.

The SEs generated by light ions have a higher average energy at creation than those from heavy ions and tend to travel further from the track. This fact is representative of better energy coupling between electrons and light ions, as expected from equation (4.2). For heavier ions, the initial energy of the secondaries at generation

decreases as the ion loses energy, resulting in a shorter range for the electrons generated further along the track. This result is apparent in the funnel-shaped tracks of Figures 4.7(b) and 4.7(c).

An evaluation was made of the average time spent by the electrons within each track between generation and reduction of energy below 200 eV. The time elapsed between interactions was calculated and summed for the total slowing-down time by knowing the distance between interactions and the kinetic energy of the electron. For all three types of ions, the average time is on the order of 10^{-14} s, indicating very rapid track formation. The range of a 200 eV electron in silicon is estimated to be 69 Å [4.27]; with this short range and the randomized direction of electron motion, further slowing down will not alter track profiles.

4.4.2 Electron-Hole Pair Distributions

Each secondary electron undergoes many inelastic collisions between generation and thermalization. With high initial energies, they can carry a significant portion of the ion's deposited energy far from the immediate vicinity of the track. To evaluate this energy deposition radially from the track, a series of concentric zones are set up around the track and energy losses by inelastic collisions within each zone are tabulated. These losses are considered to be deposited locally, and the radial e-h pair densities can be obtained by dividing the total energy deposition within each zone by the energy required to produce an e-h pair (i.e. 3.6 eV in

silicon). Once the radial distributions of e-h pairs are obtained, these results can be fit to an equation to express the distribution in a convenient form. As some track widths change with depth into the medium, several positions along the track are evaluated in terms of the energy deposition within a slice of the silicon material (e.g. a 1-μm-thick slice perpendicular to the direction of ion penetration).

Results are shown in Figure 4.8 for 180 MeV argon, 270 MeV krypton, and 1 GeV iron ions. An exponential tail is apparent for the charge distribution away from the central core of the ion path, suggestive of penetration by the high-energy SEs. The narrowing of

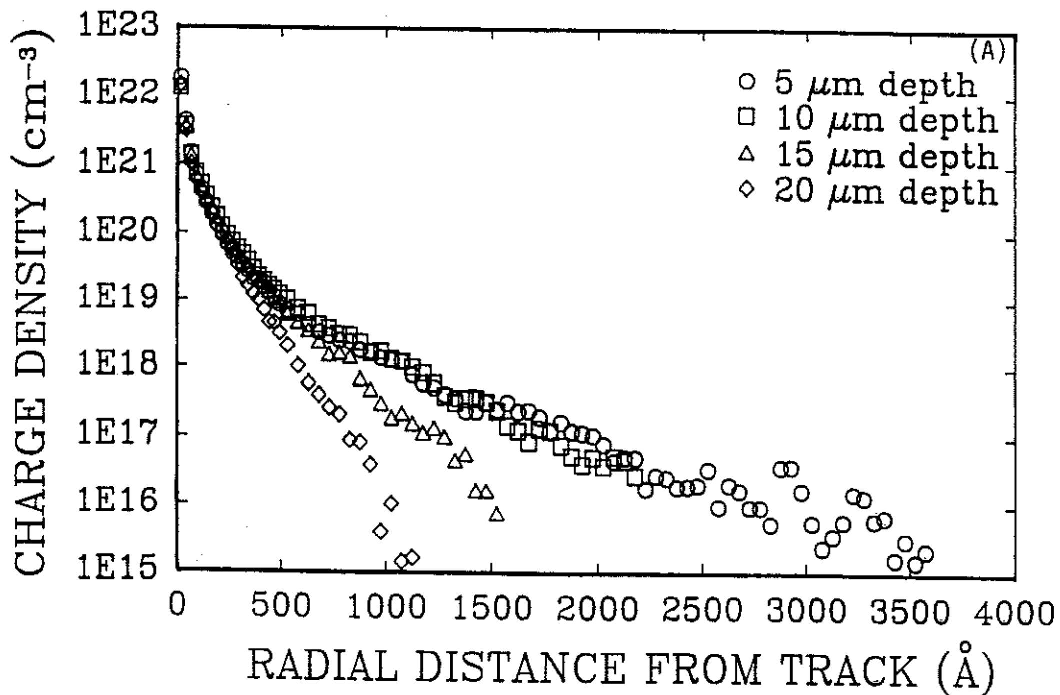

Figure 4.8: Radial volumetric charge density in silicon due to high-energy secondary electrons using T_{cut} = 1000 eV for (a) 270 MeV krypton, (b) 180 MeV argon, and (c) 1 GeV iron ions.

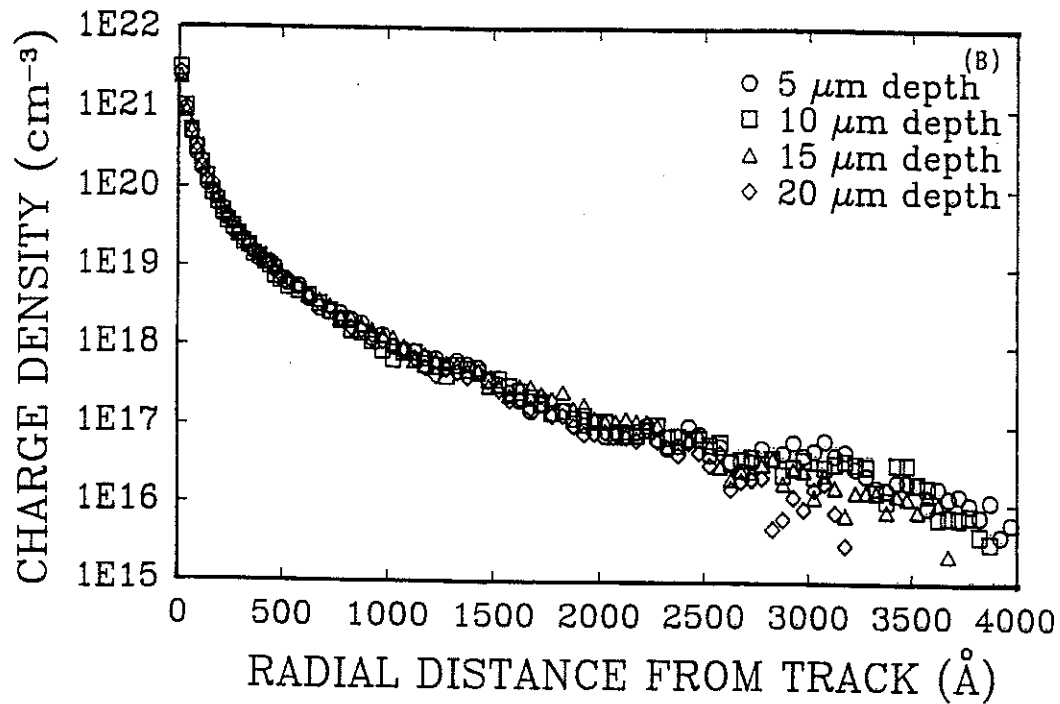

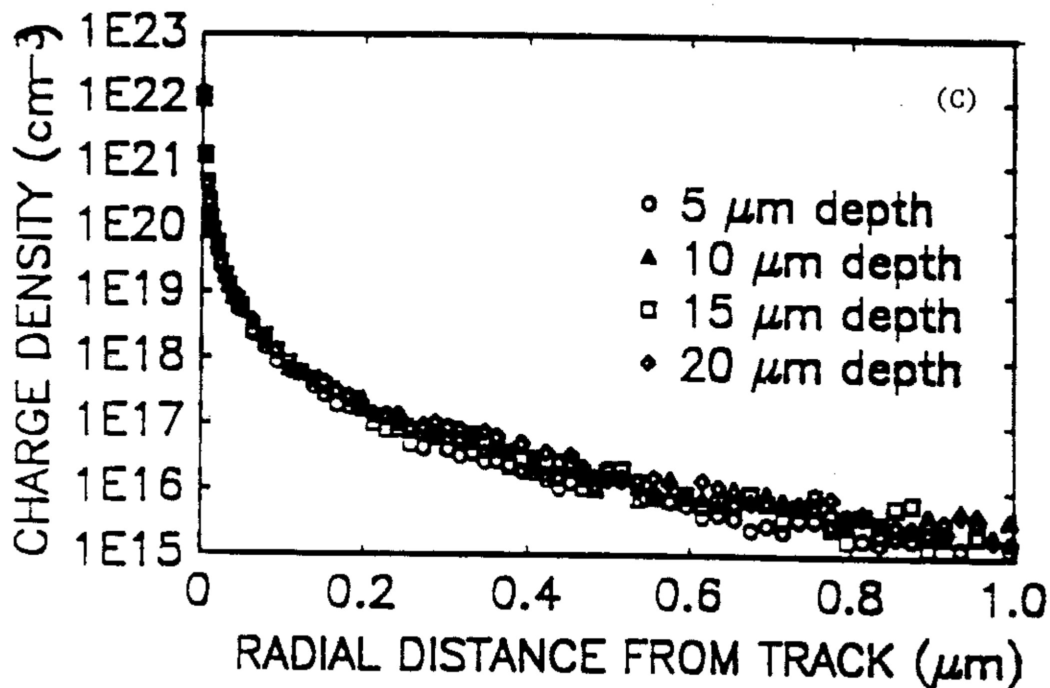

Figure 4.8: Radial volumetric charge density in silicon due to high-energy secondary electrons using T_{cut} = 1000 eV for (a) 270 MeV krypton, (b) 180 MeV argon, and (c) 1 GeV iron ions.

the charge-density profiles in Figure 4.8(a) for the krypton ion at increasing depth reflects the reduced probability of generation of secondaries above 1 keV as the ion loses energy. Figure 4.8(b) does not reflect this behavior as the argon ion travels significantly farther before losing a comparable amount of energy. Figure 4.8(c) shows significant energy deposition out to 1 μm radius for a high-energy heavy ion that might be encountered in space. A cutoff energy of 1 keV for secondary generation is used for these figures.

Charge generation arising only from the secondary electrons is reflected in Figure 4.8. The low-energy transfer to electrons below the cutoff energy must also be accounted for in a total charge-density profile. With a cutoff energy of 1 keV, these electrons would be expected to deposit their energy within a 200 Å core around the ion path, in agreement with equation (4.38). For this deposition, a Gaussian profile can be postulated similar to that of equation (3.2) which can also account for the non-exponential behavior of Figure 4.8 at small values of radial distance. Combining the Gaussian and exponential components in an expression for charge-density profile gives:

$$\eta(r) = C \frac{1}{r} [\exp(-r^2/b_1^2) + \xi \exp(-r/b_2)] \quad , \qquad (4.39)$$

where C is some constant, b_1 and b_2 are analogous to track widths for the Gaussian and exponential regions, respectively [as in equation (3.2)], ξ is a correlation factor between the two components, and the $1/r$ dependency reflects the cylindrical geometry. Equation (4.39)

can be integrated over r from zero to infinity to obtain the total charge deposition, which in turn provides an expression for the constant C and gives:

$$r\eta(r) = \frac{N_\ell}{\pi^{3/2}\ b_1 + 2\pi\xi b_2}\ [\exp(-r^2/b_1^2) + \xi\ \exp(-r/b_2)] \quad , \qquad (4.40)$$

where N_ℓ is the total charge deposition along a unit path length of the ion. Figure 4.9(a) is a conversion of Figure 4.8(a) to a graph of $\ell n[r\eta(r)]$ vs r, in which the exponential tail is still apparent. Note that the non-Gaussian portion of equation (4.40) can be expressed in the form:

$$\ell n[r\eta(r)] = \ell n\ \frac{N_\ell \xi}{\pi^{3/2}\ b_1 + 2\pi\xi b_2} - \frac{r}{b_2} \quad . \qquad (4.41)$$

The slope along the linear portion of Figure 4.9(a) provides a value for b_2, and extrapolation of the linear portion to $r = 0$ and comparison with equation (4.41) gives an expression for $\xi = \xi(b_1)$. The Gaussian component reflected by b_1 must account for the curved region of Figure 4.9(a) at small values of r plus an additional enhancement within that region due to the low energy transfers. Equation (4.40) can be converted into a form dependent only on r and b_1. This expression should give good agreement throughout the linear portion of Figure 4.9(a). Thus, a least-squares comparison of this equation to the data throughout the linear regime can provide the "best" value of b_1 while also accounting for all low-energy transfers within the assumed Gaussian regime. Once b_1 is determined, a value

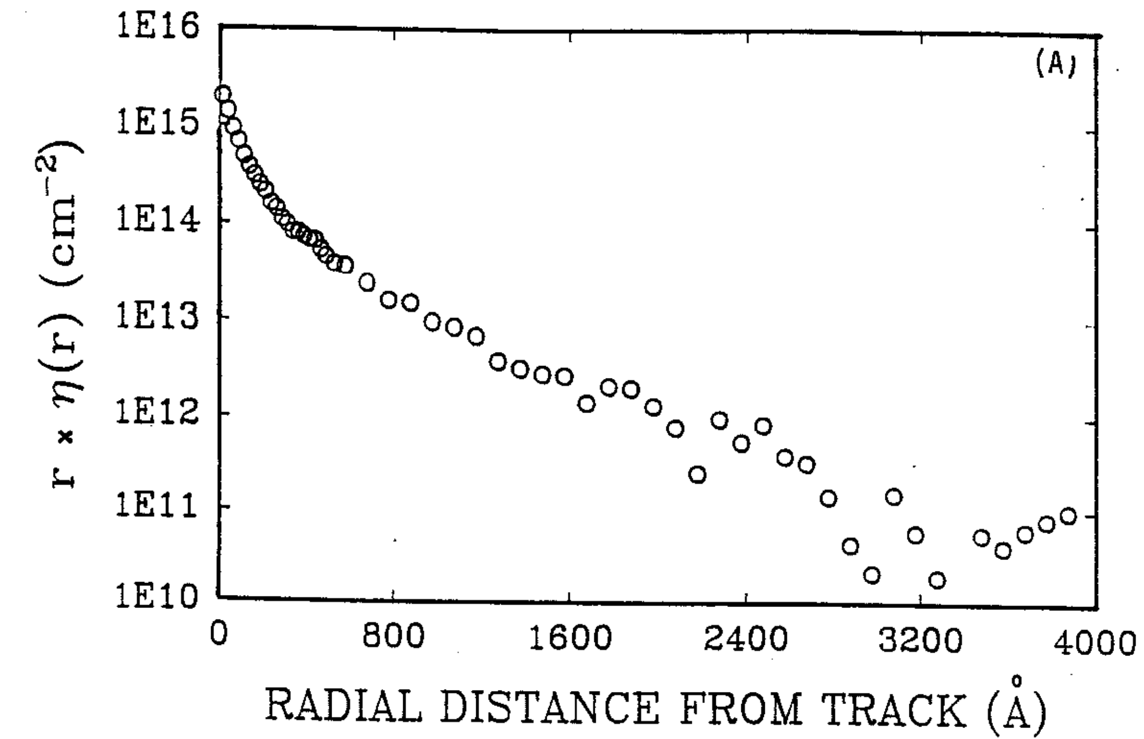

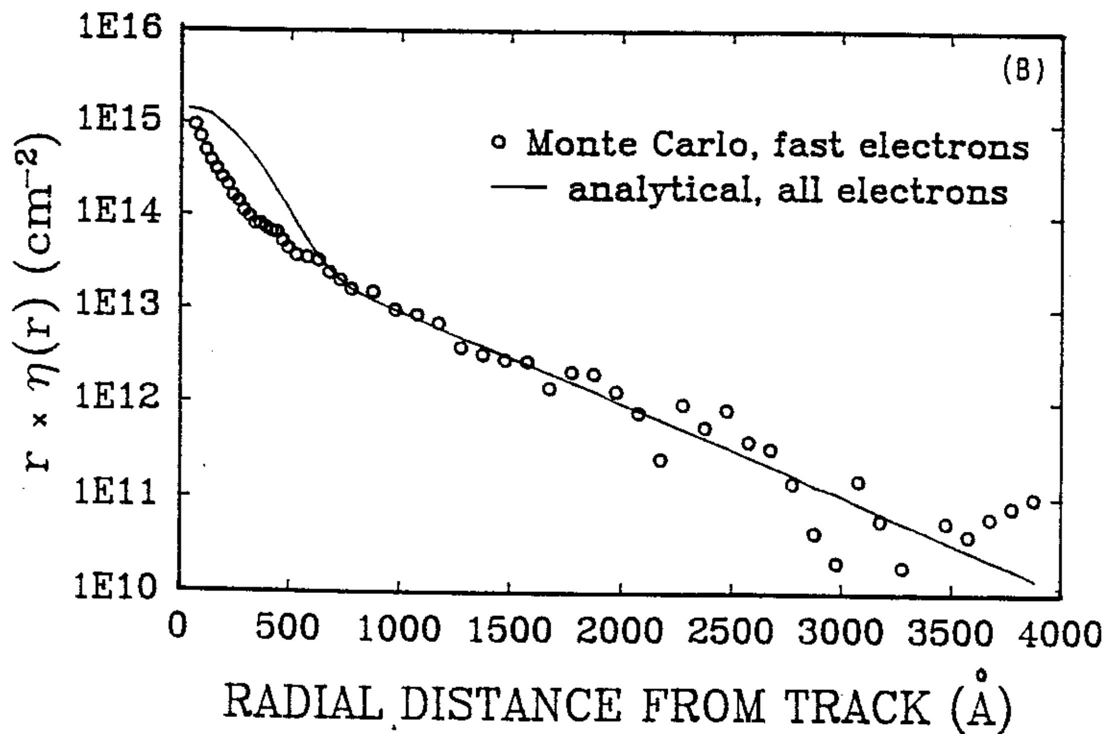

Figure 4.9: 270 MeV krypton ion incident on silicon, at 5 μm depth, using T_{cut} = 1000 eV: (a) radial charge surface density due to high-energy secondary electrons, obtained from TRIPOS-E; (b) comparison of the analytical formula to the computational results.

for the parameter ξ is obtained directly from the expression $\xi = \xi(b_1)$. Figure 4.9(b) shows the resulting analytical curve obtained from Figure 4.9(a).

Results for the radial distribution of e-h pairs can now be fit to the above equations to express the distribution in a convenient form. Given the total e-h pair generation within a region and the excess carrier profiles resulting from the high-energy secondary electrons as in Figure 4.8, the parameters b_1, b_2, and ξ can be evaluated to give an analytical expression for the e-h pair profiles at different depths of penetration [4.4]. Figure 4.10 shows the profiles given by the analytical expressions at different depths corresponding to Figure 4.8 for krypton. The higher density core

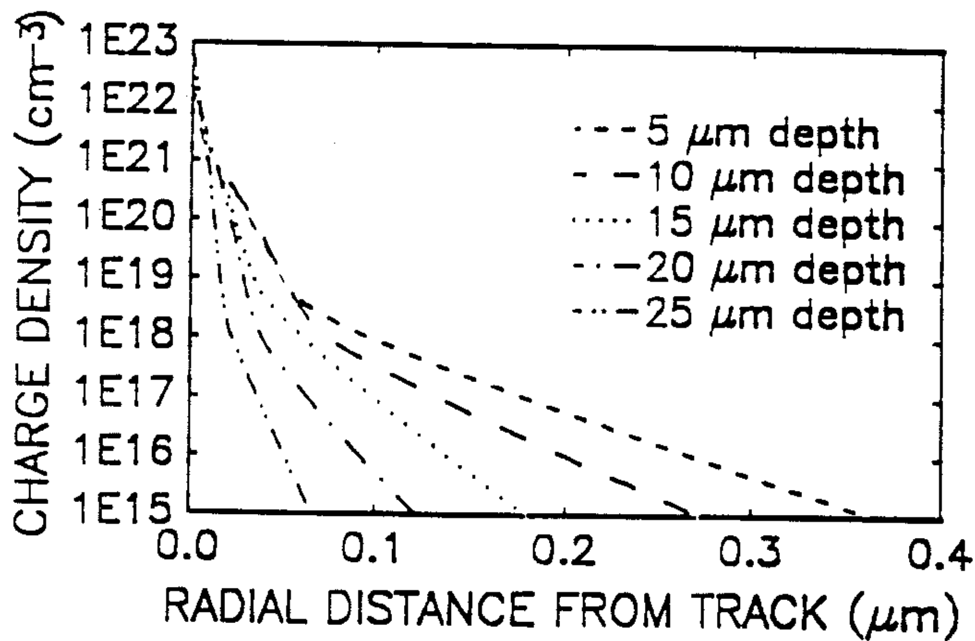

Figure 4.10: Radial volumetric charge-density profiles as a function of depth for 270 MeV krypton ion, given by the analytical formula, equation (4.39).

contains all low-energy transfers. Although peak densities exceed 10^{22} cm^{-3}, these core concentrations quickly decline due to Auger recombination of e-h pairs within the time frame of initial charge collection. Simulations of charge collection during SEUs show the initial current pulse to occur between 10 and 100 ps after the ion passes [4.28]. Within this time frame densities will decline to values on the order of 10^{20} cm^{-3}, a value in agreement with peak e-h pair concentrations generated during laser annealing of silicon [4.29].

To evaluate the effect of the choice of cutoff energy on the values of these parameters, several analyses are performed using cutoff energies ranging from 200 eV to 2 keV. Results for b_1 and b_2 for 270 MeV krypton and 180 MeV argon are plotted in Figure 4.11(a) and 4.11(b), respectively. For krypton, b_2 extrapolates to about 800 Å for a depth in silicon of 5 μm and drops off rapidly as the depth of penetration increases. For argon, b_2 extrapolates to approximately 1000 Å. Both ions give similar values for b_1: approximately 300 Å for krypton and 400 Å for argon. Values for ξ range between 0.06 and 0.16 for both ions. These results are listed in Table 4.1.

In general, extrapolation of track parameters as a function of T_c indicated lower values of T_c to give more consistent results; a value of 500 eV for T_c was used in most calculations. Results for b_1 and b_2 for 270 MeV krypton and 180 MeV argon at greater depths are listed in Table 4.2.

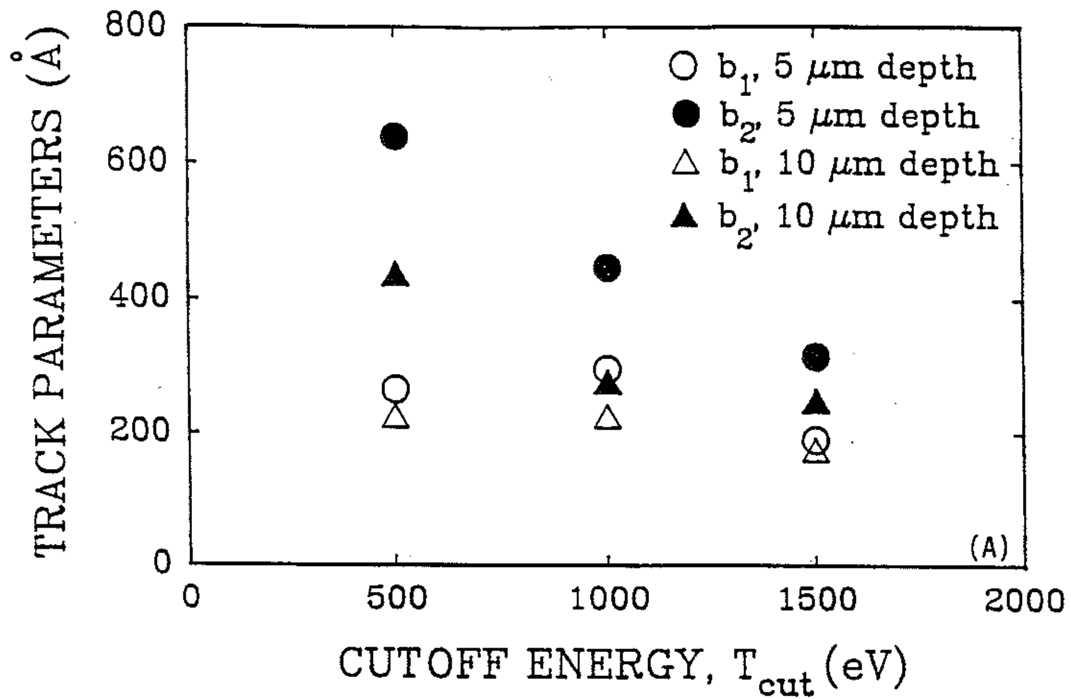

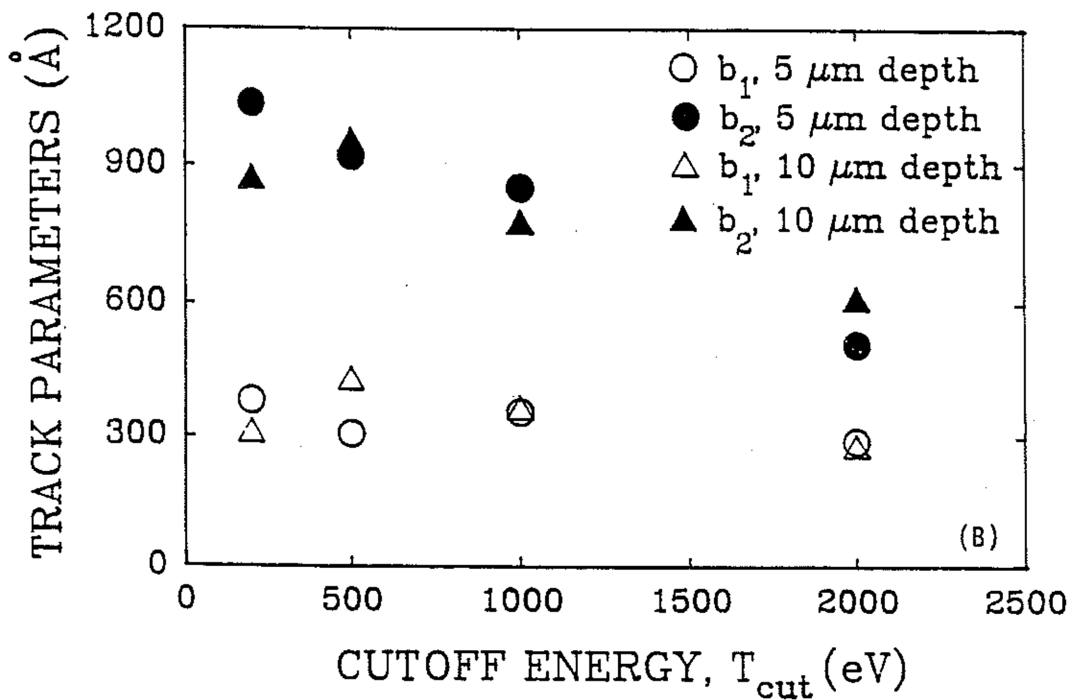

Figure 4.11: Track width parameters for different cutoff energies, at depths of 5 and 10 μm for (a) 270 MeV krypton and (b) 180 MeV argon ions.

Table 4.1. Analytical track parameters for different cutoff energies

	270 MeV Krypton					
	5 μm depth			10 μm depth		
T_c (eV)	b_1(Å)	b_2(Å)	ξ	b_1(Å)	b_2(Å)	ξ
500	265	639	0.0695	225	437	0.0874
1000	295	446	0.0622	225	276	0.104
1500	190	314	0.135	175	248	0.158
	180 MeV Argon					
200	380	1037	0.0879	310	872	0.0822
500	305	919	0.0732	430	956	0.0671
1000	355	850	0.0606	365	777	0.0643
2000	290	509	0.123	280	612	0.109

Table 4.2. Analytical track parameters at several depths

	270 MeV Krypton			180 MeV Argon		
depth (μm)	b_1(Å)	b_2(Å)	ξ	b_1(Å)	b_2(Å)	ξ
5	246	483	0.0462	384	893	0.0342
10	262	359	0.0345	325	909	0.0622
15	146	205	0.0443	268	741	0.0596
20	128	149	0.0140	232	583	0.0661
25	64	77	0.0074	200	404	0.0644
30	--	--	--	115	222	0.0913

4.5 Conclusions

Results indicate an exponential charge generation profile extending hundreds of nanometers from the ion path. Such a profile has been postulated for radiolysis in liquids [4.30], but not for charge tracks in semiconductors. Our results show the radial distribution of charge in the track is neither constant nor Gaussian as used in simulations, but agrees well with an exponential decay typical of high-energy SE penetration. Without consideration of these SEs, the large track sizes and long exponential profiles would not be created.

The radial distance over which the excess charge carrier concentrations remain above background dopant levels (typically 10^{16} cm^{-3}) is important for analysis of transient behavior. This distance was found to exceed 0.25 μm for 270 MeV krypton, 0.33 μm for 180 MeV argon, and 0.5 μm for 1 GeV iron. These values are greater than the previously mentioned assumptions for track width [4.31,4.32]. Although tracks of 1 μm radius have been postulated due to diffusion processes, the time frame for this is believed to be on the order of 500 ps [4.32]. Our simulation has found average SE slowing-down times on the order of 10^{-14} s, allowing for creation of larger initial tracks than has previously been thought.

Different results for the radial extent of the tracks of cosmic iron and those arising from cyclotron simulations also raise issues relating to the accuracy of cyclotron simulation of cosmic damage. Charge tracks generated by high-energy ions such as argon and krypton

are in general narrower than typical cosmic tracks. In addition, the cyclotron particle track profiles are attenuated faster and are less uniform than the cosmic particles. For typical device dimensions these differences may make accurate quantitative evaluations difficult for cyclotron simulation of cosmic phenomena.

Parameters have been evaluated to provide analytical expressions for the charge-density profiles along heavy ion tracks. These expressions provide much more detail than previous assumptions and will be useful as initial conditions for future modeling of transient charge transport. As an example, charge track profiles obtained from TRIPOS-E have been coupled with a PISCES code device analysis of the probability of double-bit upsets in NMOS SRAMs [4.33].

4.6 References

[4.1] H. J. Fitting and J. Reinhardt, Phys. Status solidi a, 88 (1985) 245.

[4.2] P. Chou and N. M. Ghoniem, J. Nucl. Mater., 117 (1983) 55.

[4.3] P. S. Chou and N. M. Ghoniem, Nucl. Instrum. Methods Phys. Res., B28 (1987) 175.

[4.4] R. C. Martin and N. M. Ghoniem, Phys. Status solidi a, 104 (1987) 743.

[4.5] R. C. Martin and N. M. Ghoniem, IEEE Trans. Nucl. Sci., NS-34 (1987) 1305.

[4.6] A. F. Akkerman and G. Ya. Chernov, Phys. Status solidi b, 101 (1980) 109.

[4.7] B. P. Nigam, M. K. Sundaresan, and T.-Y. Wu, Phys. Rev., 115 (1959) 491.

[4.8] G. Wentzel, Z. Phys., 40 (1927) 590.

[4.9] E. E. Anderson, Modern Physics and Quantum Mechanics, W. B. Saunders, Philadelphia 1971 (ch. 11).

[4.10] W. Jones and N. H. March, Theoretical Solid State Physics, Vol. 1, Wiley-Interscience, London 1973 (pp. 60-67).

[4.11] J. P. Ganachaud and M. Cailler, Surf. Sci., 83 (1979) 498.

[4.12] L. Smrčka, Czech. J. Phys., B20 (1970) 291.

[4.13] A. F. Akkerman and A. L. Gibrekhterman, Nucl. Instrum. Methods Phys. Res., B6 (1985) 496.

[4.14] A. E. S. Green, D. L. Sellin, and A. S. Zachor, Phys. Rev., 184 (1969) 1.

[4.15] S. Ichimura, M. Aratama, and R. Shimizu, J. Appl. Phys., 51 (1980) 2853.

[4.16] M. Gryzinski, Phys. Rev., 138 (1965) 336.

[4.17] S. Ichimura and R. Shimizu, Surf. Sci., 112 (1981) 386.

[4.18] R. A. Ferrell, Phys. Rev., 101 (1956) 554.

[4.19] R. H. Ritchie, Phys. Rev., 114 (1959) 644.

[4.20] R. Shimuzu, T. Ikuta, and K. Murata, J. Appl. Phys., 43 (1972) 4233.

[4.21] P. Duncumb and C. Da Casa, Conference on Electron Probe Microanalysis, Institute of Physics and the Physical Society, London 1967.

[4.22] R. C. Martin and N. M. Ghoniem, "Coupled Ion-Electron

Transport in Semiconductors," University of California Los Angeles Report No. UCLA-ENG-8708/PPG-1024 (March 1987).

[4.23] A. F. Akkerman and G. Ya. Chernov, Phys. Status solidi b, 89 (1978) 329.

[4.24] H. R. Philipp, as reported in Reference [4.1].

[4.25] J. C. Ashley and C. J. Tung, Surf. Interface Anal., 4 (1982) 52.

[4.26] A. Ya. Vyatskin and V. V. Trunev, Radiotekh. Elektron., 12 (1967) 1636.

[4.27] C. J. Tung, J. C. Ashley, V. E. Anderson, and R. H. Ritchie, "Inverse Mean Free Path, Stopping Power, CSDA Range, and Straggling in Silicon and Silicon Dioxide for Electrons of Energy ≤ 10 keV," U.S. Air Force Report RADC-TR-76-125, April 1976.

[4.28] J. P. Kreskovsky and H. L. Grubin, J. Comput. Phys., 68 (1987) 420.

[4.29] A. L. Smirl, in: Cohesive Properties of Semiconductors under Laser Irradiation, ed. L. D. Laude, Martinus Nijhoff Publishers, The Hague, 1983 (p. 348).

[4.30] G. C. Abell and K. Funabashi, J. Chem. Phys., 58 (1973) 1079.

[4.31] H. L. Grubin, J. P. Kreskovsky, and B. C. Weinberg, IEEE Trans. Nucl. Sci., NS-31 (1984) 1161.

[4.32] G. C. Messenger, IEEE Trans. Nucl. Sci., NS-29 (1982) 2024.

[4.33] Y. Song, K. N. Vu, J. S. Cable, A. A. Witteles, W. A. Kolasinski, R. Koga, J. H. Elder, J. V. Osborn, R. C. Martin, and N. M. Ghoniem, IEEE Trans. Nucl. Sci., NS-35 (1988) 1673.

Chapter 5

TRANSPORT OF ELECTRON-HOLE PAIRS

5.1 Introduction to Semiconductor Device Modeling

Semiconductor device simulation is a well-studied field, and a number of comprehensive references are available as background (e.g., references [5.1-5.4]. The differential equations governing semiconductor device behavior are Poisson's equation and the electron and hole continuity equations:

$$\vec{\nabla}\cdot\epsilon\vec{\nabla}\phi = -q(p - n + N_d^+ - N_a^-) \quad , \tag{5.1}$$

$$\frac{\partial n}{\partial t} = \frac{1}{q}\,\vec{\nabla}\cdot\vec{J}_n + (G - R) \quad , \tag{5.2}$$

$$\frac{\partial p}{\partial t} = -\frac{1}{q}\,\vec{\nabla}\cdot\vec{J}_p + (G - R) \quad , \tag{5.3}$$

plus the related current density equations:

$$\vec{J}_n = qn\mu_n\vec{E} + qD_n\vec{\nabla}n \quad , \tag{5.4}$$

$$\vec{J}_p = qp\mu_p\vec{E} - qD_p\vec{\nabla}p \quad , \tag{5.5}$$

in which ϵ is the material permittivity, ϕ the potential, n and p the electron and hole densities, N_d^+ and N_a^- the ionized donor and acceptor densities, q the electronic charge, $\vec{J}_n$ and $\vec{J}_p$ the electron and hole current densities, (G − R) the net generation/recombination rate, μ the mobility, D the diffusivity, and $\vec{E}$ the electric field. Coupling

between these equations typically requires either the Newton-Raphson iteration scheme for simultaneous solution of ϕ, n, and p, or an iterative technique in which Poisson's equation and the continuity equations are alternatively solved until the desired accuracy is obtained for each time step.

When the governing equations are strongly coupled (e.g., in transient simulations), the Newton-Raphson method is typically favored because of its quadratic rate of convergence, although at a cost of large matrix inversions. With M the number of computational nodes, the governing matrix is nonsymmetric of size 3M x 3M, thus requiring an order of magnitude more storage than a simple solution of the potential. Alternatively, an iterative solution can be employed in which Poisson's equation is solved assuming known quasi-Fermi levels (using an M x M symmetric matrix), these results used to solve the continuity equations (also M x M matrices), and the process repeated for each time step until the desired accuracy is obtained. This approach requires less computer memory, but the slow rate of convergence becomes a problem when the governing equations are strongly coupled [5.3].

5.2 Introduction to the Hybrid Finite Element/Particle Simulation Method

Particle simulation is a technique originally developed for plasma physics simulations, with one "superparticle" representing many individual particles and transported as if it were an individual

particle [5.5]. Application of particle simulation (PS) methods to semiconductor devices was reported by Hockney, Warriner and Reiser in 1974 [5.6]. Their approach was an extension of previous simulations of plasmas, in which the entire collection of charged particles within the plasma is represented by a computationally reasonable number of superparticles, and these superparticles transported over each time step using a method appropriate to the material medium and the device conditions. Use of PS techniques is attractive because of the convenience with which Monte Carlo transport methods can be implemented when appropriate.

The use of particle methods to represent the current continuity equations allows decoupling of these equations from Poisson's equation, permitting consecutive evaluation of the particle-pushing and potential solution steps at each time step. This decoupling permits significant reduction in matrix solution and storage requirements, with only the solution to Poisson's equation requiring matrix evaluations. In addition, PS transport of the superparticles makes the non-equilibrium transport problem more amenable to accurate treatment than do the traditional current continuity equations. This approach allows accurate treatment of transient device conditions if the time step and mesh sizes used are appropriately determined for convergence, and the mobility accurately approximates the scattering mechanisms involved.

Our approach merges these PS techniques with a finite element (FE) solution of Poisson's equation. To avoid discontinuities of electric field across interelement boundaries, we have used quadratic

interpolation of potential and density rather than the linear interpolation typically used in FE device analyses. To facilitate three-dimensional (3-D) analyses of charge collection from ion tracks, we have taken advantage of the axisymmetric track geometry by using an axisymmetric FE formulation for the solution of Poisson's equation. The axisymmetric form provides realistic 3-dimensional results with reasonable (2-D) demands on computer resources.

We chose the FE method for solving Poisson's equation for several reasons. The FE method has convenient similarities with PS methods, such as the use of the same shape functions for interpolation of potential from the mesh nodes across the triangular elements as are used in the particle-to-mesh charge weighting and mesh-to-particle force interpolations required by particle methods. Evaluation of the local shape functions at the particle's position also provides a convenient means of locating the particle within specific elements after the particle-pushing step. FE meshes also provide more flexibility for irregularly-shaped device geometries and nonuniform meshes.

Although linear interpolation of potential across a triangular element is much simpler than quadratic interpolation (i.e., requiring three nodes per element vs six), the resulting discontinuities in the force on particles crossing interelement boundaries generates increased computational noise in the system. To avoid this, we use quadratic interpolation to maintain continuity of force across element boundaries. Although more complicated, such a formulation

permits larger element sizes for similar accuracy compared with the linear interpolation.

After calculation of the nodal potentials, the particles are advanced to new positions. One of two approaches can be followed for particle motion, depending on the transport regime (i.e., linear or nonlinear, as determined by the local field strength and carrier energy). In the linear regime, the static-mobility diffusion approximation is convenient; i.e., particle motion is composed of a drift component induced by the local field and a random component resulting from scattering. In the nonlinear regime, a full MC approach can randomly select scattering mechanisms and recompute the wave vector after each scattering event. We use the simpler drift-diffusion model of carrier transport as a good approximation for carrier transport in silicon, as hot electron effects are much less significant in silicon as compared with, e.g., gallium arsenide. After each time step, the potential is recalculated. The sequence of calculations progresses from TRIPOS (ion track) to TRIPOS-E (high energy e-h pair spatial and energy distribution) to FE/PS (non-equilibrium transport).

5.3 The Finite Element Solution to Poisson's Equation

5.3.1 The Finite Element Formulation

FE methods have been used extensively for structural mechanics, and several good references are available [5.7,5.8,5.9]. The use of

FE methods for device simulation has become well established after its introduction by Hachtel et al. in 1974 [5.10] and popularization by Barnes and Lomax [5.11,5.12]. More recently entire device modeling workshops have been devoted to this method [5.13].

Although the use of FE codes for semiconductor device simulation is well established, only linear interpolation of potential across the elements has been reported. Higher-order interpolation, although more accurate, has not been pursued due to greater complexity in formulation and coding. Although linear interpolation permits continuous variation of potential across interelement boundaries, the resulting electric field is constant across an element and discontinuous across the boundaries. With quadratic interpolation of potential, the electric field varies linearly across elements and maintains continuity across the boundaries, allowing use of a coarser grid, reducing computational overhead, and reducing computational noise which can arise from the discontinuous electric fields.

The computational demands of a three-dimensional simulation of charge collection from an ion track are prohibitive. Most simulations have used 2-D Cartesian geometries. An ion path which perpendicularly intersects the center of a p-n junction is amenable to a 3-D simulation in axisymmetric geometry (r-z coordinates). By superimposing triangular elements onto a 2-D slice of the device, each element represents a 3-D triangular ring around the axis of symmetry of the ion track. We use triangular elements rather than rectangular elements because they more easily approximate irregular boundary regions and interfaces.

Although axisymmetric FE codes for the solution of Poisson's equation are common [5.8], those using higher-order interpolation are uncommon. A higher-order FE code for the solution of axisymmetric field problems has been reported, applicable for Laplace's, Poisson's, and Helmholtz's equations [5.14,5.15]. This code can provide up to fourth order polynomial interpolation, but is reported to be limited to problems with matrix size of approximately 100 by 100. Realistic semiconductor device simulation typically requires the larger matrices which result from thousands of grid points. Our study also requires a FE code amenable to direct coupling with a PS scheme. These two factors encourage the development of an original axisymmetric FE code using quadratic interpolation, rather than attempting to modify this pre-existing code.

Our FE formulation is described in detail in reference [5.16]. The FE method approximates the exact solution ϕ to the Poisson equation by an interpolating function defined over each element:

$$\phi \approx N_1\Phi_1 + \ldots + N_i\Phi_i \quad , \tag{5.6}$$

with Φ_i the value of the potential at each node i of the element and N_i the nodal shape functions of magnitude 1 at node i and 0 at all other nodes [5.8]. The shape functions are defined such that at any point within the triangle:

$$\Sigma N_i = 1 \quad . \tag{5.7}$$

Linear shape functions require only 3 nodes per triangle, but we use 6 nodes per triangle for our quadratic formulation.

For higher-order interpolating functions (i.e. non-linear shape functions), the concepts of local and global shape functions must be clarified. For example, consider a simple triangular element with a linear interpolating function defined with respect to the three corner nodes, and consider a local coordinate system defined with respect to the isolated triangle rather than in terms of r and z coordinates. The local shape function for node 1 can be defined relative to a point P inside the triangle as:

$$L_1 = A_1/A \quad , \tag{5.8}$$

where A is the area inside the triangle and A_1 is the region indicated in Figure 5.1. These shape functions L_i can be related to the global coordinates r and z by:

$$L_i = (a_i + b_i r + c_i z)/2A \quad , \tag{5.9}$$

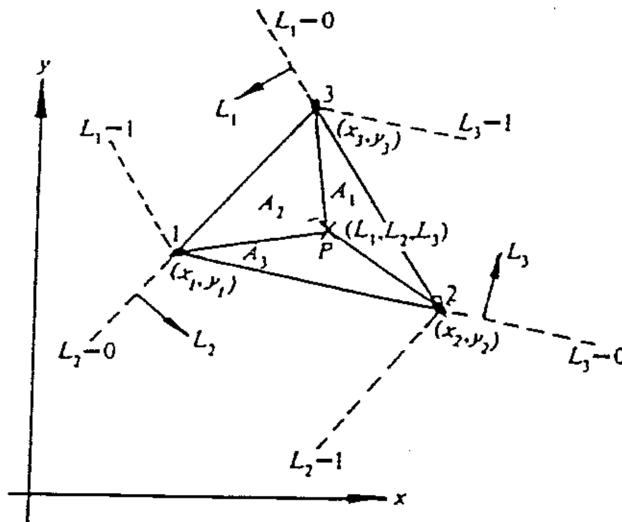

Figure 5.1: Area coordinates for linear triangular elements [5.7].

with the coefficients a_i, b_i, and c_i algebraically defined in terms of the r- and z-coordinates of the corner nodes [5.8].

For a linear interpolating polynomial, the local shape functions L_i and the global shape functions N_i are identical. For a quadratic interpolating function, the global shape functions N_i for the six nodes are quadratic in the local shape functions L_i, i.e., of order L_i^2. For the triangle shown in Figure 5.2, L_1, L_2, and L_3 are defined at the corner nodes 1, 2, and 3, and vary linearly across the triangle, while N_i vary quadratically as in Figure 5.3.

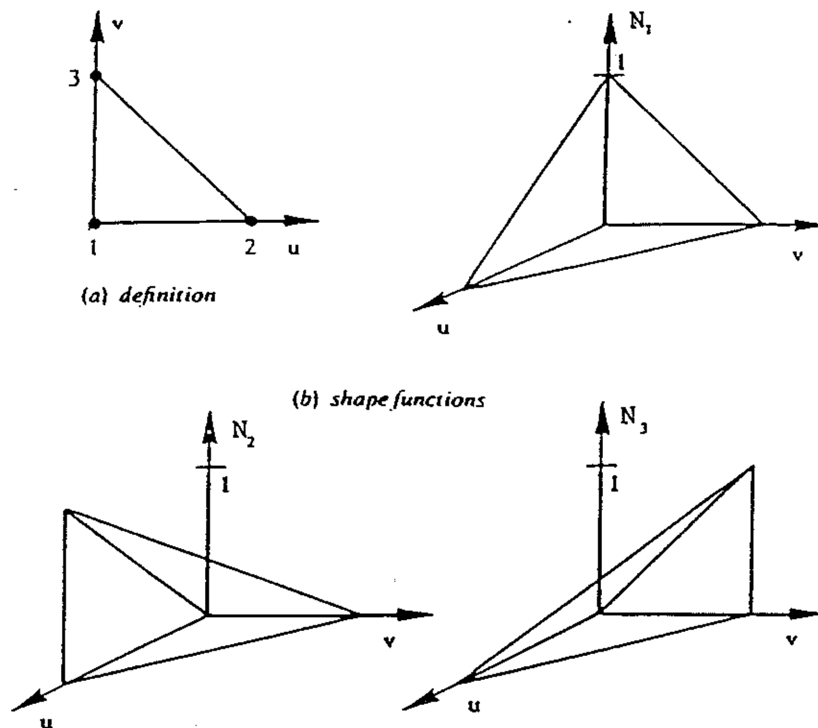

Figure 5.2: Linear triangular elements in finite element analysis, showing (a) the element and its nodes, and (b) the linear shape function for each node [5.17].

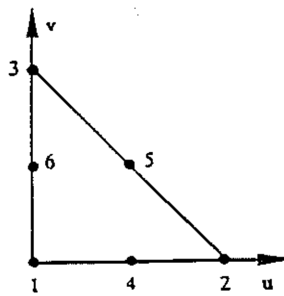

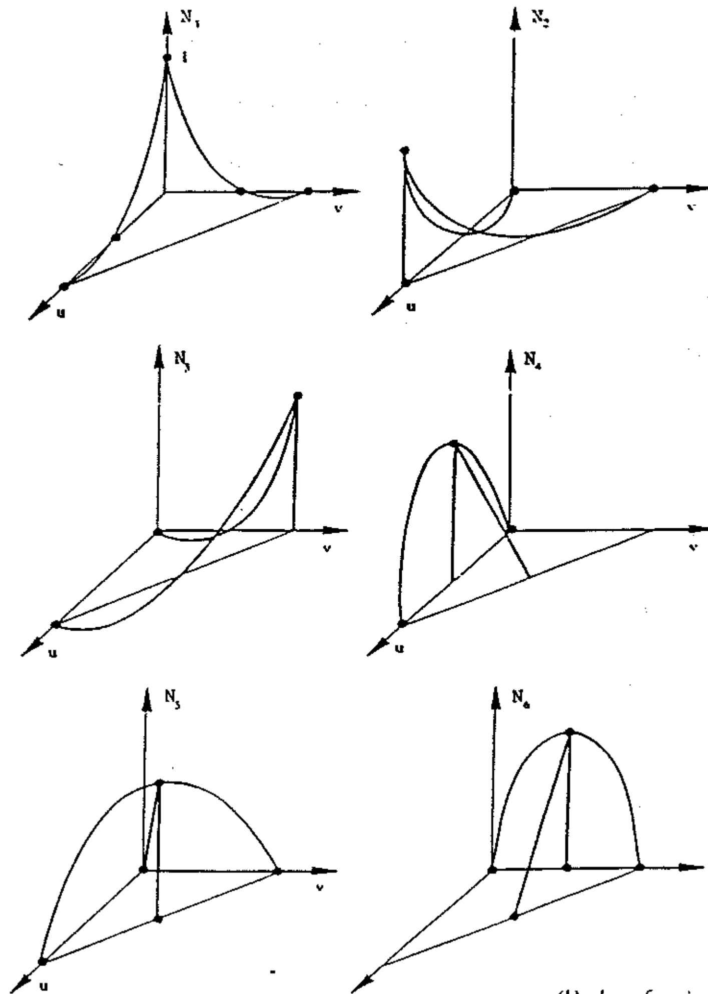

Figure 5.3: Quadratic triangular elements in finite element analysis, showing (a) the element and its nodes, and (b) the quadratic shape function for each node [5.17].

The Poisson equation for axisymmetric geometry can be represented by:

$$\text{div } \vec{D} = \rho(r,z) \quad , \tag{5.10}$$

where $\vec{D} = \epsilon\vec{E} = \epsilon(-\text{ grad } \phi) \quad .$ (5.11)

and $\rho(r,z) = -q(p - n + N_d^+ - N_a^-) \quad .$ (5.12)

Typical FE formulations of Poisson's equation use either the variational or Galerkin approaches (see e.g., references [5.11] and [5.18]). In the first approach, the governing equation is cast in the form of a variational principle, while the second begins by casting the governing equation in terms of a residual. Governing equations were derived for both approaches, but the Galerkin method was found to give simpler governing equations (i.e., with lower powers of the local shape functions) and was thus used in our formulation [5.16].

In the Galerkin formulation, we define the residual as:

$$R = \text{div } \vec{D} - \rho(r,z) \quad . \tag{5.13}$$

The Galerkin approach weights the residual by some shape function N_j, and that product is integrated over the region to be modeled. In axisymmetric cylindrical coordinates the governing equation becomes:

$$\int_V N_j \left[\frac{1}{r}\frac{\partial}{\partial r}(r\frac{\partial\phi}{\partial r}) + \frac{\partial^2\phi}{\partial z^2}\right] dV = -\frac{1}{\epsilon}\int_V N_j \rho(r,z)\, dV \ , \tag{5.14}$$

in which we assume an isotropic dielectric constant. The volume element dV equals $2\pi r$ dr dz. The region is broken up into a collection of triangular elements.

To evaluate the spatial derivatives in equation (5.14), we note that N_i is a function of r and z, while Φ_i has a specified value only at the node i and is zero elsewhere. The Φ_i thus behave as constants, and the spatial derivatives only act on the shape functions. With the integral now evaluated over the region of a single element, equation (5.14) takes the form:

$$\sum_{i=1}^{6} \left[\int_{V^e} \left[N_j \left(\frac{1}{r} \frac{\partial}{\partial r} \left(r \frac{\partial N_i}{\partial r} \right) + \frac{\partial^2 N_i}{\partial z^2} \right) \right] dV \right] \Phi_i = -\frac{1}{\epsilon} \int_{V^e} N_j \, \rho(r,z) \, dV. \quad (5.15)$$

With six nodal variables Φ_i per triangle, both i and j must take on values from 1 to 6. This generates the matrix equation for the element:

$$[k^e] \{\Phi\} = \{f^e\} \quad , \qquad (5.16)$$

with $[k^e]$ a 6 x 6 symmetric matrix and $\{\Phi\}$ and $\{f^e\}$ 6-element column matrices. The matrix $[k^e]$ is traditionally called a stiffness matrix, and $\{f^e\}$ the loading or force vector.

The elements of the stiffness matrix are given by the integral term on the left-hand side of equation (5.15). This integral term corresponds to $N_j \nabla^2 N_i$ in cylindrical coordinates, and the first form of Green's theorem can be used to obtain:

$$k_{ij} = \int_{V^e} N_j \nabla^2 N_i \, dV = -\int_{V^e} \vec{\nabla} N_j \cdot \vec{\nabla} N_i \, dV + \int_{S^e} N_j \vec{\nabla} N_i \cdot \vec{n} \, dS \ , \quad (5.17)$$

with $\vec{n}$ the unit vector normal to the surface enclosing the region V^e. We can show that the surface term equals zero for common semiconductor device modeling boundary conditions (i.e., Dirichlet boundary conditions with Ohmic contacts, or Neumann boundary conditions at planes of symmetry or typical semiconductor/insulator interfaces) [5.16]. Using this result, we convert equation (5.17) into the form for cylindrical coordinates:

$$k_{ij} = \int_{V^e} \left[\frac{\partial N_j}{\partial r} \frac{\partial N_i}{\partial r} + \frac{\partial N_j}{\partial z} \frac{\partial N_i}{\partial z} \right] r \, dr \, dz \quad , \qquad (5.18)$$

in which the minus sign cancels with that in equation (5.15). The term for r can be expressed in the form of a linear interpolation with respect to only the three corner nodes:

$$r = r_1 L_1 + r_2 L_2 + r_3 L_3 \quad . \qquad (5.19)$$

For the element of the force vector, $\rho(r,z)$ must be interpolated from the same nodes at which the potential is evaluated, analogous to ϕ in equation (5.6).

The integrals for k_{ij} and f_i are too involved to evaluate analytically, so numerical methods of integral evaluation are employed. We use the technique of Gaussian quadrature [5.8].

Numerical integration is simplified by converting all terms in equation (5.18) to functions of the local shape functions L_1, L_2, and L_3. Gaussian quadrature is then be applied to local L-space.

Briefly, we convert the spatial derivatives of equation (5.18) into the product of the derivatives with respect to L_i and the inverse of the Jacobian [J]. The products of the spatial derivatives in equation (5.18) are evaluated in terms of L_1, L_2, and L_3, and multiplied by r [equation (5.19)] and the determinant of [J] to obtain a function $g(L_1, L_2, L_3)$ amenable to Gaussian quadrature:

$$k_{ij} = \int_0^1 \int_0^{1-L_2} f(L_1, L_2, L_3) \; |\det[J]| \; dL_1 \; dL_2$$
$$= \sum_{i=1}^{\ell} W_i \; g(L_1, L_2, L_3). \tag{5.20}$$

The function g is evaluated at ℓ specific points with tabulated values of L_i, to give an exact solution for the interpolation of g across the triangle. The value of g is multiplied by tabulated weights, and the process repeated over the ℓ points and summed to provide a numerical value for k_{ij}.

The elements of the loading vector can be similarly evaluated using Gaussian quadrature. As these values are evaluated element-by-element, they are combined into an overall matrix equation. After the values of k_{ij} and f_i have been evaluated for each element, these elemental matrices must be combined into an overall matrix. For this, we let the values of i and j in k_{ij} and f_i take on the number of the node as it is labeled in the overall system, i.e. some number between 1 and M, where M is the total number of nodes. We then construct the matrix equation:

$$[K] \; \{\Phi\} = \{F\} \quad , \tag{5.21}$$

with [K] an M x M symmetric matrix and $\{\Phi\}$ and $\{F\}$ column vectors of length M. Each element K_{ij} of [K] contains the contributions k_{ij} from any triangle which contains the nodes i and j; the elements F_i are constructed in a similar fashion by summing all terms f_i from those triangles containing the node i. Prior to solution for $\{\Phi\}$, any Φ_i specified by Dirichlet boundary conditions must be imposed on the system of equation (5.21). That is, any Φ_i specified on the boundary are no longer unknowns and must be imposed on the system. The matrix is modified by standard approaches [5.8], but remains symmetric. With all elements of [K] and $\{F\}$ evaluated, $\{\Phi\}$ can be determined using whatever matrix solution technique is most efficient.

5.3.2 Solution Methods for Systems of Linear Equations

Several good references are available on solution techniques for systems of algebraic equations (e.g., reference [5.19]). Applicability of the various techniques was studied in detail in reference [5.16]. For rectangular devices with simple boundary conditions, the rapid elliptic solvers such as FFT are very useful. Development of fast Fourier transform (FFT) solutions to Poisson's equation have received increased attention over the past decade for their speed and convenience. However, these FFT routines have traditionally been applied to finite difference approximations rather than our FE approach.

Other techniques fall either into the category of mesh-relaxation methods (essentially iterative methods) and matrix methods which act on the matrix representing the linear equations. The mesh-relaxation techniques include the Gauss-Seidel, successive overrelaxation, successive line overrelaxation, and alternating direction implicit schemes. The matrix methods include the Thomas tridiagonal algorithm (for 1-D), sparse matrix methods (e.g., banded Gaussian elimination), the conjugate gradient algorithm, Stone's strongly implicit procedure, and incomplete Choleski-conjugate gradient method.

For our problem, the Choleski LU decomposition of the banded symmetric matrix [K] is efficiently used to solve for Φ_i. We use IMSL routines LEQ1PB for initial inversion of the K-matrix and LUELPB for subsequent solutions of Φ_i at each time step [5.20]. Although this method may be more time consuming than some iterative matrix solution methods, no convergence problems are expected. To minimize matrix storage requirements and improve efficiency, the nodes are numbered such that the bandwidth is kept as small as possible.

Although FFT solutions of Poisson's equation are very rapid, the requirement of regularly spaced meshes and the difficulty of treating irregular device geometries has tended to discourage widespread use of the FFT method. The presence of internal electrodes also requires additional computations involving capacitance matrix methods [5.19]. Because FFT methods cannot be formulated in axisymmetric geometry, a three-dimensional FFT formulation would be required to simulate our ion track problem, and a 3-D capacitance matrix routine would be

required for the internal electrodes typical of semiconductor devices. To our knowledge, only one formulation of a 3-D capacitance matrix routine has been reported [5.21]. Typical spacings of the computational mesh are smaller for FFT routines than those we have found practical for our FE Poisson solver, and extension to 3-D geometry would require significant matrix computations due to the large number of nodes required. Although Moglestue has recently reported the use of Hockney's FFT routines for 3-D simulations "to analyze semiconductor microcomponents of any geometry", he apparently has not implemented a capacitance matrix routine which would allow the simulation of internal electrodes [5.22].

The advantages of using a coarser mesh in true axisymmetric geometry and the ability to do future simulations for any irregular geometry favored our use of FE methods rather than FFT. The easy availability of packaged linear equation solvers was felt to be preferable to the major software development required for developing and coupling a 3-D capacitance matrix routine to our PS routine. We have found that the computer time required by our linear equation solver in the FE formulation is not a major factor in the overall cost of running our code. Although an FFT formulation might reduce this cost, the other inherent disadvantages might not aid in the general applicability and future development of our numerical method to simulations of charge tracks and radiation effects in other media.

5.4 The Particle Simulation Method

5.4.1 Introduction

Application of particle simulation (PS) methods to semiconductor devices was reported by Hockney, Warriner and Reiser in 1974 [5.6]. Hockney et al. simulated the steady-state operation of GaAs and silicon FETs and diodes using 12,000 to 30,000 particles. This simulation was done by using either a full Monte Carlo transport scheme or the static-mobility diffusion approximation (SMDA) in which a particle's motion consists of a drift and a diffusive component. A time step of 5×10^{-14} s and a uniform mesh were employed; the uniform mesh permits use of fast Fourier transform (FFT) techniques to solve for the potential profile. Both the potential and force equations were solved by finite difference schemes. Hockney and Eastwood [5.19] reviewed this PS/FFT approach to device analysis in 1981.

In 1977 Warriner applied this PS model to simulate GaAs negative-resistance oscillators and FETs [5.23], with cell sizes of 0.1 and 0.02 μm respectively. Also in 1977 Rees et al. applied this model to simulate a low-temperature FET [5.24]. In 1979 Moglestue and Beard used the same approach to simulate GaAs FETs [5.25]; they simulated 10,000 particles with a time step of 5×10^{-14} s for recalculation of the field. In 1982 Pone et al. [5.26] did another analysis of GaAs FETs using particle and SMDA methods; their numerical approach is similar, although more discussion is presented

on the relation of carrier relaxation times to the SMDA approach and on the limitations of particle noise (it being concluded that present computer memories limit modeling to devices with doping less than 10^{17} cm^{-3}). More recent reports of particle models applied to GaAs FETs [5.27] and MOSFETs [5.28] rely on Hockney et al.'s original approach [5.6]. Analysis of millimeter-wave IMPATT devices by Lippens et al. [5.29] again uses the SMDA and PS approaches of reference [5.6], with 10,000 particles, a time step of 5×10^{-14} s, and a cell size of 2×10^{-6} cm.

Although PS techniques in device analysis have been refined since their introduction, they do not significantly differ from the original effort of Hockney et al. [5.6]. Many of the above-mentioned applications rely on the FFT solutions of Poisson's equation developed by Hockney et al. Although FFT analysis permits a major speedup in potential calculations, complex device geometries are more difficult to simulate and internal electrodes require additional computations involving capacitance matrix methods [5.19]. The requirement of regularly spaced meshes and the difficulty of treating irregular device geometries has tended to discourage widespread use of the FFT method. Apparently PS methods have not been extended for use with numerical techniques other than finite difference schemes, and only majority carrier transport has been simulated.

5.4.2 Formulation of the Method

Particle-simulation methods typically use a rectangular grid. The nearest-grid-point (NGP) and cloud-in-cell (CIC) methods are commonly used to allocate charge to nearby grid points for potential field calculations. The NGP scheme assigns the entire charge of a particle to the nearest grid point, but the amount of inherent computational noise can be significant as the moving particle's charge discontinuously jumps from one grid point to the next. Instead, CIC allocates the charge of the particle to several nearby grid points, in effect extending the particle from a point charge to a cloud of charge [5.30] (Figure 5.4), with the amount of charge allocated to each neighboring grid point equivalent to the fractional area of the charge cloud within the cell surrounding that grid point.

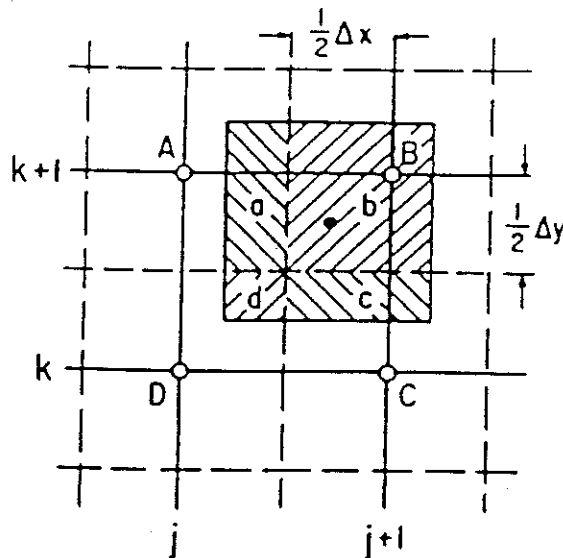

Figure 5.4: Cloud-in-cell charge assignment for linear two-dimensional weighting. Areas are assigned to grid points; i.e., area a to grid point A, b to B, etc., with the particle center located as indicated [5.30].

With an irregularly shaped triangular mesh, a scheme must be devised to assign the charge from the particle position to the surrounding nodes. For this, we can use the same quadratic shape functions that we have previously used to interpolate the nodal potentials over the element. For a point P inside the triangle, the local shape functions with respect to that point can be defined identically with equation (5.8). The charge Q_i assigned to node i from a particle at point P can then be handled analogously to the interpolation of the potentials at each node over the triangle [equation (5.6)]. For example, the relationship between Q_i and Q_P must take on the form:

$$Q_i = N_i \, Q_P \quad . \tag{5.22}$$

Here, we are now interpolating from point P to node i. If we calculate the values of L_1, L_2, and L_3 from the position of P within the triangle, we can calculate the global shape functions N_i and directly obtain the values of Q_i for the six surrounding nodes, for use in the subsequent solution of Poisson's equation.

With the charge allocated to the nodes, Poisson's equation is solved for the nodal potentials using the FE Poisson solver. In interpolating the nodal potentials, Φ_i, back to the particle positions, the electric field at a point is given by:

$$\vec{E} = -\nabla\phi = -\left[\sum_{i=1}^{6} \Phi_i \frac{\partial N_i}{\partial r} \vec{r} + \sum_{i=1}^{6} \Phi_i \frac{\partial N_i}{\partial z} \vec{z} \right] \quad . \tag{5.23}$$

We know the spatial derivatives for each value of i in terms of the local shape functions L_i, and have previously calculated the values of L_1, L_2, and L_3 for each particle's position. The global shape functions N_i are then calculated for (r_p, z_p), and all N_i and L_i are stored for subsequent calculations. We can then calculate the values of the spatial derivatives for each surrounding node, multiply each by the potential at that point, and sum over all six nodes to obtain the components of the electric field in the r- and z-directions at the particle's position. This value, multiplied by the charge on an electron, gives the force on the particle due to the electric field.

5.4.3 Particle Transport

Hockney et al. [5.6] suggest one of two methods to advance the position of the particle over a time step. The simpler SMDA method (drift-diffusion model) considers each increment in particle position to be composed of two components, one due to the electric-field-induced drift of electrons (of magnitude $\mu E \Delta t$ with Δt the time step) and the other due to a random diffusional motion [of magnitude $(2D\Delta t)^{1/2}$ according to Hockney, although $(4D\Delta t)^{1/2}$ seems more reasonable]. This approach assumes the carrier velocities are instantaneously related to the field by a field-dependent mobility, as in conventional device simulation codes such as PISCES [5.31] and MINIMOS [5.32].

The second method is a complete Monte Carlo (MC) treatment, where rates of scattering are evaluated for all relevant scattering

mechanisms. For situations involving hot-electron transport effects, inter-valley transitions, non-Maxwellian carrier distributions, or non-local field effects, the SMDA can be an inaccurate approximation. The MC approach better accounts for the physics of microscopic transport, and a recent modification of PISCES includes the MC method [5.33]. Expressions for the frequencies of phonon- and ionized-impurity-assisted intravalley and intervalley scattering in silicon for both electrons and holes are available [5.34,5.35,5.36]. Treatment of carrier-carrier scattering is not as developed because of the uncertainty in the distribution function; however, expressions useful for MC analysis have been obtained using assumptions [5.37]. This scattering mechanism is dominant within the e-h plasma. As reported by Hockney et al. [5.6] , a major disadvantage of the MC approach is the use of about ten times the computer time relative to the SMDA method.

The carrier energy and the local field strength determine whether the SMDA gives satifactory results or if a MC formulation is required. The secondary electrons created by the ion remain energetic within the time frame of the initial computational cycle. With high-density e-h plasma relaxation times on the order of 10^{-16} s (i.e., the characteristic e-h collision times [5.38]), their thermalization in the central dense region of the track is a reasonable assumption. The use of computational time steps on the order of 0.05 ps suggests the vast majority of the secondary electrons and core plasma electron-hole pairs will have thermalized by the beginning of the computational sample. The small fraction of

energetic secondary electrons remaining at the beginning of the computational cycle should not introduce significant error in the use of the SMDA for transport of the thermalized transient charge. We employ the SMDA by using appropriate values of μ and D as a function of carrier concentration. If future device applications require MC transport, our FE/PS formulation is flexible enough that a MC formulation could be readily introduced into the code. Simulations could conceivably employ both methods, with particles of different energies being transported by the method relevant to their energies, or by different methods in subsequent steps.

Data is available to implement the SMDA, including data for very high carrier densities within the ion track. Recently the transport data has been augmented by experiments of carrier generation using femtosecond laser pulses. Laser pulse measurements have provided values for ambipolar diffusion coefficients with carrier densities as high as 10^{21} cm^{-3} [5.39]. Dorkel and Leturcq [5.40] have estimated electron and hole mobilities in silicon under high-injection regimes, for pn-products as high as 10^{36} cm^{-6}; at 300 K the electron mobility drops from the typical 1430 cm^2/V-s to < 200 cm^2/V-s under high-injection conditions.

As we are initially emphasizing silicon device simulations, we have implemented the SMDA transport method for all particles as a good approximation. We evaluate the mobility using the calculation procedure proposed by Dorkel and Leturcq [5.40]. This procedure can accurately simulate mobilities for all but the largest track concentrations. The carrier mobility is calculated as:

$$\mu = \mu_L \left[\frac{1.025}{1 + (X/1.68)^{1.43}} - 0.025 \right] , \qquad (5.24)$$

with μ_L the lattice mobility, given by:

$$\mu_L = \mu_{L_o} \, (T/300)^{-a} , \qquad (5.25)$$

in which T is the temperature and μ_{L_o} and a are parameters dependent on the type of carrier and the temperature range. In equation (5.24) X is given by:

$$X = \left[\frac{6\mu_L(\mu_I + \mu_{ccs})}{\mu_I \mu_{ccs}} \right]^{1/2} , \qquad (5.26)$$

with μ_I the impurity mobility and μ_{ccs} the carrier-carrier scattering mobility, given by:

$$\mu_I = \frac{AT^{3/2}}{N_{dop}} \left[\ln\left(1 + \frac{BT^2}{N_{dop}}\right) - \frac{BT^2}{N_{dop} + BT^2} \right]^{-1} , \qquad (5.27)$$

$$\mu_{ccs} = \frac{2 \times 10^{17} \, T^{3/2}}{(np)^{1/2}} \{\ln\left[1 + 8.28 \times 10^8 \, T^2 \, (np)^{-1/3}\right]\}^{-1} . \qquad (5.28)$$

In equation (5.27), N_{dop} is the net local dopant concentration and A and B are carrier-dependent parameters. In equation (5.28), n and p are the electron and hole carrier concentrations. The above expressions are appropriate for weak electric-field conditions. Extension to situations involving strong electric fields uses an approach suggested by Caughey and Thomas [5.41]:

$$\mu = \frac{\mu_o}{[1 + (E/E_c)^b]^{1/b}} \quad , \tag{5.29}$$

in which E is the magnitude of the local electric field, E_c is a carrier-dependent constant, and μ_o is the result from equation (5.24). The constants used in equations (5.24) through (5.29) are given in Table 5.1. The diffusivities D_n and D_p are obtained from equation (5.29) using the Einstein relation. For densities above 10^{18} cm^{-3}, a mobility expression similar to reference [5.41] is used.

Minority carrier transport is handled simultaneously with the majority carriers. The np product is used as a measure of the relative carrier recombination or thermal generation during each time step, after nodal carrier densities are evaluated and before the

Table 5.1. Constants used in mobility calculations [5.40]

Constant	Electrons	Holes
T (K)	300	300
μ_{L_o} (cm^2 V^{-1} s^{-1})	1430	495
a	2.2	2.2
A (cm^{-1} V^{-1} s^{-1} $K^{-3/2}$)	4.61×10^{17}	1.0×10^{17}
B (cm^{-3} K^{-2})	1.52×10^{15}	6.25×10^{14}
E_c (V cm^{-1})	8000	19,500
b	2	1

solution of Poisson's equation. The net rate of carrier thermal generation and recombination is given by the standard expressions for Shockley-Read-Hall and Auger recombination [5.42]:

$$G - R = (n_i^2 - np) \{[\tau_n(p + n_i) + \tau_p(n + n_i)]^{-1} + c_n n + c_p p\} \quad , \qquad (5.30)$$

with the local carrier lifetimes given by:

$$\tau_n = 3.95 \times 10^{-5}/[1 + (N_{dop} / 7.1 \times 10^{15})] \text{ s} \quad , \qquad (5.31)$$

$$\tau_p = 3.52 \times 10^{-5}/[1 + (N_{dop} / 7.1 \times 10^{15})] \text{ s} \quad , \qquad (5.32)$$

with n_i the intrinsic carrier density and the Auger coefficients $c_n = 2.8 \times 10^{-31}$ cm^6/s and $c_p = 9.9 \times 10^{-32}$ cm^6/s.

Carrier recombination must be taken into account after each time step. Auger recombination quickly reduces peak e-h plasma densities, while Shockley-Read-Hall (SRH) recombination must be considered in lower concentration regimes. After the particle-to-node charge assignment step, and prior to the solution of Poisson's equation, the expressions for Auger and SRH recombination will be applied to the charge densities at each node and this charge reduced by the fraction of charge carriers undergoing recombination within the time step Δt.

The only boundary conditions used on the particles are those required by equilibrium conditions at the ohmic contacts. After each time step, the majority carrier density within the contact boundary elements is immediately equilibrated to match the doping density, and the minority carrier density is adjusted to satisfy the thermal equilibrium condition at the contact:

$$n_i^2 = np \quad . \tag{5.33}$$

The complete computational cycle is represented by the flow chart of Figure 5.5.

5.5 The Combined Finite Element/Particle Simulation Method

5.5.1 Computational Considerations

Not much has been written on the choice of grid spacing and time step as it applies to the finite element approach to device simulation. The criteria which are sometimes mentioned appear to frequently be derived from finite difference stability and accuracy criteria, or to be based on empirical computational experience. One such brief discussion of stability and convergence criteria has been given by Barnes and Lomax [5.12].

Mesh Size

In terms of the mesh spacing, two criteria are given for numerical stability: the Debye length and the cell Reynolds number. A mesh spacing on the order of the Debye length is frequently mentioned as a requirement for meaningful physical results [5.12], with the Debye length defined as:

$$L_D \simeq \left[\frac{2kT\epsilon}{q^2 N_{dop}}\right]^{1/2} \quad , \tag{5.33}$$

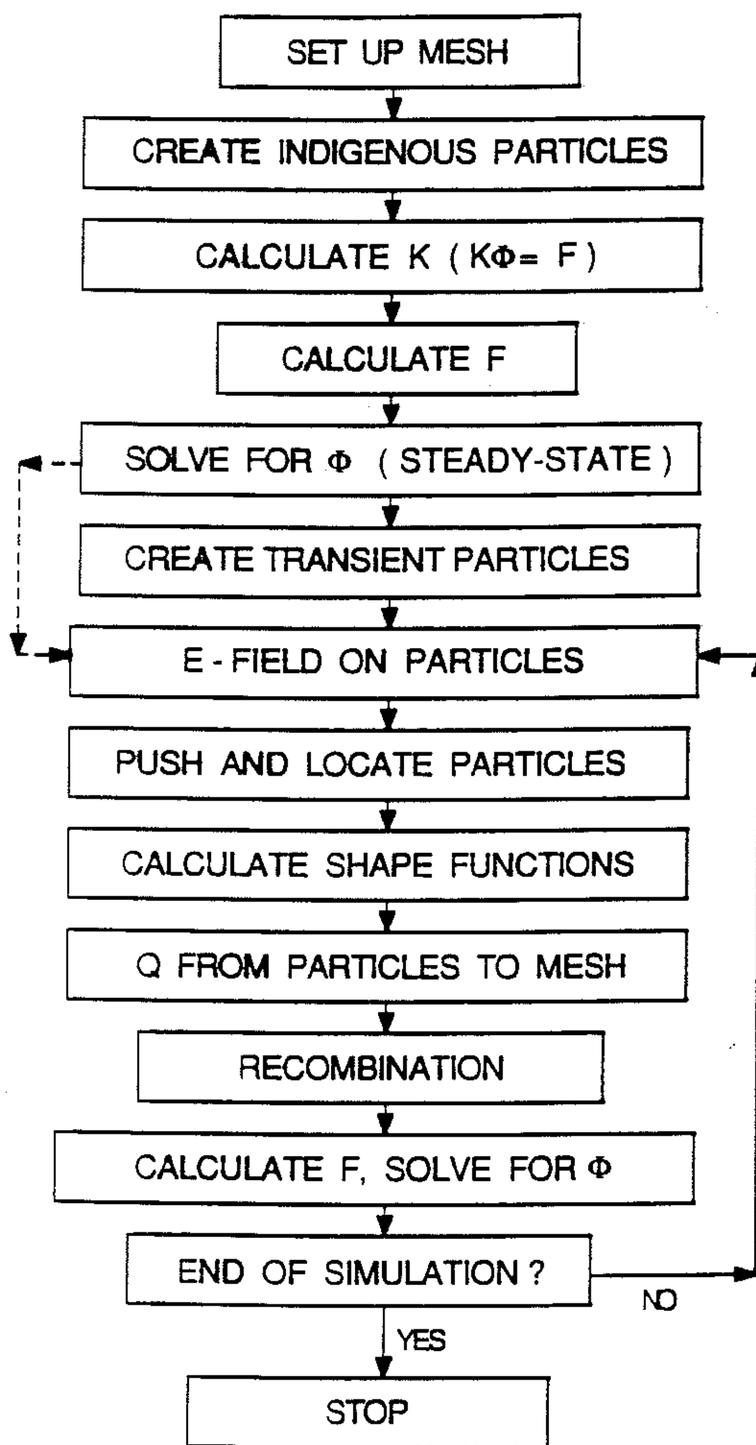

Figure 5.5: Flowchart for the finite element/particle simulation code.

with all terms defined as before. For example, a carrier concentration of 10^{16} cm^{-3} requires a grid spacing of about 0.04 μm while a concentration of 10^{18} cm^{-3} requires a spacing of about 0.004 μm. Such a criterion is computationally impossible for large doping concentrations. Some finite difference and finite element analyses have adhered to this criteria. For example, Riemanschneider and Wang [5.43] chose grid spacings of about half the Debye length for their FE simulation. However, other FE and FD analyses frequently employ grid sizes much larger than this criterion, as a matter of computational necessity. One detailed anaysis of the stability of FD analyses [5.44] concluded that the mesh size should be less than the Debye length when significant potential gradients exist over a Debye length. However, that criterion was violated in order to maintain feasible computational requirements while still obtaining meaningful physical results. This pragmatic approach seems reasonable for those cases where the Debye length is too small to be a practical requirement for grid spacings. This pragmatic approach is in the spirit of reference [5.29], which deliberately avoided simulation of heavily doped p^+ and n^+ contact regions; with dopant concentrations in excess of 10^{19} cm^{-3}, any internal field is rapidly forced to zero and thus such regions of high carrier concentration can be considered non-active regions in practice. Kreskovsky and Grubin in their ion track calculations recently used an average cell size of nearly 0.2 μm with no apparent stability problems [5.45].

Inhomogeneities of charge density and doping will not be felt beyond one Debye length. Less than one Debye length, charge and

potential oscillations will be apparent. Although these phenomena are meaningful for studies of plasma oscillations and properties on this spatial scale [5.19], this criterion does not appear to be critical for macroscopic semiconductor analysis. Because of this, we believe grid sizes less than a Debye length unnecessarily increase computational effort without contributing to the overall analysis.

The second criterion for grid spacing arises from finite difference approximations to the current continuity equations, and requires that the cell Reynolds number R_c must be small enough to avoid overshoot leading to negative densites [5.12], i.e.:

$$R_c \simeq \frac{vh}{D} \leq 2 \quad , \tag{5.34}$$

with v the carrier velocity, h the computational cell size, and D the carrier diffusivity. Based on this criteria, cell size for electrons should be in the range 0.064 to 0.75 μm (depending on their velocity), and that the cell size for holes is on the order of 0.025 μm. A major advantage of particle simulation methods is that negative densities cannot arise numerically [5.6]. Thus, we believe our finite element/particle simulation scheme relaxes this criterion relative to FD formulations.

In conclusion, we need fine grid over strong potential gradients so as not to lose the physics and detail of the problem at the most significant regions of carrier behavior. We also need fine grid over regions of heavy doping, as we have seen perturbations in the potential profile arise with doping levels approaching 10^{18} cm^{-3}.

From experience, we have found mesh spacings of 0.20 μm or more acceptable for low doping and low field conditions. Regions with strong potential gradients may be handled with mesh spacings of 0.10 to 0.15 μm, depending on doping conditions. For an n^+-contact with doping of 10^{18} cm^{-3}, we can largely suppress potential oscillations within the contact region with a mesh spacing on the order of 0.05 μm. These results suggest that our numerical method permits significant relaxation of the criteria accepted for finite difference mesh spacings.

Time Step

Two criteria are suggested for determining the appropriate time step, involving the dielectric relaxation time and the cell Courant number. The maximum time step is given as two to three times the dielectric relaxation time, or a spatial density oscillation may result from the time delay between solving Poisson's equation and the continuity equation [5.12]:

$$\tau \simeq \frac{\epsilon}{q \mu N_{dop}} \quad . \tag{5.35}$$

The dielectric relaxation time can be defined as a time constant which characterizes the exponential decay with time which any charge perturbation will exhibit. This criteria is relevant to analyzing non-equilibria situations. A charge imbalance sets up restoring forces, and an excessively long time step would not reflect the exponential decay of the force over that time. Thus carriers could

be transported further than would be physically accurate, leading to density and potential oscillations in subsequent time steps. From this it would be expected that accurate numerical analysis of non-equilibrium systems requires a time step on the order of the dielectric relaxation time. However, it may be feasible to relax this criteria as the system moves toward equilibrium, as Grubin and Kreskovsky concluded [5.45]; they used time steps of 50 to 100 times greater than that indicated by this criterion without reporting any stability limitations.

Another restriction for physically meaningful transient calculations is that the time step must be small enough that the Courant number is less than one, or the particles would jump across more than one computational cell during the time step Δt:

$$c \simeq \frac{v\Delta t}{h} \leq 1 \quad . \tag{5.36}$$

Assuming the saturation velocity of an electron in silicon and a time stop of 0.1 ps, a cell size greater than 0.01 μm is required. With our minimum element sizes several times this value, this criterion poses no difficulties for us.

Related to the dielectric relaxation time are the momentum and energy relaxation times. Lippens et al. [5.29] analyze nonequilibrium transport in silicon devices, and conclude that use of a mobility relationship such as SMDA limits the description of transient behavior to time scales greater than the momentum relaxation time (on the order of 10^{-14} s for high-energy carriers),

but Δt should also be less than the energy relaxation time. They suggest that a time step of 0.05 ps satisfies both these criteria. Since other particle simulations (e.g., reference [5.6]) have used this same value, we typically use this a time step of 0.05 to 0.1 ps in our simulations. With transient charge collection occurring on the order of picoseconds, this choice of Δt requires thousands of time steps. To reduce the computational time we can increase the time step in the later stages of the charge collection similar to the approach of Grubin et al. [5.45].

Particle Number

A typical number of particles used for PS techniques is 10,000, a number primarily determined by the limitation of computer resources. A trade-off exists between the number of particles and the number of nodes needed to simulate the semiconductor device. As an example, we can consider an incident ion with an LET of 12 MeV/(mg/cm^2), passing through a 5 x 5 x 5 μm^3 device with a dopant concentration of 10^{16} cm^{-3}. If we are limited to 10,000 particles, each would need to initially represent 900 electrons or holes on average. This charge would be reduced by recombination and/or charge collection at the contacts. Our PS technique is flexible in that equal-charged particles are not required; e.g., fewer particles of greater charge can simulate the slow-moving charge carriers in the core of the e-h plasma. PS permits flexibility in reapportioning charge to the particles in the course of the simulation or in changing the total number of particles simulated if desired. Because

thermal generation can continually increase the number of particles being simulated, we have implemented a particle reformulation subroutine to periodically combine the particles with little charge into those nearby particles with more significant amounts of charge.

One rule of thumb is the requirement of several particles per cell, to smooth out charge fluctuations on the nodes [5.19]. As a rule, we use at least five particles per element to represent the majority carriers, and three to five to represent the minority carriers. Under heavy doping conditions, we may use several times more particles per element for the majority carriers. For fine mesh simulations, we have typically used between five and ten thousand particles to simulate the device behavior, plus several thousand more to represent the charge track.

5.5.2 Summary of Potential Advantages of the FE/PS Method

The greatest advantage of our FE/PS method is its ability to handle transient analyses and nonequilibrium conditions. By allowing a device to evolve to steady state and then introducing a perturbation, e.g., an ion track, we can watch the evolution of the device profiles with time as it returns to equilibrium. The details and physics of transient device behavior can be studied in a way impossible for steady-state device simulation codes to duplicate. The number of particles can be increased in regions of interest to obtain greater accuracy in the analysis of device transients. However, for equilibrium conditions, our FE/PS method may not be

preferred because of the computational time required to let a device evolve to steady state. For these conditions a conventional code is most efficient.

Decoupling Poisson's equation from the current continuity equations reduces computational requirements of the matrix solutions. For highly perturbed conditions, this decoupling may simplify the solution where more conventional solution methods might have difficulty achieving convergence.

The formulation of the code introduces a number of advantages over previous FE and PS methods in device simulation. The quadratic formulation is designed to provide greater accuracy of potential field evaluations than linear formulations, permitting the use of larger elements and reducing computational requirements. Continuity of electric field across element boundaries is also maintained, reducing computational noise. The triangular elements allow simulation of irregular geometries, unlike the FFT solutions of potential traditionally used in PS applications. Our formulation can simulate the transport of both majority and minority carriers as well as recombination and thermal generation effects, making it more generally applicable to a wider range of device conditions than other PS codes.

The axisymmetric formulation is ideal for simulations involving charge tracks. Limitations arise, however, for certain device structures which cannot be realistically simulated without a full 3-D representation.

5.6 References

[5.1] S. Selberherr, Analysis and Simulation of Semiconductor Devices, Springer-Verlag, N.Y. 1984.

[5.2] M. Kurata, Numerical Analysis for Semiconductor Devices, Lexington Books, Lexington, Mass. 1982.

[5.3] B. T. Browne and J. J. H. Miller, eds., Numerical Analysis of Semiconductor Devices, Boole Press, Dublin, 1979, and additional proceedings of the NASECODE series of conferences held biennially.

[5.4] W. L. Engl, H. K. Dirks, and B. Meinerzhagen, Proc. IEEE, 71 (1983) 10.

[5.5] J. M. Dawson, Rev. Mod. Phys., 55 (2) (1983) 403.

[5.6] R. W. Hockney, R. A. Warriner, and M. Reiser, Electron. Lett., 10 (1974) 484.

[5.7] A. J. Davies, The Finite Element Method: A First Approach, Oxford University Press, N.Y. 1980.

[5.8] L. J. Segerlind, Applied Finite Element Analysis, John Wiley, N.Y., 1976.

[5.9] O. C. Zienkiewicz, The Finite Element Method, 3d ed., McGraw-Hill, N.Y. 1977.

[5.10] G. D. Hachtel, M. Mack, and R. R. O'Brien, "Semiconductor Device Analysis Via Finite Elements," in Conference Record, Eighth Asilomar Conference on Circuits, Systems, and Computers, (Pacific Grove, CA, Dec. 1974), pp. 332-338.

[5.11] J. J. Barnes and R. J. Lomax, IEEE Trans. Electron Devices, ED-23 (1976) 1042.

[5.12] J. J. Barnes and R. J. Lomax, IEEE Trans. Electron Devices, ED-24 (1977) 1082.

[5.13] J. J. H. Miller, ed., Finite Element Programming with Special Emphasis on Semiconductor Device and Process Modelling, Boole Press, Dublin, 1983.

[5.14] P. Silvester, IEEE Trans. Microwave Theory and Techniques, MIT-17 (1969) 204.

[5.15] A. Konrad and P. Silvester, Comp. Phys. Comm., 5 (1973) 437.

[5.16] R. C. Martin and N. M. Ghoniem, "Higher Order Axisymmetric Finite Element Solution of Poisson's Equation for Semiconductor Device Simulation," University of California Los Angeles report UCLA-ENG-8835/PPG-1195 (1988).

[5.17] J.-C. Sabonnadière and J.-L. Coulomb, Finite Element Methods in CAD: Electrical and Magnetic Fields, Springer-Verlag, N.Y. 1987.

[5.18] T. Adachi, A. Yoshii and T. Sudo, IEEE Trans. Electron Devices ED-26, 1026 (1979).

[5.19] R. W. Hockney and J. W. Eastwood, Computer Simulation Using Particles, McGraw-Hill, N.Y. 1981.

[5.20] The IMSL Library Reference Manual, Vol. 2, 9th edn. IMSL, Inc., Houston, Texas (1982).

[5.21] D. P. O'Leary and O. Widlund, Math. Comp., 33 (1979) 849.

[5.22] C. Moglestue, IEEE Trans. Computer-Aided Design, CAD-5 (1986) 326.

[5.23] R. A. Warriner, Solid-State and Electron Devices, 1 (1977) 97, 105.

[5.24] H. Rees, G. S. Sanghera, and R. A. Warriner, Electron. Lett., 13 (1977) 156.

[5.25] C. Moglestue and S. J. Beard, in Numerical Analysis of Semiconductor Devices, B. T. Browne and J. J. H. Miller, eds., Boole Press, Dublin, 1979 (pp. 232-236).

[5.26] J.-F. Pone, R. C. Castagné, J.-P. Courat, and C. Arnodo, IEEE Trans. Electron Devices, ED-29 (1982) 1244.

[5.27] C. Moglestue, in NASECODE 4: Proc. of the Fourth International Conf. on the Numerical Analysis of Semiconductor Devices and Integrated Circuits, J. J. H. Miller, ed., Boole Press, Dublin, 1985 (pp. 48-57).

[5.28] H. Oka and T. Nakamura, in J. J. H. Miller, ed., ibid. (pp. 460-465).

[5.29] D. Lippens, J.-L. Nieruchalski, and E. Constant, IEEE Trans. Electron Dev., ED-32 (1985) 2269.

[5.30] C. K. Birdsall and A. B. Langdon, Plasma Physics via Computer Simulation, McGraw-Hill, N.Y. 1985.

[5.31] M. R. Pinto, C. S. Rafferty and R. W. Dutton, "PISCES II: Poisson and Continuity Equation Solver," Stanford Electronics Laboratories, Stanford University, Stanford, CA (1984).

[5.32] S. Selberherr, A. Schutz, and H. W. Potzl, IEEE Trans. Electron Devices, ED-27 (1980) 1540.

[5.33] D. Y. Cheng, C. G. Hwand, and R. W. Dutton, IEEE Trans. Computer-Aided Design, CAD-7 (1988) 1017.

[5.34] C. Canali, C. Jacoboni, F. Nava, G. Ottaviani, and A. Alberigi-Quaranta, Phys. Rev. B, 12 (4) (1975) 2265.

[5.35] C. Jacoboni, R. Minder, and G. Majni, J. Phys. Chem. Solids, 36 (1975) 1129.

[5.36] G. Ottaviani, L. Reggiani C. Canali, F. Nava, and A. Alberigi-Quaranta, Phys. Rev. B, 12 (8) (1975) 3318.

[5.37] C. Jacoboni and L. Reggiani, Rev. Mod. Phys., 55 (3) (1983) 645.

[5.38] D. Hulin, A. Migus, C. Tanguy, and A. Antonetti, J. Lumin., 30 (1985) 262.

[5.39] H. Bergner, V. Brueckner, and M. Schubert, J. Lumin., 30 (1985) 114.

[5.40] J. M. Dorkel and Ph. Leturcq, Solid-St. Electron., 24 (9) (1981) 821.

[5.41] D. M. Caughey and R. E. Thomas, Proc. IEEE, 55 (1967) 2192.

[5.42] S. Selberherr, Microelectron. Reliab., 24 (1984) 225.

[5.43] P. R. H. Riemenschneider and K. L. Wang, IEEE Trans. Electron Devices, ED-30 (1983) 1142.

[5.44] M. Reiser, Comp. Meth. Appl. Mech. Eng., 1 (1972) 17.

[5.45] J. P. Kreskovsky and H. L. Grubin, J. Comput. Phys., 68 (1987) 420.

Chapter 6

ASSESSMENT OF THE FINITE ELEMENT/PARTICLE SIMULATION METHOD

6.1 Introduction

To ascertain the validity of the finite element/particle simulation method, comparison with known solutions of device physics equations is necessary. Approximate solutions for one-dimensional representations of p-n diodes have been worked out for some time [6.1]. Since then, significant effort has gone into the development of efficient numerical techniques for the accurate solution of device equaions in a variety of applications. It is not our intent to develop the FE/PS method as a general substitute for other numerical schemes, but rather as a specialized method for the simulation of fast transients, as in the case of single event upsets. However, in this chapter, we demonstrate that the results obtained from the FE/PS method are in good agreement with other solutions to device equations.

6.2 One-Dimensional Comparison with Analytical Potential Profiles

The simplest analytical result for the potential profile is that based on the depletion approximation for the open-circuit p-n junction [6.1]. The basis of the depletion approximation is that any applied or induced electric field removes all free carriers from the

depletion zone, with the only remaining space charge due to uncompensated donor and acceptor ions. This approximation allows determination of an analytical solution to Poisson's equation for the potential:

$$\phi = \frac{qN_a}{2\epsilon}(d_a + x)^2 \quad \text{for} \quad -d_a \leq x < 0 \quad ,$$
$$= \phi_o - \frac{qN_d}{2\epsilon}(d_d - x)^2 \quad \text{for} \quad 0 \leq x \leq d_d \quad , \tag{6.1}$$

with N_a and N_d the acceptor and donor doping densities respectively, q the charge on the electron, ϵ the dielectric constant, d_a and d_d the spatial extent of the depletion zone from the junction into acceptor and donor doping regions respectively, and ϕ_o the built-in potential at the junction given by:

$$\phi_o = \frac{kT}{q} \ln \frac{N_a N_d}{n_i^2} \quad , \tag{6.2}$$

with n_i the intrinsic carrier concentration. The total width of the depletion zone is given by:

$$W = \left[\frac{2\epsilon\phi_o}{q}(N_a^{-1} + N_d^{-1})\right]^{1/2} = d_a + d_d \quad . \tag{6.3}$$

This open-circuit condition for a silicon device with a doping of $\pm 10^{15}$ cm^{-3} gives the values W = 1.224 μm and ϕ_o = 0.5743 V.

One-dimensional (1-D) comparative computations were performed on an open-circuit silicon diode with 10^{15} cm^{-3} doping density on each side of an abrupt junction (i.e., no doping variation in the radial

direction). The device geometry is represented by Figure 6.1. For code input, the doping concentration at the junction is modeled as a step function from positive to negative doping densities of magnitude 10^{15} cm^{-3}. The depletion zone was allowed to evolve to steady state. The resulting potential and electric-field profiles were compared to the analytical solutions for the abrupt p-n junction and found to be in very good agreement. Figure 6.2 compares the results of our quadratic code with the analytical solution. Very good agreement was obtained for a grid spacing of 0.15 μm between the nodes, with a

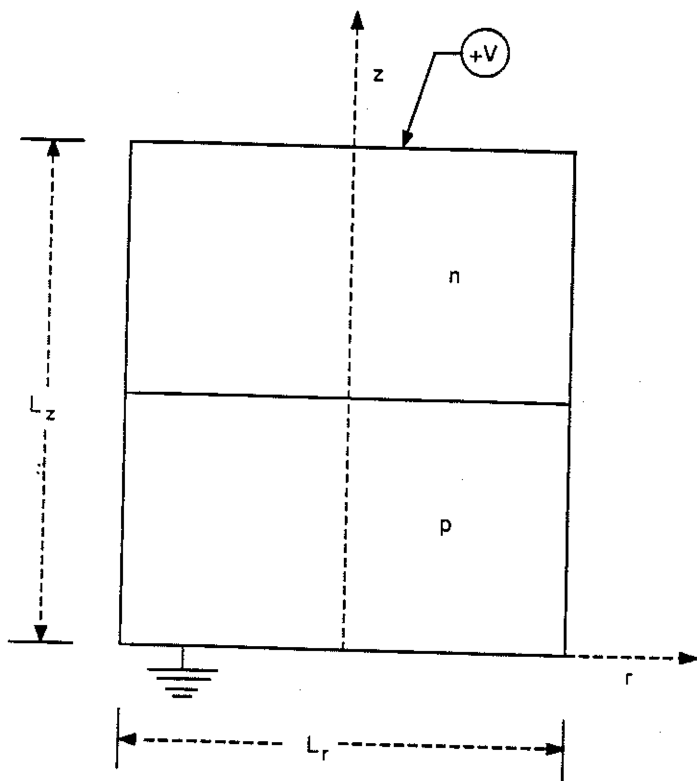

Figure 6.1: Axisymmetric 1-D device geometry showing geometry of the open-circuit silicon diode (V = 0 volts, L_z = 2.5 μm, L_r = four times the element size).

maximum deviation from the analytical potential of about 0.002 V. Even a large mesh spacing of 0.3 μm gives a good approximation, with a maximum error on the order of 0.01 V. Results obtained for a 0.15 μm grid spacing using linear shape functions is also plotted in Figure 6.2 for comparison, and the greater error resulting from linear interpolation and large grid spacings is apparent. The results provided by quadratic interpolation are shown plotted in r-z space in Figure 6.3. Figure 6.3(a) shows the potential profile over a 5 μm device with the p-n junction at the mid-point. Numerical variation of the potential in the r-direction is insignificant. Figure 6.3(b) shows the potential profile only over the depletion

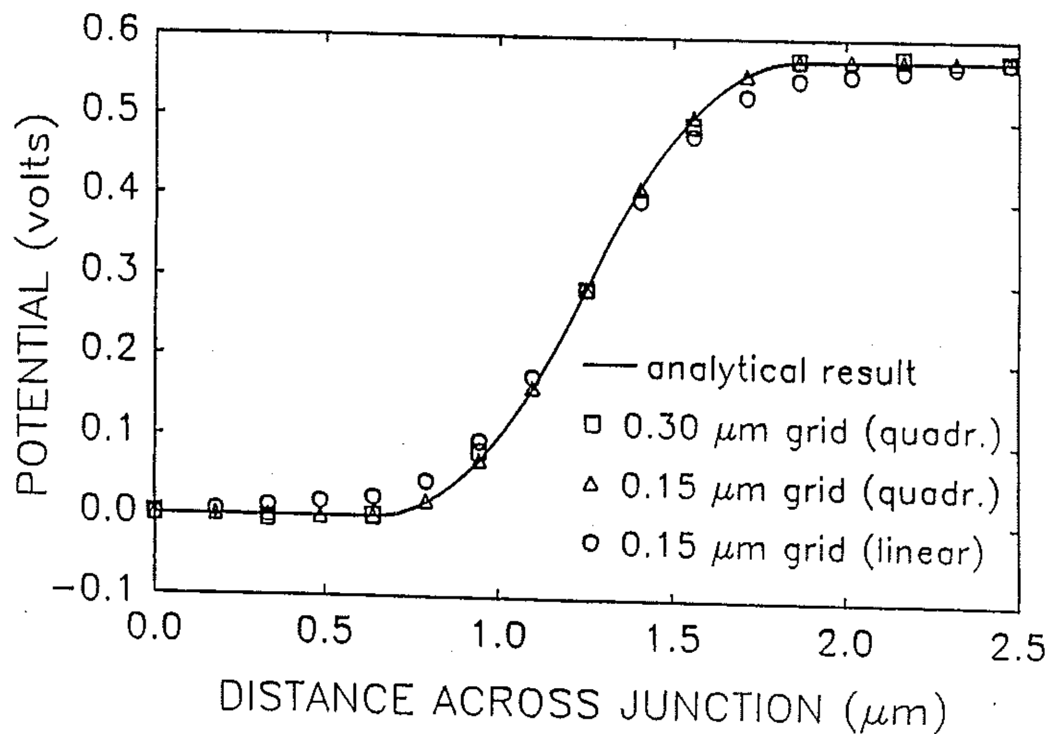

Figure 6.2: Comparison of calculated potential profiles to analytical results. Element size is twice the grid size.

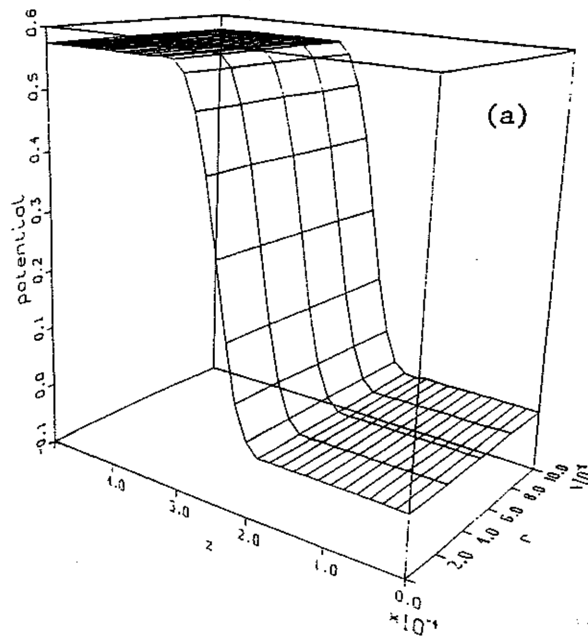

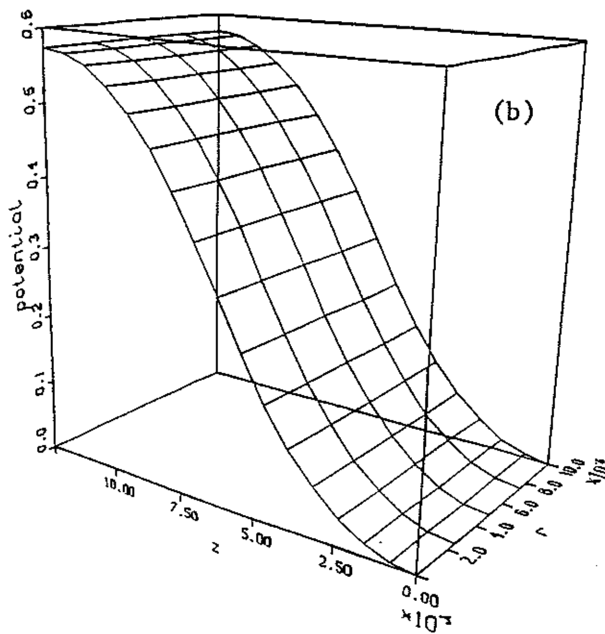

Figure 6.3: Calculated potential profile across open-circuit p-n junction, with 10^{15} cm^{-3} doping, for (a) 5 μm device (0.31 μm elements), and (b) 1.2 μm device (0.08 μm elements).

region, approximately 1.2 μm in length. The element size for Figure 6.3(a) is about 0.31 μm and for Figure 6.3(b) 0.08 μm.

Figure 6.4 shows the effect of element size on the error in the electric field calculation, for a device twice the length of the depletion zone. An abrupt junction is again simulated, with the charge density given by the depletion approximation. The error is calculated at several positions i along the device length, using the equation:

$$\epsilon_i = \frac{1}{N} \left| \frac{[(\Delta E_r)^2 + (\Delta E_z)^2]^{1/2}}{E^a_{max}} \right| , \tag{6.4}$$

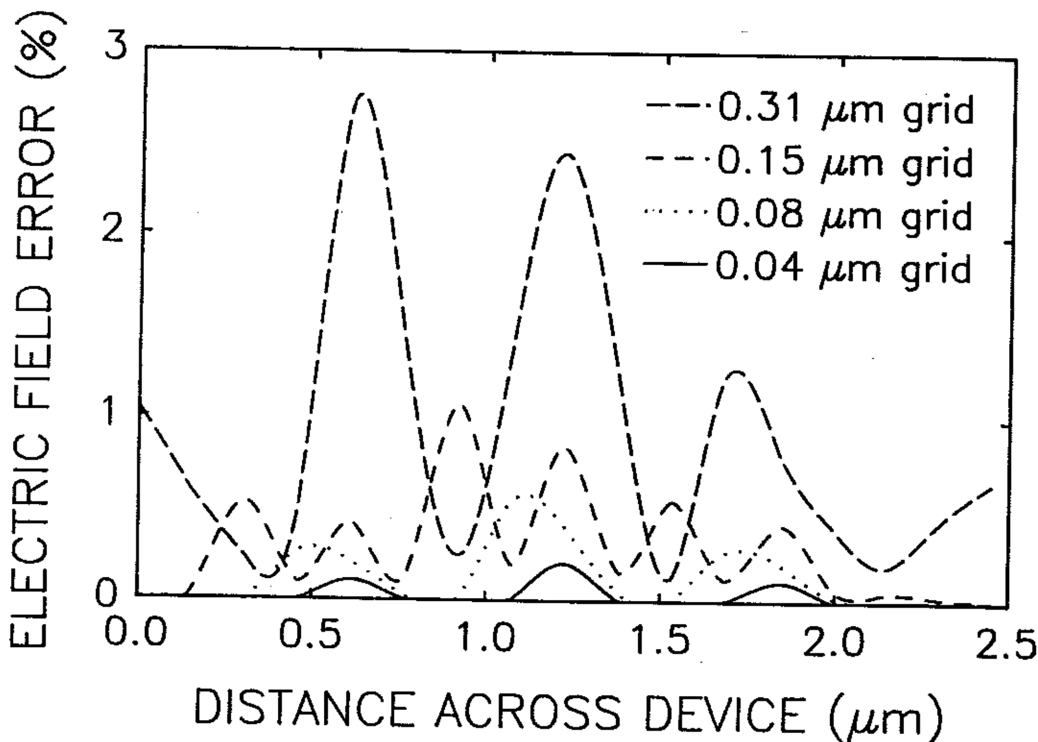

Figure 6.4: Dependence of the relative average radial error in the electric field on grid size and axial distance across the 2.5 μm device. Element size is twice the grid size.

with ΔE_r the total absolute error in the radial electric field, summed over the N radial mesh points at each axial position along the device, ΔE_z the sum of the total absolute error in the axial electric field, and E^a_{max} the maximum analytical electric field at the p-n junction. E^a_{max} for this open-circuit condition is given by [6.2]:

$$E^a_{max} = \frac{2\phi_o}{W} = 9384 \text{ V/cm} \quad , \tag{6.5}$$

with W the width of the depletion zone [equation (6.3)]. The analytical electric field varies linearly to zero at the edges of the depletion zone. Figure 6.4 shows that reducing element dimensions to 0.1 μm reduces the error to small magnitudes, and the error is concentrated at the locations which generate the most numerical difficulties: the p-n contact and the two ends of the depletion zone.

6.3 One-Dimensional Comparison with an Iterative Self-Consistent Finite Element Code

The depletion approximation permits useful simplification of actual charge carrier density profiles across the depletion zone. As a realistic comparison, our potential results were compared to another FE code written by Dr. Philip Chou of U.C.L.A., based on the Newton-Raphson iteration of the coupled current-continuity and Poisson equations [equations (5.1) to (5.3)] until a self-consistent steady state is achieved [6.3]. For this comparison, a 5 μm reverse-biased p-n junction similar to Figure 6.1 was simulated with an

applied potential of 3 volts and donor and acceptor doping densities of 10^{15} cm^{-3} across an abrupt junction. The free carrier densities as evaluated by the self-consistent code were used as the space charge input to our code, and the resultant potential calculated. The results are shown in Figure 6.5. Very good agreement is obvious across the device. A small increase in our potential values relative to the other code can be seen, but this is attributed to a net excess charge on the order of 10^9 cm^{-2} (integrated over the z-direction) from the concentration profiles used as input. This small charge imbalance arises from the error inherent in any non-exact iterative evaluation of the densities.

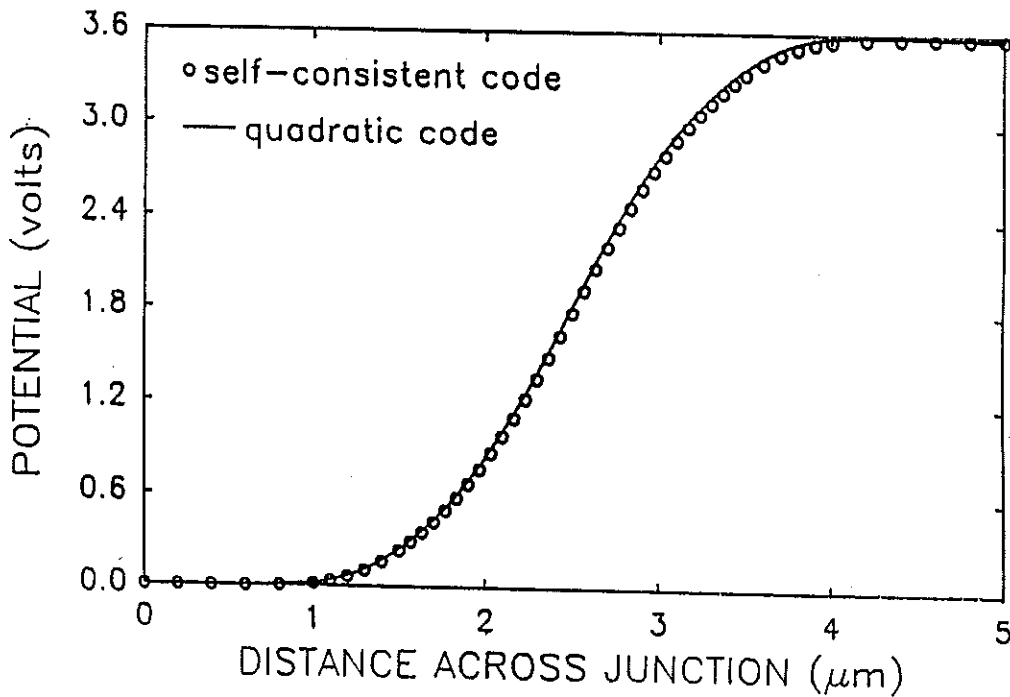

Figure 6.5: Comparison of calculated potential profile to self-consistent finite element results.

depletion zone forms and steady-state profiles are obtained, in good agreement with the benchmark calculations provided by the iterative self-consistent code.

Very good quantitative agreement between the two codes is obtained for majority carrier profiles and effective depletion widths. Minority carrier profiles show some variation, but these are not significant for realistic device modeling. The computational noise apparent in the density profiles is inherent in the particle method. An average of 15 particles each for positive and negative charge per element were used in this simulation. Simulations using half this average number showed no significant difference in the overall profiles, but slightly more noise in the density profiles. Although quadratic interpolation of carrier densities is used in the Poisson solution, the densities in Figures 6.6(a) and 6.6(b) are represented by linear interpolation to the corner nodes. We determined that quadratic visualization of the densities (6 nodes per triangle) showed systematic oscillations at non-corner nodes.

Figure 6.6(c) also shows very good agreement between the steady-state potential profiles obtained by the two codes. The PS code offers the advantage of observing the transient evolution of the device toward steady state. Because of large electron mobilities, the electron density profiles for these low doping levels quickly approach steady state within 0.25 ns. The lower hole mobilities prevent hole density profiles from approaching steady-state for a few ns; the minority carrier hole profiles gradually decline due to drift, diffusion, and recombination. Figure 6.6(c) shows the

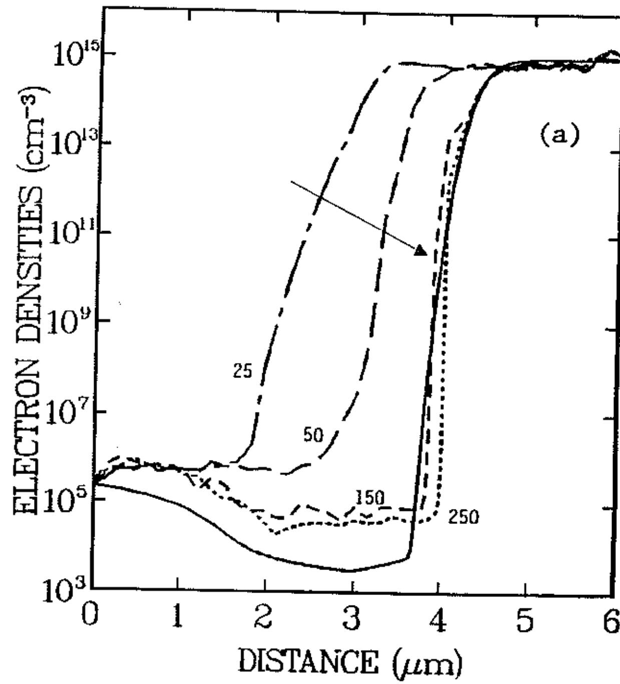

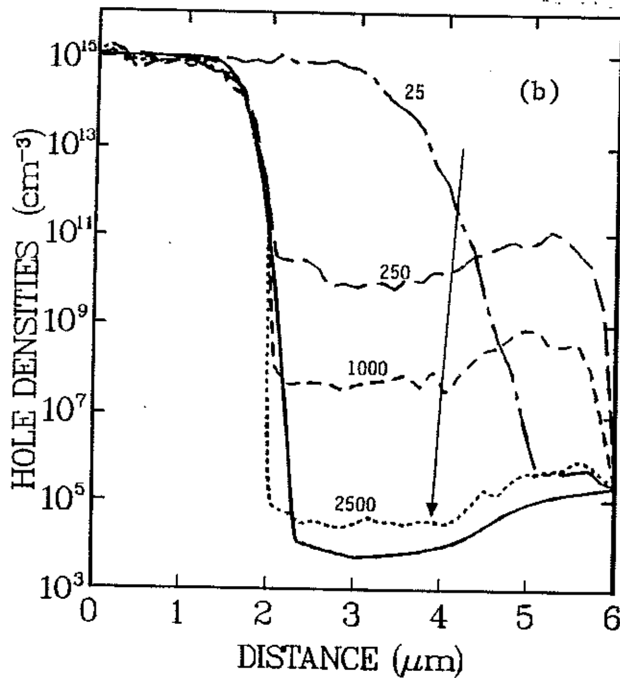

Figure 6.6: Evolution of density and potential profiles with time, after applying 3 volts reverse-bias to a 6 μm long, 1-D silicon diode. The FE/PS code results (at times given in ps) for (a) electron and (b) hole carrier densities, and (c) potential profile. The solid lines give steady-state results from iterative self-consistent FE code. Arrows indicate direction of profile evolution with time.

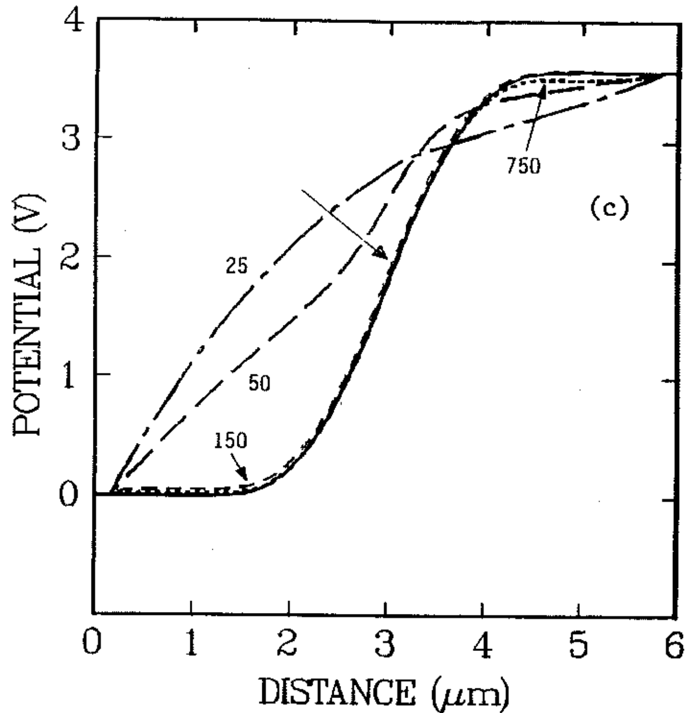

Figure 6.6: Evolution of density and potential profiles with time, after applying 3 volts reverse-bias to a 6 μm long, 1-D silicon diode. The FE/PS code results (at times given in ps) for (a) electron and (b) hole carrier densities, and (c) potential profile. The solid lines give steady-state results from iterative self-consistent FE code. Arrows indicate direction of profile evolution with time.

potential distribution approaches steady state on a time scale comparable to the electron distribution.

Figures 6.7(a) and 6.7(b) show carrier density and potential profiles at steady state for fine and coarse grids, compared to the benchmark calculations of the iterative code. The profiles obtained by the FE/PS code using a fine mesh (0.15-μm element size, 0.075 μm between mesh points) show very good agreement with the self-consistent code. Surprisingly, even the profiles obtained using a very coarse mesh (0.25 μm between mesh points) are in good

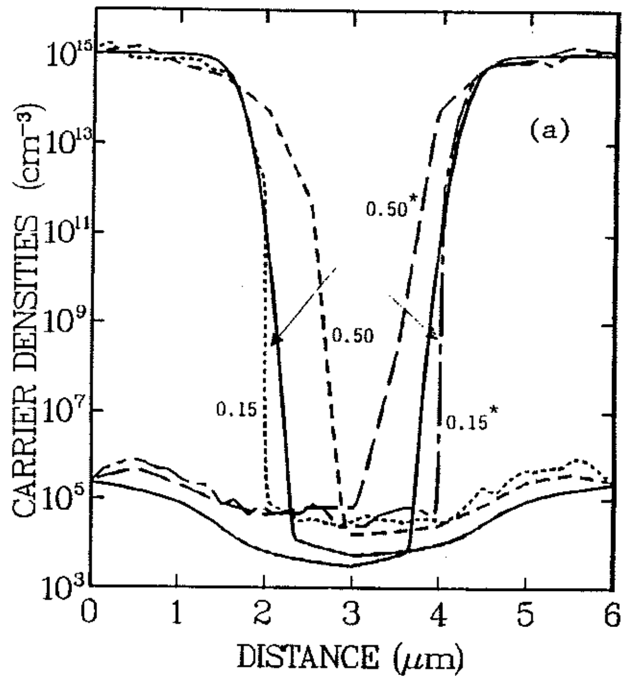

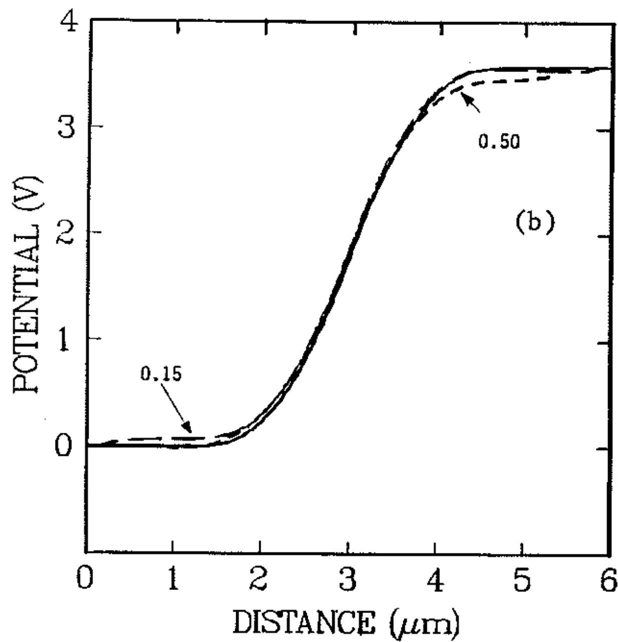

Figure 6.7: Effect of grid element size (in μm) on steady-state profiles, showing FE/PS code results at 2.5 ns for (a) electron (starred) and hole carrier densities (arrows indicate change from coarse to fine grid) and (b) potential profiles. The solid lines show steady-state results from iterative self-consistent FE code.

qualitative agreement for carrier densities and close to quantitative agreement for potential profiles. These results suggest that the quadratic FE formulation reduces the restrictions on small mesh spacings as suggested for typical device simulations [6.4].

Figures 6.8(a) and 6.8(b) show the steady-state results for a more typical silicon diode, with n^+-region doping densities of 10^{17} cm^{-3} and p-region doping of 10^{15} cm^{-3}. Also shown are the results of the self-consistent code. The average number of majority carrier particles per element is increased ten-fold within the n^+-region to accommodate the hundred-fold increase in doping density. The doping profile does not assume an abrupt junction, but rather uses an analytical doping expression previously used in another simulation to better represent a graded junction [6.5]:

$$N_d^+ - N_a^- = 1.01 \times 10^{17} \exp[-116.54(1 - \chi^2)] - 10^{15} \text{ cm}^{-3} \quad , \quad (6.6)$$

where χ is a dimensionless distance across the device (0.0 at the p-region contact, 1.0 at the n^+-contact, and 0.8 at the junction for this 5-μm device). The use of this doping profile is more realistic than an abrupt junction, and also reduces the computational difficulties inherent in a discontinuous order-of-magnitude change in doping densities across the junction.

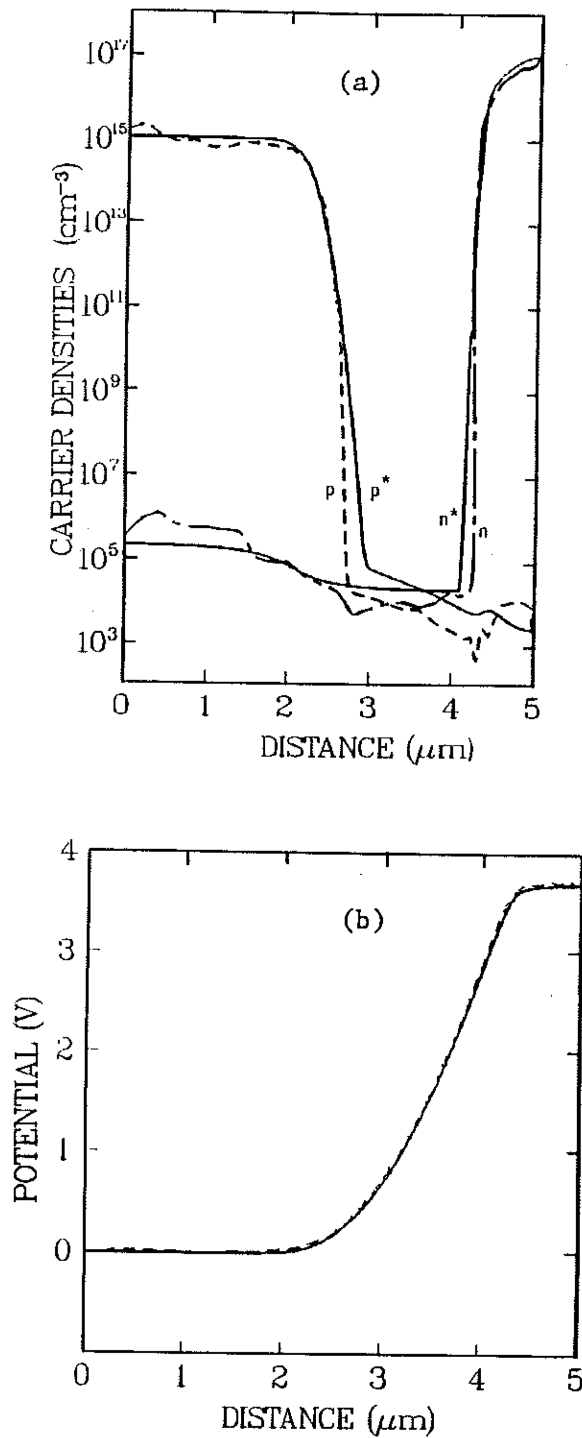

Figure 6.8: Steady-state profiles for 3-volt reverse-bias, 5 μm silicon diode with n^+ doping of 10^{17} cm^{-3} and p doping of 10^{15} cm^{-3}, showing (a) FE/PS code results at 900 ps for electron (n) and hole (p) densities and iterative FE code results (n^* and p^*); and (b) potential profiles for FE/PS (---) and iterative FE (——) codes.

6.4 Current-Voltage Characteristics

To test the effect of applied voltage on diode current density for our method, we again simulated the silicon diode represented by Figure 6.1, with doping of $\pm 10^{15}$ cm^{-3}, length of 6 μm, width of 0.3 μm, and element size of 0.15 μm. An approximate analytical expression is available for diode current density as a function of voltage [6.6]:

$$J = J_s[\exp(qV_a/kT) - 1] \quad , \tag{6.7}$$

with the saturation current density J_s given by:

$$J_s = \left[\frac{qD_p}{L_p}\right]p_n + \left[\frac{qD_n}{L_n}\right]n_p \quad , \tag{6.8}$$

with V_a the applied voltage, and p_n and n_p representing the equilibrium minority carrier densities in the n and p regions respectively. L_n and L_p are the diffusion lengths given by:

$$L_i = (D_i \tau_i)^{1/2} \quad , \tag{6.9}$$

for carrier type i, with τ_i the carrier lifetime, D_i the carrier diffusivity, and q, k, and T having the standard meanings. This equation only portrays realistic device response at reverse bias and weak forward bias (i.e., the applied voltage never significantly exceeds the opposing built-in voltage at the p-n junction). To test the response of our model over a wider range of voltage, we again used the results from the iterative self-consistent FE code as a comparative measure.

At each value of applied voltage, we ran our code until steady-state current results were obtained. The current is represented by a combination of the charge on the particles which escape the ends of the device, plus the adjustment of the charge in the boundary elements to impose equilibrium electron and hole densities for the device boundary condition, as discussed in Section 5.4.3, equation (5.33).

Figure 6.9(a) shows our current density results compared to the results of the iterative FE code, for identical device conditions, over the range of applied bias from -3 to +3 volts. Our results show very good agreement with the iterative FE code over all voltages except the strong forward bias conditions above 2 volts, values large for typical device operation. The analytical expression is also plotted for comparison, with its range of validity obviously restricted to applied potentials on the order of the built-in potential. Figure 6.9(b) amplifies the weak forward bias regime, to show the expected exponential relationship of our results at weak forward bias.

Although the comparison is very good for these low doping conditions, the amount of computer time required for our FE/PS method to achieve steady-state current is prohibitive relative to the iterative code. This factor reinforces the strength of our method for transient simulations relative to steady-state simulations. Conventional device simulation codes are well-suited for simulations of steady-state solutions, but they are not typically designed to

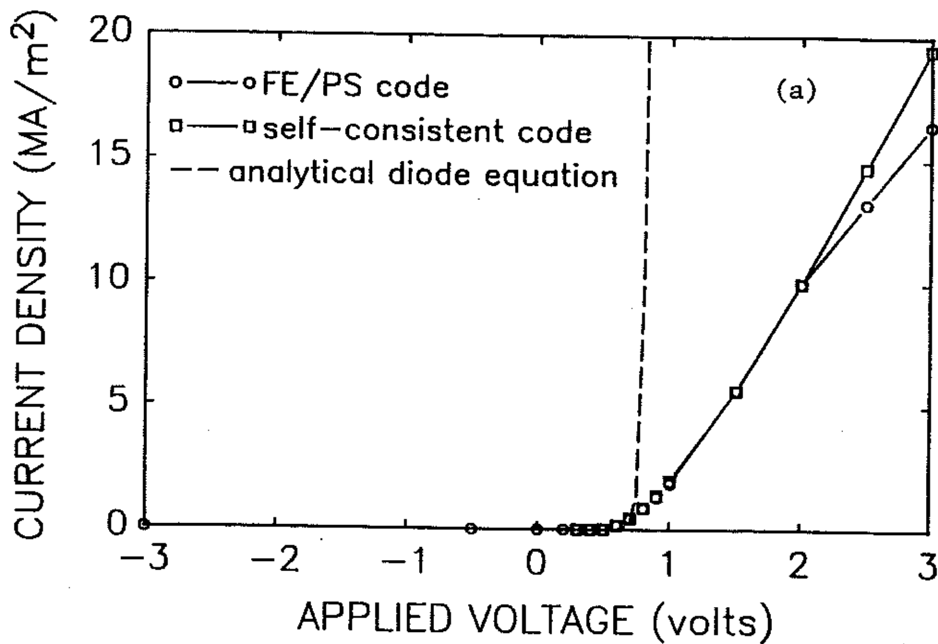

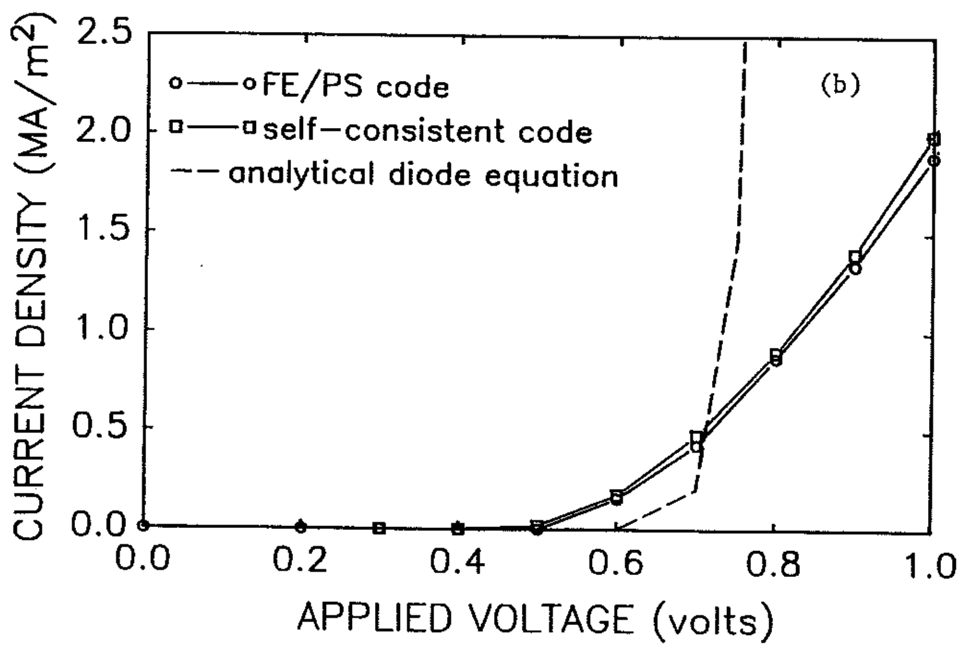

Figure 6.9: Comparison of calculated current-voltage characteristics of a 6 μm silicon diode to the self-consistent FE code results, for voltage ranges of (a) -3 to +3 volts, and (b) 0 to +1 volts. Device doping is $\pm$ 10^{15} cm^{-3}. Dotted line gives the results from the analytical diode equation.

demonstrate transient behavior in a computationally straightforward manner as does our code.

Although these results for low doping are reasonable, simulation of device current-voltage characteristics for heavy doping is not as simple. For doping of 10^{18} cm^{-3} and above, each superparticle represents orders of magnitude more charge than this simulation, and the transport of few superparticles with very large charge introduces significant error in the current relative to many particles with little charge in each. Under such conditions, the imposition of electron and hole density equilibrium in the boundary elements has a very sensitive effect on the resulting current in terms of particle creation and placement, numbers of particles created, etc. For these reasons, we did not pursue assessment of I-V characteristics at higher densities.

6.5 Three-Dimensional Potential and Density Profiles

Figures 6.10 and 6.11 demonstrate the axisymmetric 3-D capabilities of our code, with maximum n^+-region doping of 10^{18} cm^{-3} and p-region doping of 10^{15} cm^{-3}. A schematic of the silicon device simulated is shown in Figure 6.10; due to symmetry only half of the device is modeled. For comparative purposes, the graded doping profiles used were identical to those used by Kreskovsky and Grubin [6.5]:

$$C = (N + P_s) \exp(-a\ell^2) - P_s \quad , \qquad (6.10)$$

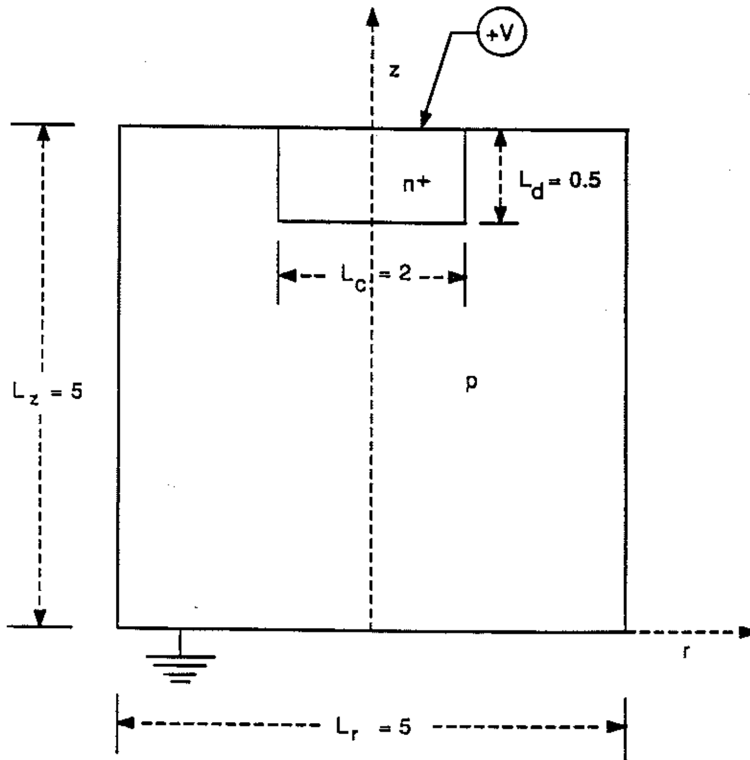

Figure 6.10: Axisymmetric 3-D device simulation showing geometry of the reverse-biased silicon diode ($V = 3$ volts, geometry units are in μm). n^+-doping maximum is 10^{18} cm^{-3}, and p-doping is 10^{15} cm^{-3}.

with
$$a = -\frac{1}{\ell_o} \ln\left[\frac{P_s}{N^+ + P_s}\right] \quad , \tag{6.11}$$

for $N^+ = 10^{18}$ cm^{-3}, $P_s = 10^{15}$ cm^{-3}, $\ell_o = 0.5$ μm, and:

$$\begin{aligned} \ell &= z \quad , && \text{for } r \le 0.5\ \mu m \quad , \\ \ell &= [z^2 + (r - 0.5)^2]^{1/2} \quad , && \text{for } r > 0.5\ \mu m \quad . \end{aligned} \tag{6.12}$$

Figure 6.11 shows the potential, electron density, and hole density profiles after evolution to steady state, and Figure 6.12

shows contour plots of the profiles represented by Figure 6.11. These profiles show good agreement with previous simulations using similar device conditions and geometry, such as those portrayed in Figure 6.13, taken from reference [6.5]. The density contours of Figure 6.13 appear to be based on a linear scale, while ours are based on a logarithmic scale. The potential contours of Figure 6.13 show more potential gradient within the n^+-region than do ours in Figure 6.12; as the doping exceeds 10^{17} cm^{-3} over all but the edges of the n^+-region, our results appear to be more consistent due to exclusion of the depletion zone from the n^+-region and expected lack of potential gradients.

As a measure of the computational accuracy of our method, we used this 3-D device geometry as the basis for measuring the relative error in potential calculations as a function of element size. We let the device evolve to steady state using 0.5 μm element sizes, halved the element size and let the device again obtain steady state, and compared the potential values at the same mesh points for the two cases using the L^2-norm error measure:

$$\epsilon_M = \frac{1}{\Phi_{max}} \left[\frac{1}{N_g} \sum_{j=1}^{N_g} (\Phi_j^{M+1} - \Phi_j^M)^2 \right]^{1/2} , \tag{6.13}$$

with Φ_{max} the maximum potential across the device (3 volts for this case), and the potential values Φ_j for element sizes M and M+1 compared over each of the N_g grid points. We continue halving the element size and compare consecutive cases. The results are plotted in Figure 6.14, which shows that the relative error converges to a

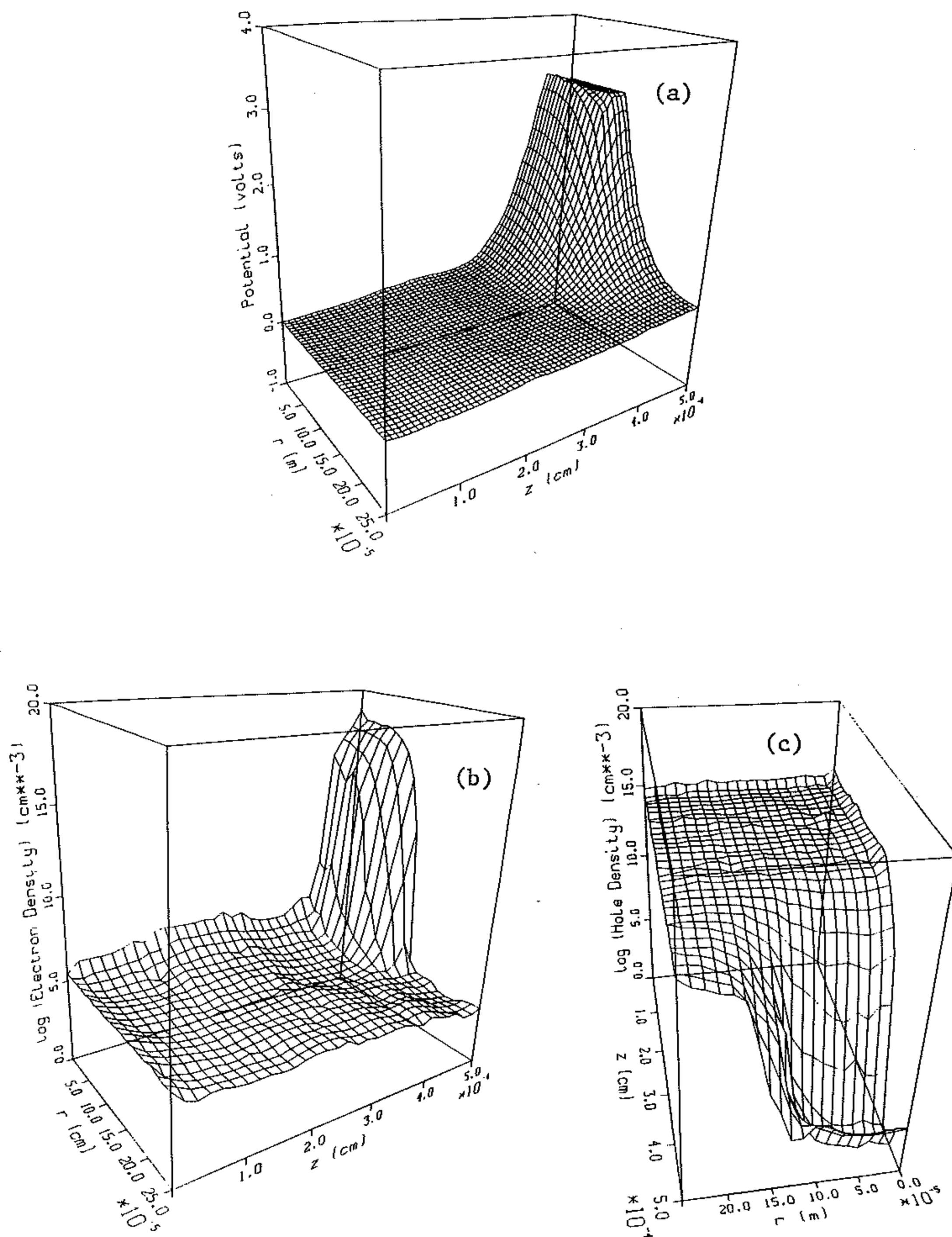

Figure 6.11: Axisymmetric 3-D device simulation at steady-state showing (a) potential, (b) electron, and (c) hole profiles. Viewing perspective of (c) is reversed from (a) and (b).

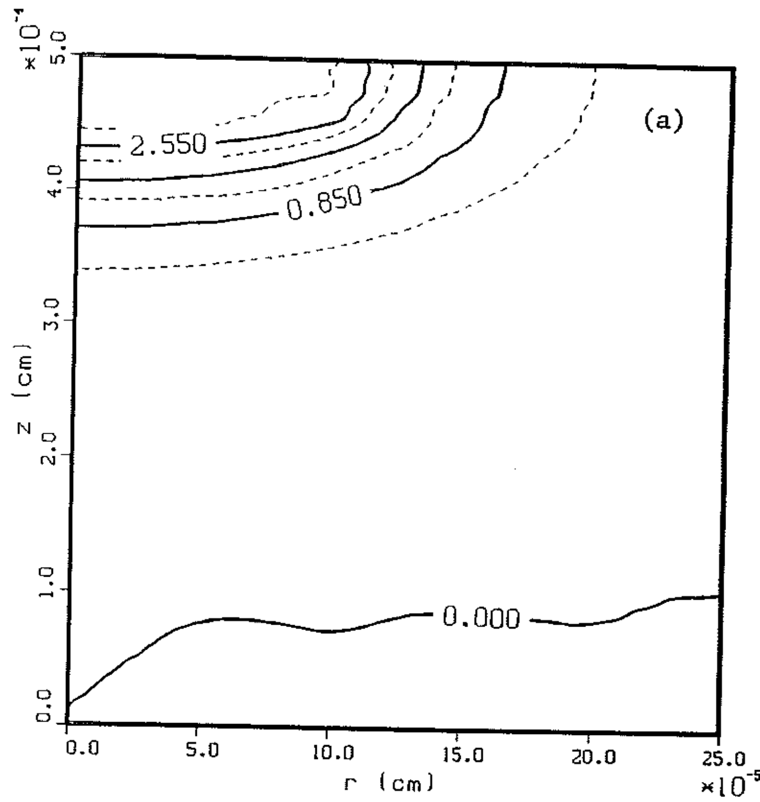

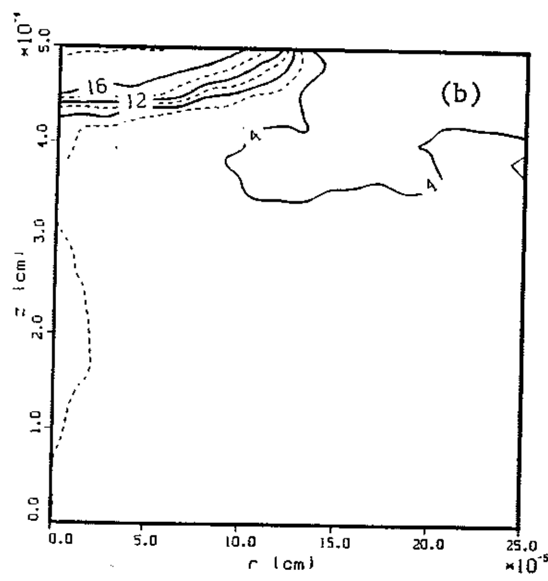

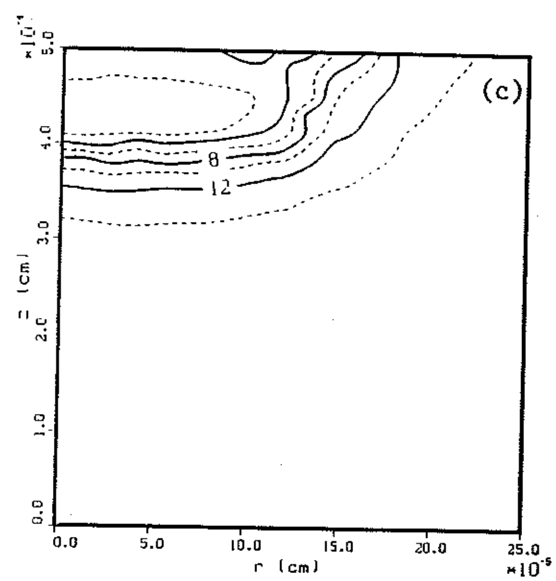

Figure 6.12: Contour plots for axisymmetric 3-D device simulation at steady-state showing (a) potential, (b) electron, and (c) hole profiles. Each contour line represents 0.425 volt change in potential, or two orders of magnitude change in density.

small value as element sizes are reduced to the order of 0.1 μm. This result shows that the numerical method is convergent with reduction of the element size.

These simulations use time steps of 0.05 ps for initial device evolution, with the time step subsequently increased to 0.1 ps as the device approaches steady state. Time steps as large as 0.5 ps are used for light doping conditions. This choice of time step is in the range of the dielectric relaxation time criterion discussed in Section 5.5.1. The effect of time step on simulation results will be analyzed in more detail in Section 7.2. Other applications of PS to device simulations typically use a time step of 0.05 ps.

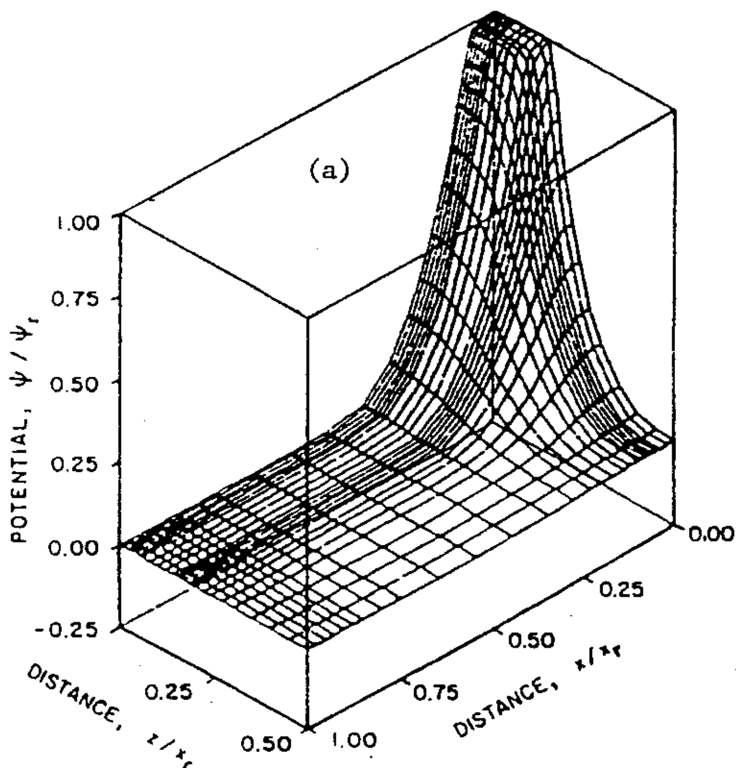

Figure 6.13: Steady-state profiles from Kreskovsky and Grubin 3-D simulation [6.5], showing (a) 3-D potential profile, and contour plots for (b) potential, (c) electron, and (d) hole profiles. Device geometry is identical to Figure 6.10.

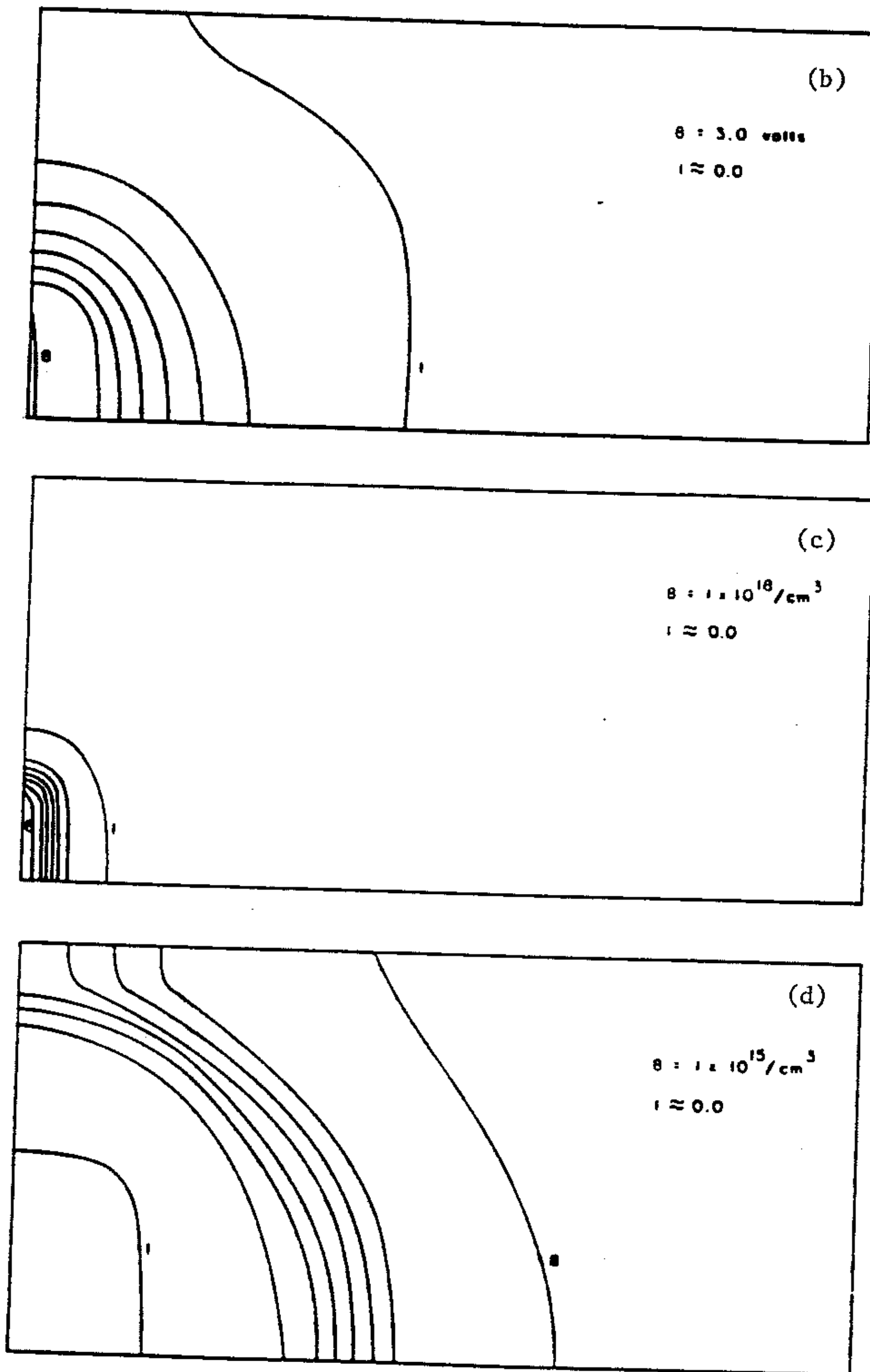

Figure 6.13: Steady-state profiles from Kreskovsky and Grubin 3-D simulation [6.5], showing (a) 3-D potential profile, and contour plots for (b) potential, (c) electron, and (d) hole profiles. Device geometry is identical to Figure 6.10.

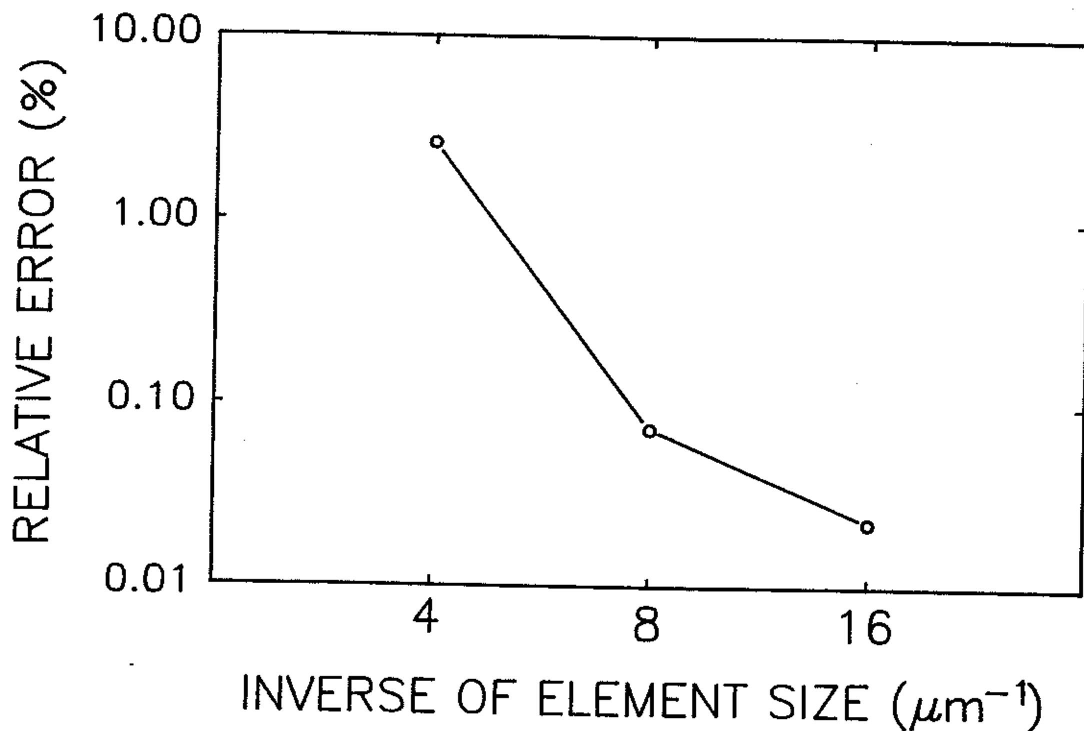

Figure 6.14: Reduction in relative computational error as a function of the element size.

6.6 Summary

Good results are apparent for our methodology in the previous examples. Our quadratic FE formulation permits element sizes considerably larger than previous PS device simulations have reported. Convergence of potential for decreasing element size has been demonstrated.

The strength of our code is in its ability to handle transient simulations. For simulations of steady-state and equilibrium behavior, traditional device simulation codes have the advantage of

speed of solution compared to our simulations, which must allow device evolution to steady state over time.

To our knowledge, no attempts to use PS methods for charge densities as large as 10^{18} cm^{-3} have been published. Although we have seen potential perturbations within these heavily-doped regions with our method, requiring a judicious choice of mesh sizes, we have successfully simulated these large densities and, as will be seen, have simulated much higher transient ion track densities and achieved reasonable results. With previous applications of PS methods believed limited to doping concentrations of 10^{17} cm^{-3} device doping [6.7], we feel our extension of PS methods to high density regimes to be a significant development.

6.7 References

[6.1] R. A. Smith, Semiconductors, 2d ed., Cambridge University Press, Cambridge, England, 1978 (p. 207).

[6.2] J. P. McKelvey, Solid State and Semiconductor Physics, Harper and Row, New York, 1966 (ch. 12).

[6.3] S. P. Chou and N. M. Ghoniem, "Finite-Element Solution of Coupled Poisson and Electron-Hole Continuity Equations for Semiconductor Devices," University of California Los Angeles report UCLA-ENG-8834/PPG-1194 (1988).

[6.4] M. R. Pinto, C. S. Rafferty and R. W. Dutton, "PISCES II: Poisson and Continuity Equation Solver," Stanfort Electronics Laboratories, Stanford University, Stanford, CA (1984).

[6.5] J. P. Kreskovsky and H. L. Grubin, J. Comput. Phys., 68 (1987) 420.

[6.6] K. G. Nichols and E. V. Vernon, Transistor Physics, Chapman and Hall, London, 1966 (ch. 7).

[6.7] J.-F. Pone, R. C. Castagné, J.-P. Courat, and C. Arnodo, IEEE Trans. Electron Devices, ED-29 (1982) 1244.

Chapter 7

NUMERICAL SIMULATION OF SINGLE EVENT UPSETS

7.1 Comparison with Previous Single Event Upset Simulations

The SEU simulation of Kreskovsky and Grubin [7.1,7.2] provides a detailed numerical evaluation of charge collection and transient current pulse, and we repeated the simulation to compare our results to theirs. We extended the steady-state 3-D simulation of Section 6.5 for the axisymmetric silicon diode represented by Figure 6.10, by introducing an ion track through the n^+-contact identical to that used in Ref. [7.1]: 4.5 μm long, 0.0565 μm in radius, extending along the device axis and ending 0.5 μm above the ground contact, with uniform N_α of 10^{18} cm^{-3} for a total track charge of 7.23 fC each for electrons and holes. The only differences between the two simulations was in the collection area of the n^+-contact with respect to total device cross section (16% for our simulation vs. 40% for theirs) and in the generation time of the track: we introduced our track instantaneously at time equals zero, while theirs assumed a generation time constant of 3 ps [equation (3.1)] for a total generation time of about 10 ps.

Figure 7.1 shows the evolution of the 3-D profile of electron density across the device with time. Figure 7.1(a) shows the steady-state profile, followed by the perturbed profile generated by the ion track at several times after introduction of the track. Figure 7.2 shows the corresponding electron density contours, at 2.5 ps after

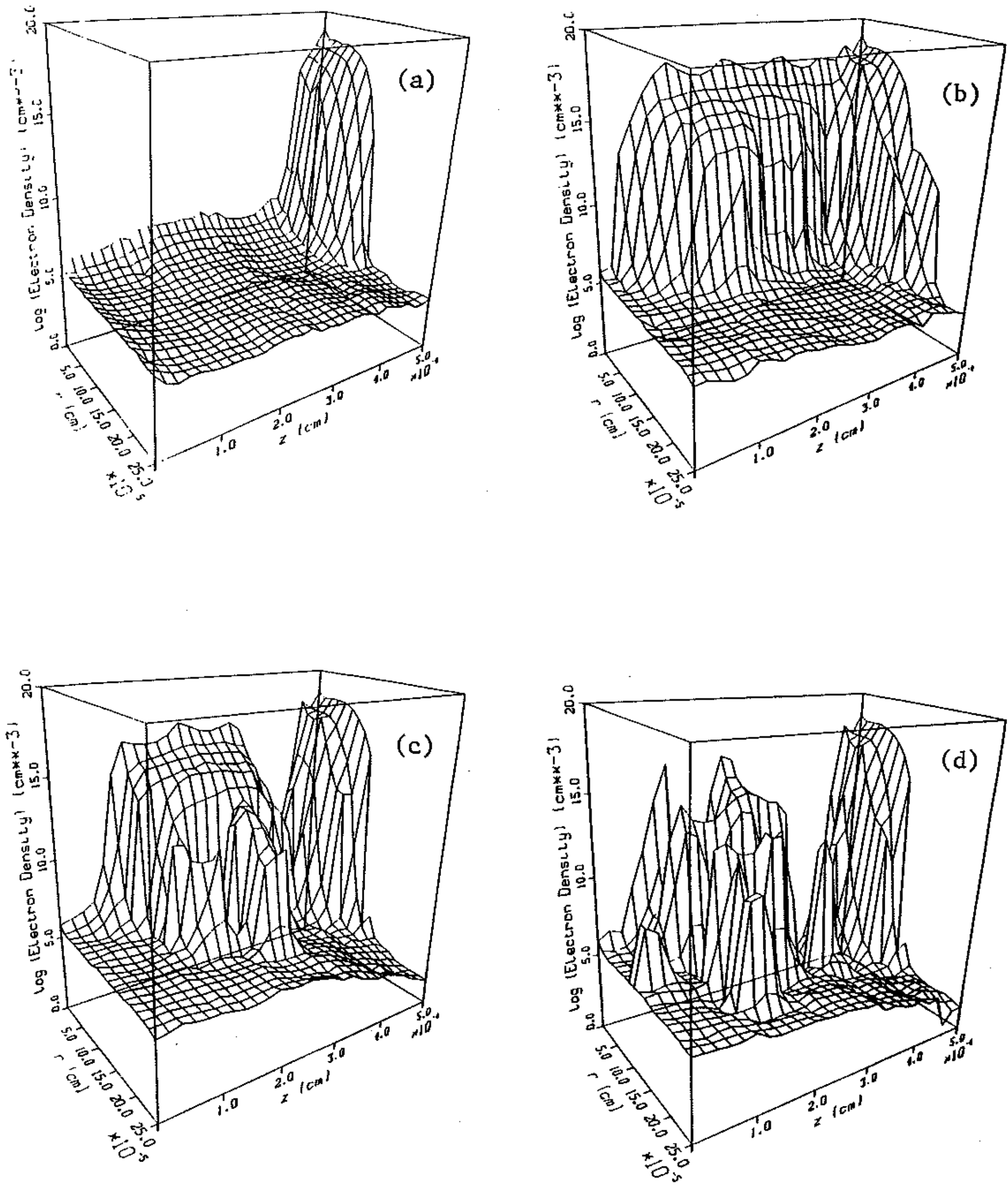

Figure 7.1: Evolution of 3-D electron profile with time after introduction of ion track at t = 0, for (a) steady-state at t = 0, (b) 70 ps, (c) 240 ps, and (d) 450 ps. Ion track is 4.5 μm long, 0.0565 μm in radius, with uniform density of 10^{18} cm^{-3}.

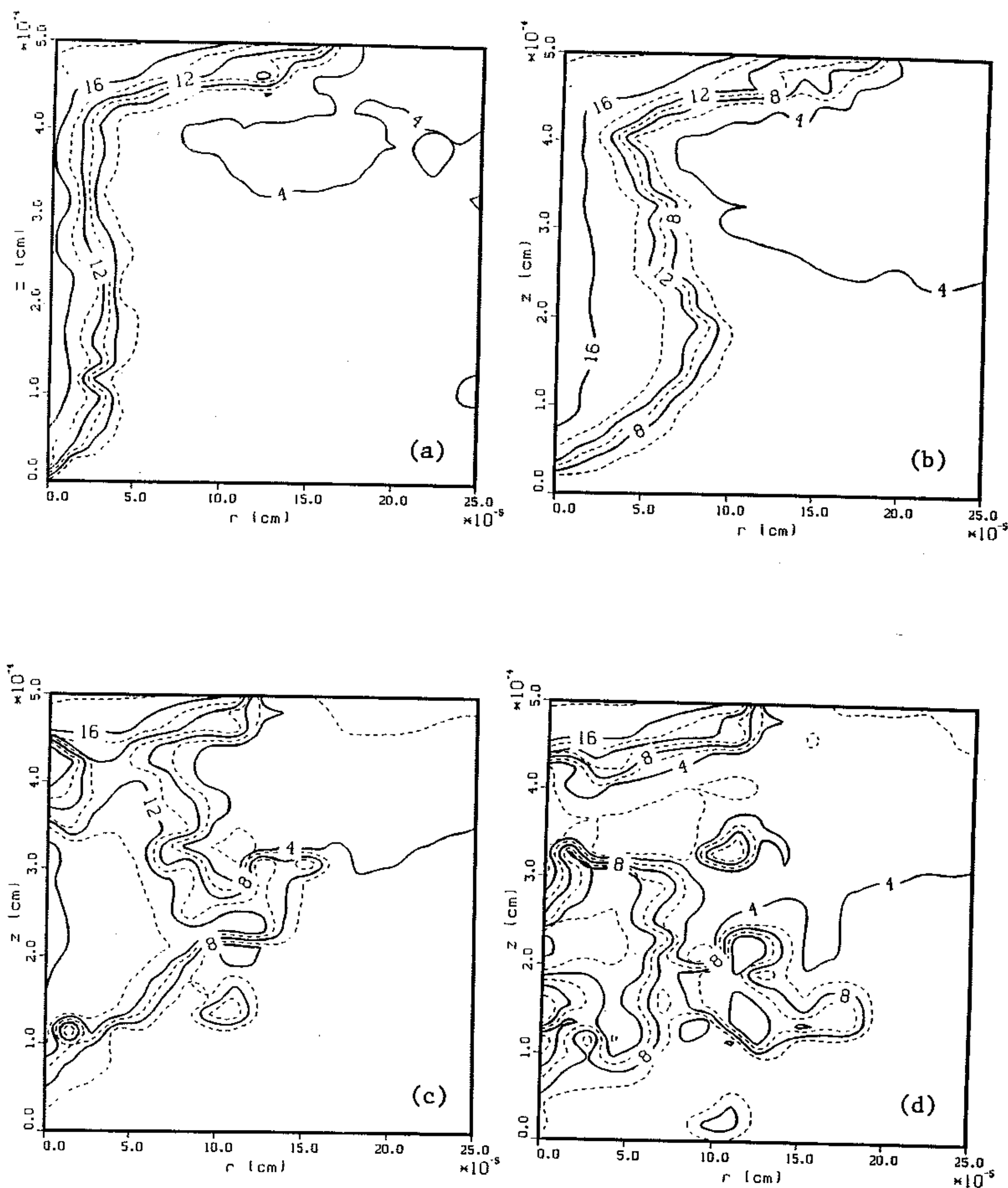

Figure 7.2: Evolution of electron density contours with time, similar to Figure 7.1, at (a) 2.5 ps, (b) 70 ps, (c) 240 ps, and (d) 450 ps. Each contour line represents two orders of magnitude change in density. Legends represent the logarithm of the density.

track introduction and then at later times corresponding to Figure 7.1. Outward diffusion of the track electrons with time is apparent, and collection of electrons by drift within the depletion zone causes pinchoff of the track from the n^+-contact by 240 ps, with continuing decay and outward diffusion of the track at 450 ps. The track profile of Figure 7.1(d) would appear smoother if more particles were used to represent the track. Over 4000 particles were used to represent the initial track, compared with about 10,000 particles for the device at steady-state. Electron profiles are shown rather than holes because the difference between track and background hole concentration within the p-region is less significant (3 orders of magnitude at most compared to 13 for electrons within the p-region) and thus track evolution is less distinct with respect to hole densities.

Figure 7.3 shows the evolution of the 3-D potential profile with time, corresponding to Figures 7.1 and 7.2. At 10 ps the potential is slightly perturbed, but the funnel effect develops over 100 ps as the potential field is pulled down into the substrate to enhance charge collection from the bulk. By 240 ps the field has been fully restored. The perturbations apparent along the device axis ($r = 0$) arise as an artifact of the axisymmetric formulation: small variations in the magnitude of the free charge near $r = 0$ appear as larger variations of charge density due to the small element volumes along the axis. Figure 7.4 shows contour plots of potential corresponding to Figure 7.3: the funnel effect is very noticeable in Figures 7.3(b) and 7.3(c). With the field fully restored by 240 ps,

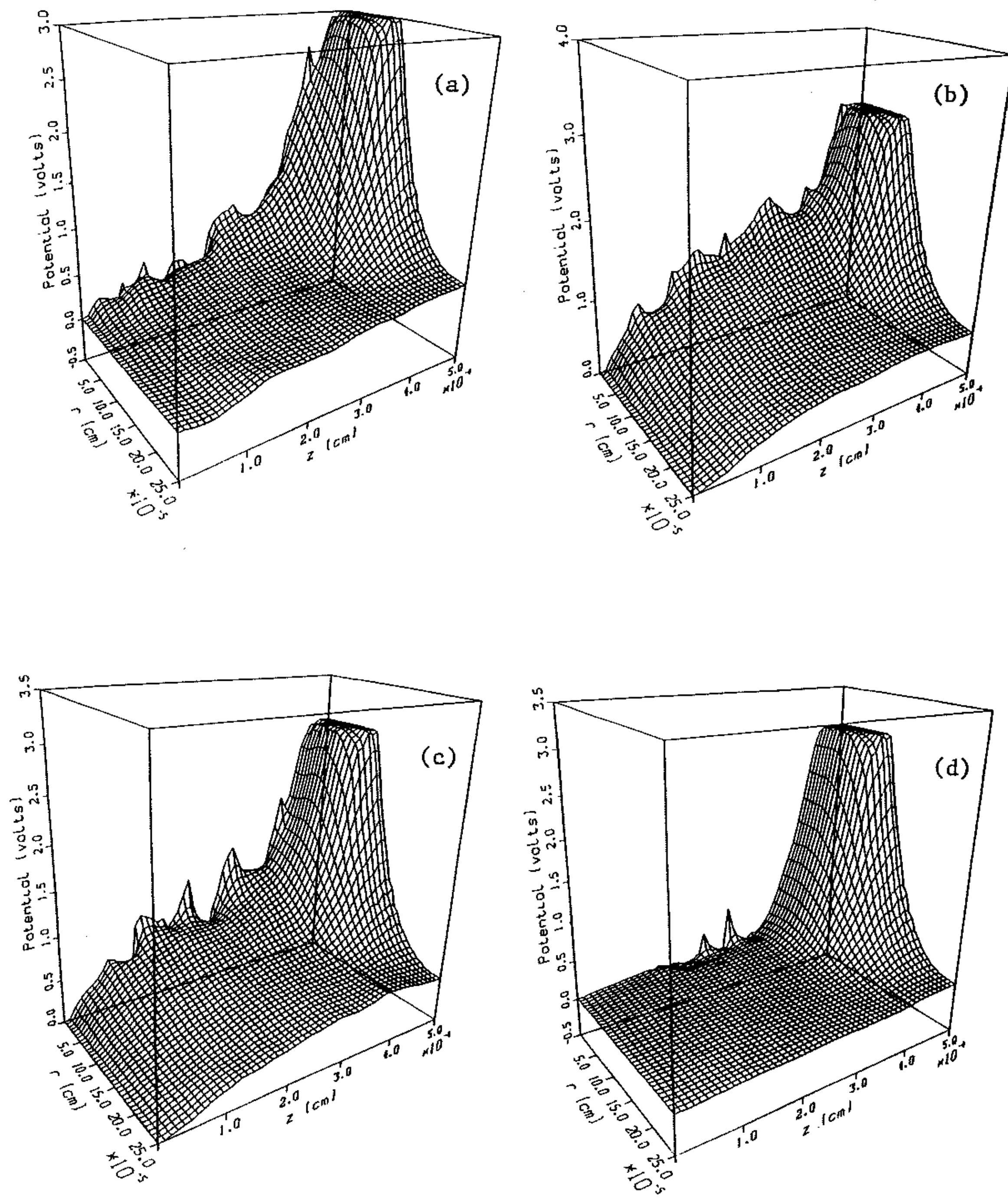

Figure 7.3: Evolution of 3-D potential profile with time after introduction of ion track, at (a) 10 ps, (b) 70 ps, (c) 120 ps, and (d) 240 ps.

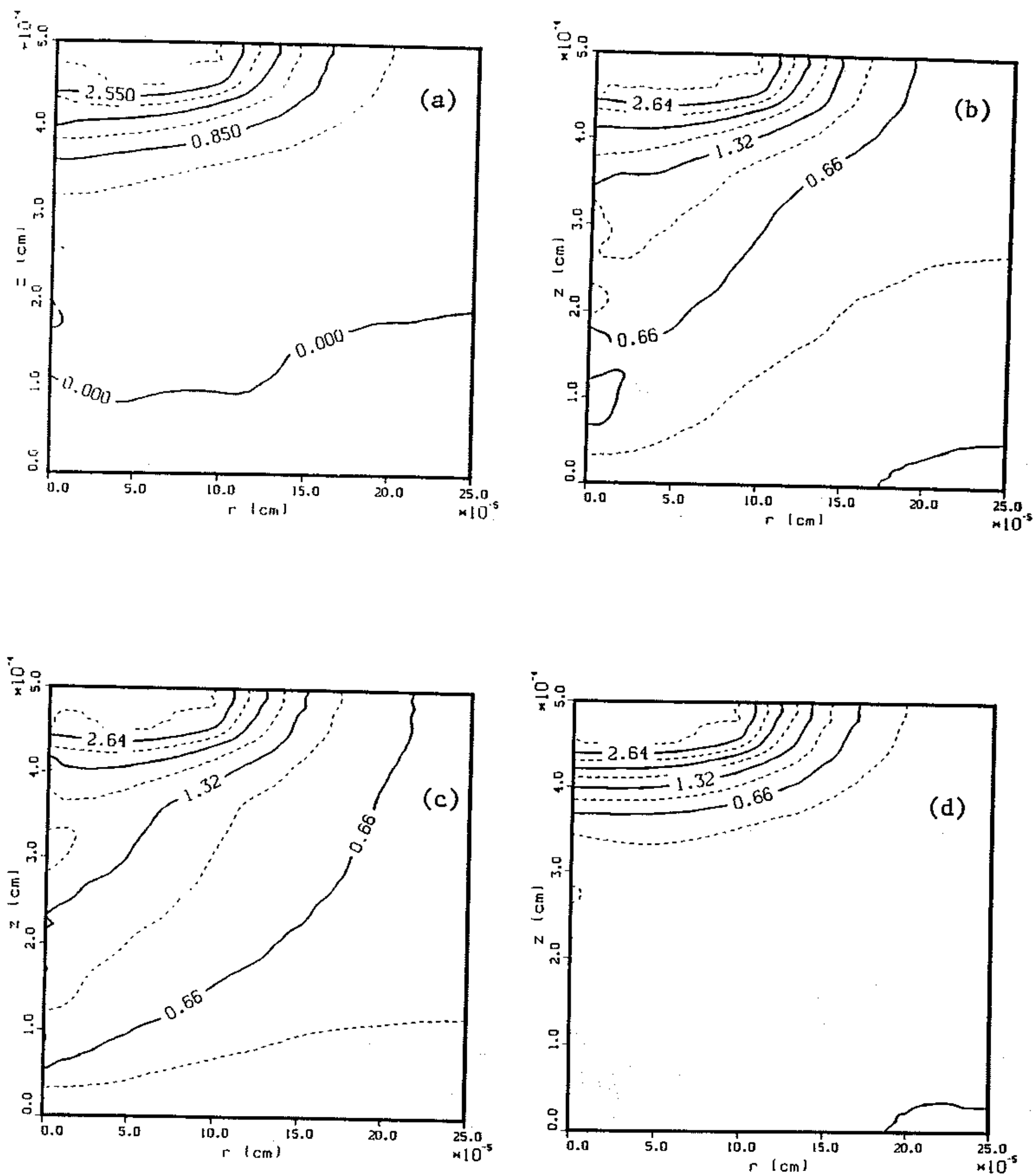

Figure 7.4: Contour plots of potential profile evolution with time, similar to Figure 7.3, at (a) 2.5 ps, (b) 30 ps, (c) 70 ps, and (d) 240 ps. Each contour line in (a) represents 0.425 volt change in potential, and each line in (b), (c), and (d) represents 0.33 volt change in potential.

the track electrons and holes remaining in the bulk of the device can only decay by diffusion to the contacts or by recombination over time. Figure 7.5 shows the 3-D potential profiles at different times from the simulation of Kreskovsky and Grubin [7.1]. Comparison with Figure 7.3 shows quite good agreement between our simulation and theirs.

Figure 7.6 shows the integrated collected charge [Q(t)] at the n^+-contact over time for our simulation, and Figure 7.7 shows that collected at the ground contact. Simultaneous generation of track electrons and holes within the n^+-contact initially generates a small hole current, as suggested by Figure 7.6. As the track ends 0.5 μm from the ground contact, no appreciable electron charge escapes from the ground contact as seen in Figure 7.7. Because the track is more influenced by electric-field-induced drift toward the n^+-contact than toward ground, collection of electron charge from the track is largely complete by 800 ps, but hole collection is only half complete.

Figure 7.8 shows the magnitude of Q(t) at the n^+-contact with time for our axisymmetric 3-D simulation vs. the 2-D and 3-D simulations from Reference [7.1]. Only the collected electrons are represented in this figure for our results; unlike our results, Kreskovsky and Grubin mention no minority carrier collection from the n^+-contact with their numerical method. As might be expected, our axisymmetric results are intermediate between 2-D and full 3-D results. The only qualitative difference with our results is the initial lag in rate of charge collection; potential gradients are

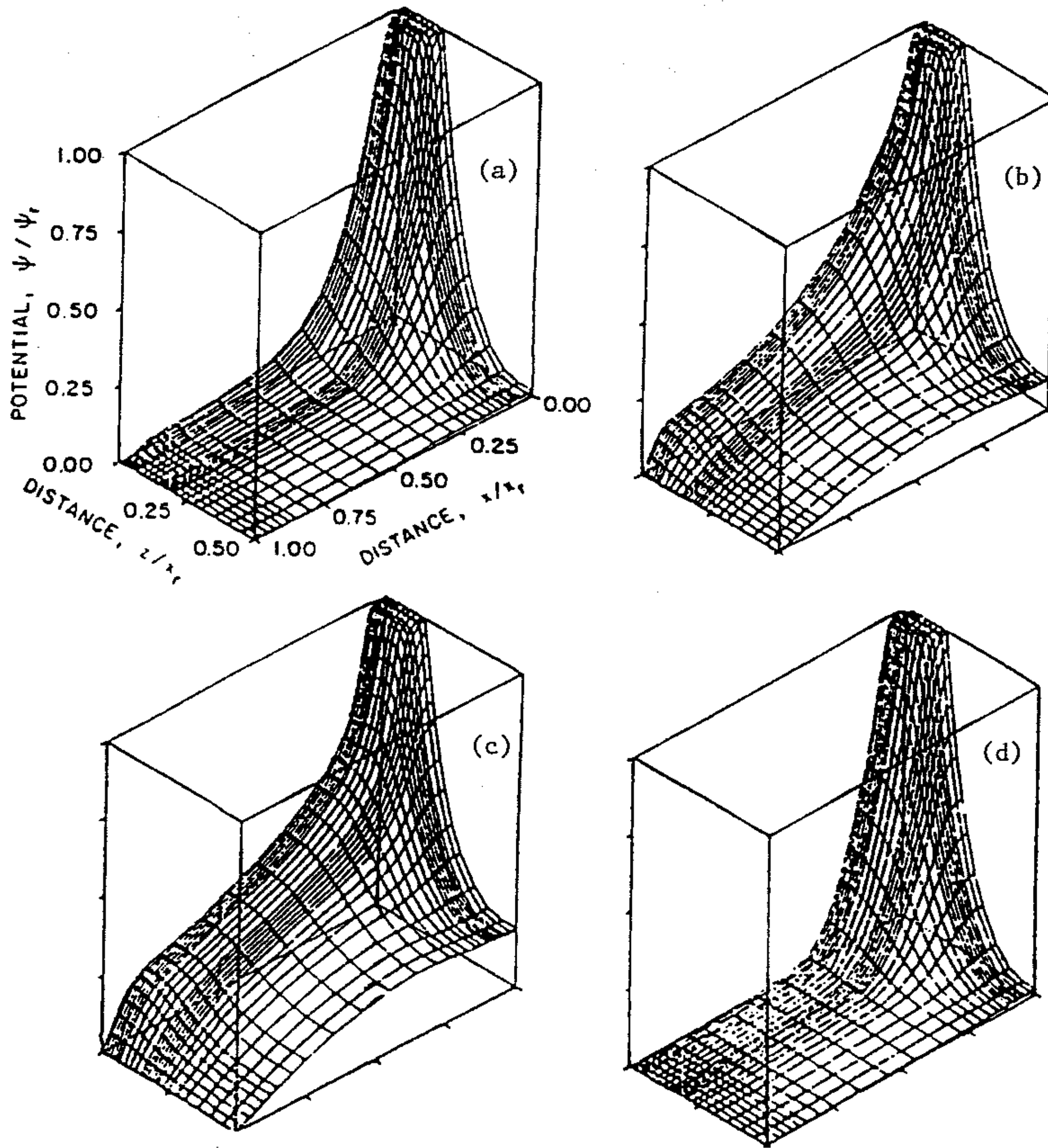

Figure 7.5: Evolution of 3-D potential profile with time for Kreskovsky and Grubin simulation [7.1], after introduction of ion track with identical geometry as that in Figures 7.1 to 7.4, at (a) 2.5 ps, (b) 14 ps, (c) 38 ps, and (d) 290 ps.

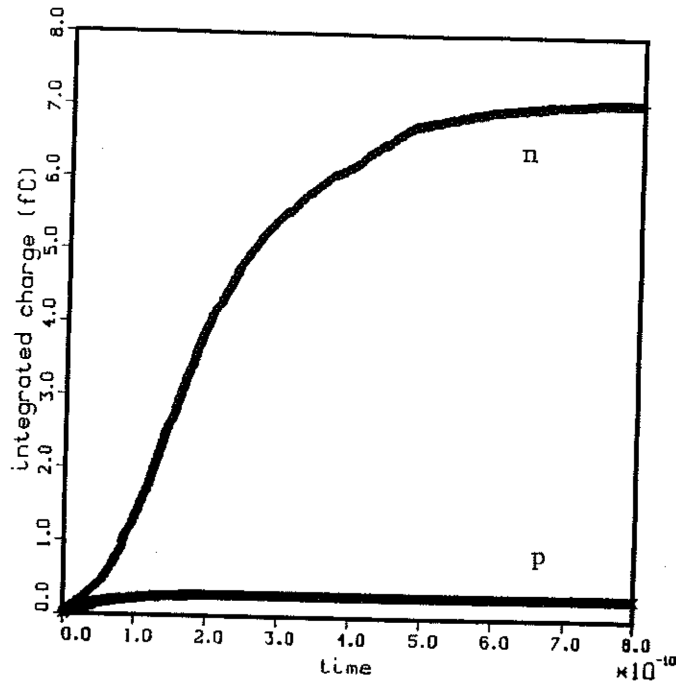

Figure 7.6: Integrated collection of track charge at n^+-contact vs. time for electrons (n) and holes (p).

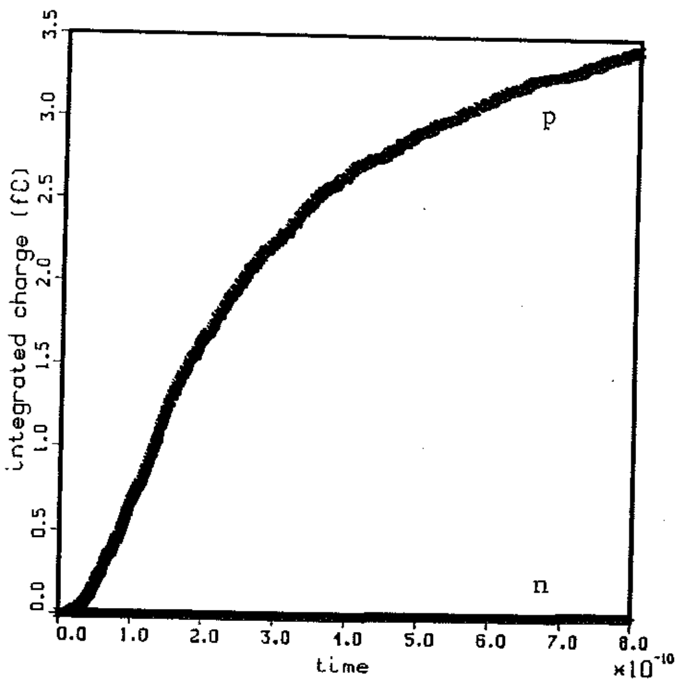

Figure 7.7: Integrated collection of track charge at ground contact vs. time for electrons (n) and holes (p).

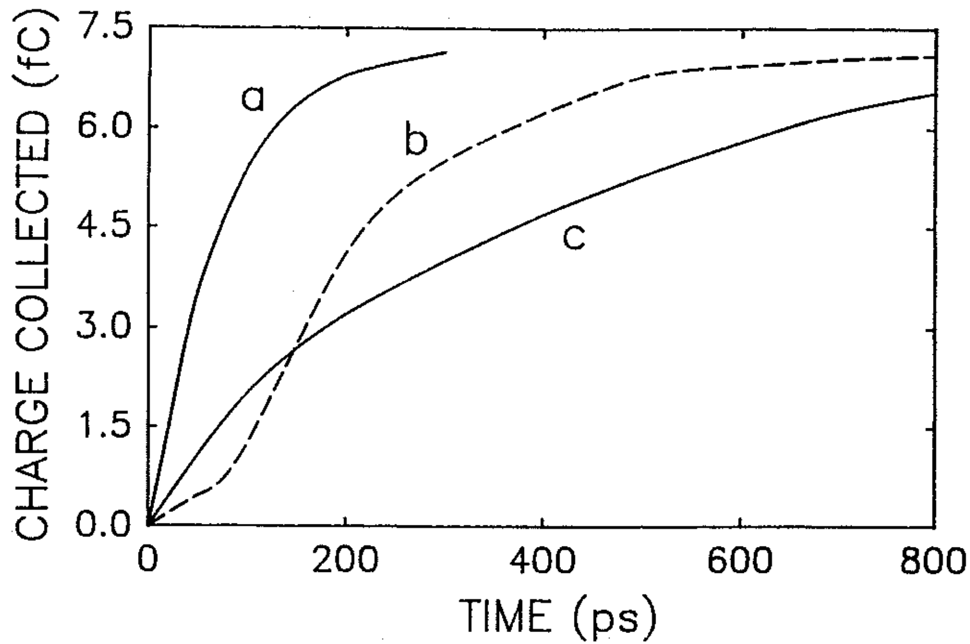

Figure 7.8: Integrated collection of track electron charge at n^+-contact vs. time for (a) 3-D simulation [7.1], (b) axisymmetric 3-D FE/PS simulation, and (c) 2-D simulation [7.1].

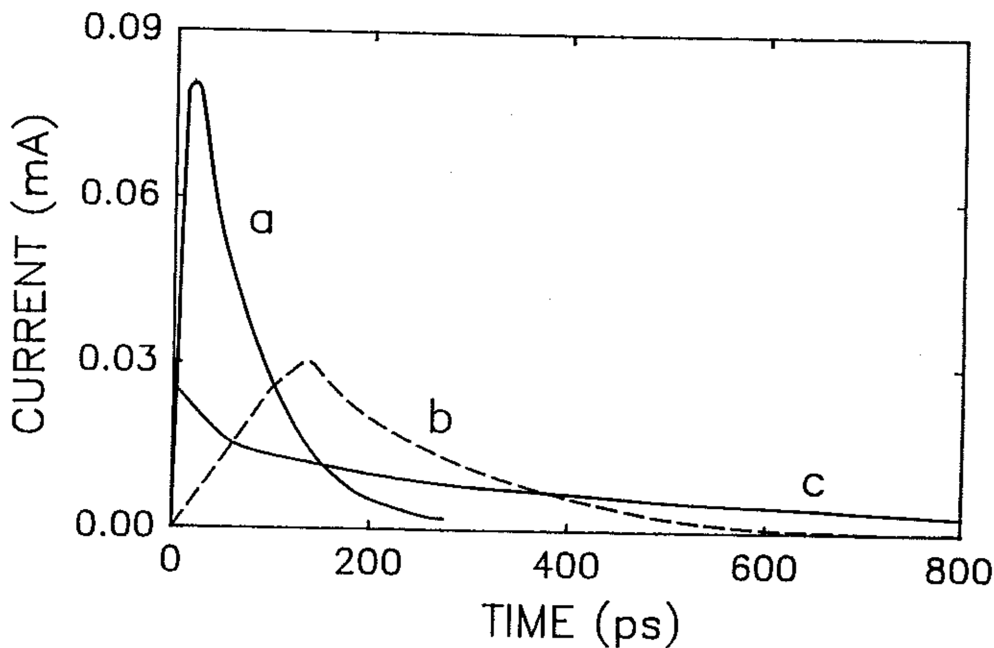

Figure 7.9: Track electron current at n^+-contact vs. time for (a) 3-D simulation [7.1], (b) axisymmetric 3-D FE/PS simulation, and (c) 2-D simulation [7.1].

suppressed within the heavily-doped 0.5 μm n^+-contact, so electrons can drift toward the n^+-contact but then must escape across the device boundary by diffusion. Figure 7.9 compares the transient current from our track electrons at the n^+-contact with the other simulation. Although our current peak occurs at about 135 ps rather than tens of picoseconds for Kreskovsky and Grubin's 3-D simulation, the qualitative features of our current peak are apparent unlike their 2-D simulation.

Although differences in the two numerical approaches should provide some difference in results, we can conclude that our axisymmetric 2-D method qualitatively captures the main features of a full 3-D simulation without the rigorous computational requirements of the third dimension, and gives more realistic results than a simple 2-D simulation. Although Figure 7.9 shows our transient current peak occurs at longer time frames than both the 2-D and 3-D results, we cannot conclude that our results are less realistic. Rather, in comparing these results to actual transient charge collection experiments [7.3], our results for time to peak current are in much better agreement with the 100 to 200 ps time frame apparent from the experiments than are Kreskovsky and Grubin's results.

These results show our numerical method to be successful in reproducing the predominant phenomena of ion hits on diode structures. We observe the field funneling effect as do other simulations, and we observe eventual pinchoff of the charge track at the depletion zone coupled with radial diffusion of the track into

the p-region. This track behavior is in good qualitative agreement with another simulation by Zoutendyk et al. using the axisymmetric PISCES device simulation code, which also presented contour plots of these pinchoff and radial diffusion effects [7.4].

Another capability of our code which will be demonstrated in more detail in Section 7.3 is the simulation of carrier recombination with time within the track. Although the magnitude of recombination is not significant in this simulation due to the relatively low track density, carrier recombination does become very significant as a charge removal mechanism for more realistic tracks with densities approaching 10^{20} cm^{-3}. This track phenomenon has not been given the significance it deserves in SEU simulations because of the numerical limitations of other methods in simulating high-density ion tracks.

Reference [7.1] mentions their 3-D simulation to 300 ps took 3.4 hours of central processing unit (cpu) time on a CRAY-1 computer, corresponding to 0.002 cpu seconds per grid point per time step (17,500 grid points, 350 time steps). Our axisymmetric 3-D simulation compares favorably with this, taking 98 cpu minutes on a CRAY-2 computer for a simulation to 800 ps, corresponding to 0.00083 cpu seconds per grid point per time step (1960 grid points, 3600 time steps). A 300 ps simulation by our method would have taken approximately one hour of CRAY-2 cpu time. The output of CRAY-1 vs. CRAY-2 computer per cpu minute is approximately comparable. In our simulation we initially used a 0.05 ps time step and gradually increased it to 0.4 ps, while Kreskovsky and Grubin began with a time step of 0.05 ps and ended with 1.25 ps.

7.2 Effect of Time Step on Charge Collection

We typically use a time step (Δt) of 0.05 to 0.1 ps in the initial stage of transient simulations, based on experience and others' recommendations [7.5], but the effect of Δt on transient simulations requires consideration. As discussed in Section 5.5, a time step on the order of the dielectric relaxation time is recommended. Use of $\Delta t = 0.05$ ps adheres to this criterion up to densities of about 10^{17} cm^{-3}. Densities of 10^{18} cm^{-3} and above would require Δt in the femtosecond range, a requirement too demanding for reasonable computational times. A practical approach is a choice of Δt which provides reasonable results with acceptable cpu time requirements, as Kreskovsky and Grubin did with their large (>1 ps) time steps in the latter stages of transient simulations [7.1].

To test the effect of Δt on transient charge collection from an ion track, we repeated the simulation of Section 7.1 over the first 50 ps with several values of Δt: 0.05, 0.1, 0.2, 0.4, and 0.8 ps. The integrated collection of electron charge at the n^+-contact over time is plotted for each case in Figure 7.10. Values for Δt of 0.05 and 0.1 ps gave similar results, but the larger values resulted in about a 20% decrease in collected charge after 50 ps.

A choice of Δt which is too large can induce potential and density oscillations [7.6]. We have found from experience that use of large Δt will enhance potential perturbations, especially at the device axis where charge fluctuations have the greatest relative effect. During these charge collection simulations, we also

monitored the potential fluctuations and tabulated the minimum and maximum potential values calculated during each simulation. The results are plotted in Figure 7.11. The potential values at $\Delta t = 0$ correspond to the steady-state potentials at the contacts. The trend is apparent: choice of Δt approaching 1 ps induces much greater potential perturbations during initial ion-induced transients. From this we conclude that a choice of Δt from 0.05 to 0.1 ps during strong transient conditions is a reasonable choice with respect to stability of results and adherence to the dielectric relaxation time criterion.

7.3 Modeling of the Transient Current Pulse

As discussed in Section 3.2, Messenger proposed an analytical equation to model the transient current pulse (I_t) as a combination of two exponential terms [7.7]:

$$I_t = I_o \, [\exp(-\alpha t) - \exp(-\beta t)] \quad , \tag{7.1}$$

with α^{-1} representing the collection time constant of the junction, and β^{-1} representing the ion track generation time constant (with $\beta > 10^{11}\ s^{-1}$). According to equation (3.4), $\alpha \approx 1.5 \times 10^{11}\ s^{-1}$ for a (substrate) doping density of $10^{15}\ cm^{-3}$. This representation of I_t has been generally accepted by the radiation effects community. For example, Wagner et al. [7.3] have attempted to model the results from their charge collection experiments using the Messenger model.

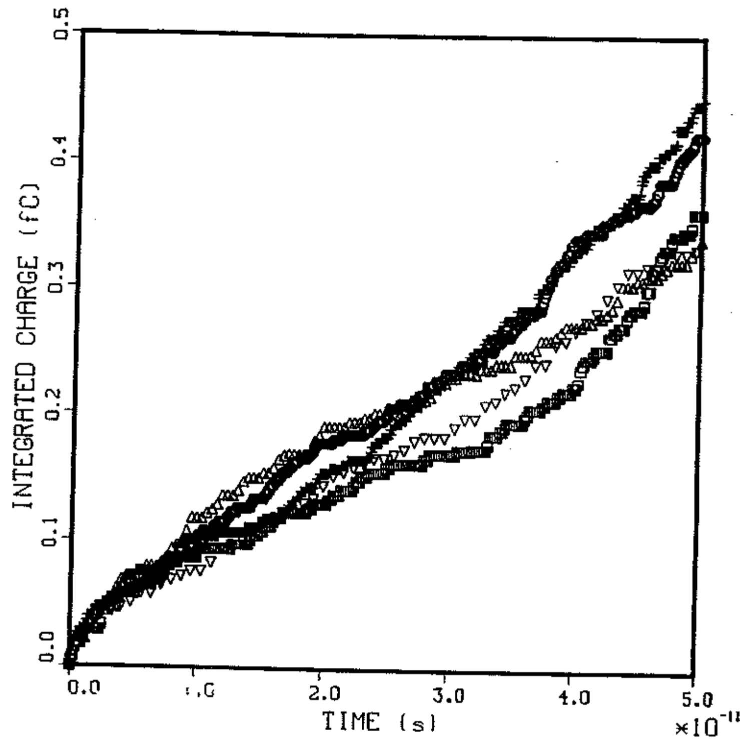

Figure 7.10: Integrated collection of track electron charge at n^+-contact vs. time for time steps of (+) 0.05 ps, (o) 0.10 ps, (□) 0.20 ps, (Δ) 0.40 ps, and (∇) 0.80 ps. Ion track is 4.5 μm long, 0.0565 μm in radius, with uniform density of 10^{18} cm^{-3}.

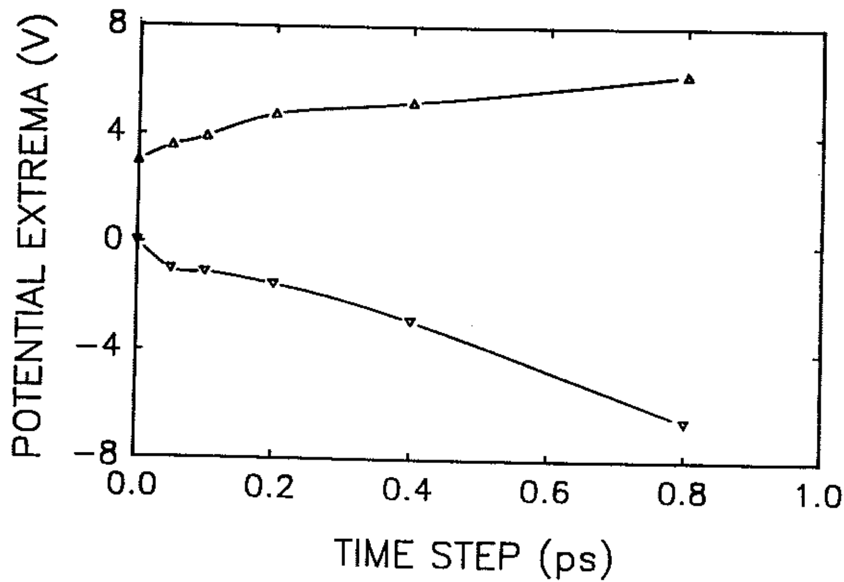

Figure 7.11: Maximum and minimum potential values as a function of time step for simulations of Figure 7.10.

With our detailed results in Section 7.1 for both I_t and integrated charge collection Q(t), we can test Messenger's model and obtain values for the track constants α and β by fitting the equation to our results for I_t in Figure 7.9. For engineering applications, development of a method by which α and β can be determined and tabulated as a function of ion species and energy, applied voltage, etc. would be very useful in SEU circuit simulations. Such an evaluation has not been conducted to date.

By integrating equation (7.1) with respect to time we can also obtain an analytical expression for Q(t) as a function of α and β:

$$Q(t) = I_o[\beta^{-1}(e^{-\beta t} - 1) + \alpha^{-1}(1 - e^{-\alpha t})] \quad . \qquad (7.2)$$

We have not seen any previous attempts to model results for both I_t and Q(t) and compare them for consistency.

When we attempted to parametrically determine α and β by fitting equations (7.1) and (7.2) to our data, we found an inconsistency in that a choice of α and β which gives us positive values of current will give us negative values for Q(t), and vice versa. We are not concerned here whether collected charge is positive or negative, so if the general exponential relationships expressed in equation (7.1) are reasonable, the coefficient I_o may not be correctly formulated.

As an alternative approach, we looked at the governing equations which represent the concentration of radioactive nuclei as a function of time for a radioactive decay chain. The general exponential relationships in such equations are analogous to those of equation

(7.1) but the pre-exponential term is more complex [7.8]. From this analogy, we propose the following empirical forms:

$$Q(t) = Q_o(\lambda_2 - \lambda_1)^{-1}[\lambda_1(e^{-\lambda_2 t} - 1) + \lambda_2(1 - e^{-\lambda_1 t})] \quad , \qquad (7.3)$$

and
$$I_t = \lambda_1\lambda_2 Q_o(\lambda_2 - \lambda_1)^{-1}(e^{-\lambda_1 t} - e^{-\lambda_2 t}) \quad , \qquad (7.4)$$

in which λ_1 and λ_2 are decay constants (inversely proportional to the half-lives) of the first two species in a radioactive decay chain. To convert equation (7.4) into a form analogous to equation (7.1), we replace λ_1 with β and λ_2 with α to obtain:

$$I_t = \alpha\beta Q_o(\beta - \alpha)^{-1}(e^{-\alpha t} - e^{-\beta t}) \quad . \qquad (7.5)$$

In this form, the pre-exponential coefficient is dependent on the total created charge as well as α and β, rather than simply representing a maximum current term as in equation (7.1). Likewise, we can convert equation (7.5) into the form:

$$Q(t) = Q_o(\beta - \alpha)^{-1}[\beta(1 - e^{-\alpha t}) + \alpha(e^{-\beta t} - 1)] \quad . \qquad (7.6)$$

When we applied equations (7.5) and (7.6) to represent our numerical data, we found consistent agreement with our computational results for both Q(t) and I_t for a judicious choice of values for α and β. For example, for $\alpha = 7.8 \times 10^9 \ s^{-1}$ and $\beta = 1.1 \times 10^{10} \ s^{-1}$, the analytical curves agree quite well with our computational results as shown in Figure 7.12 for Q(t) and Figure 7.13 for I_t. Positive to negative inversion of the curves from Messenger's model are apparent from the figures. By reversing the values of α and β, curve (c) in

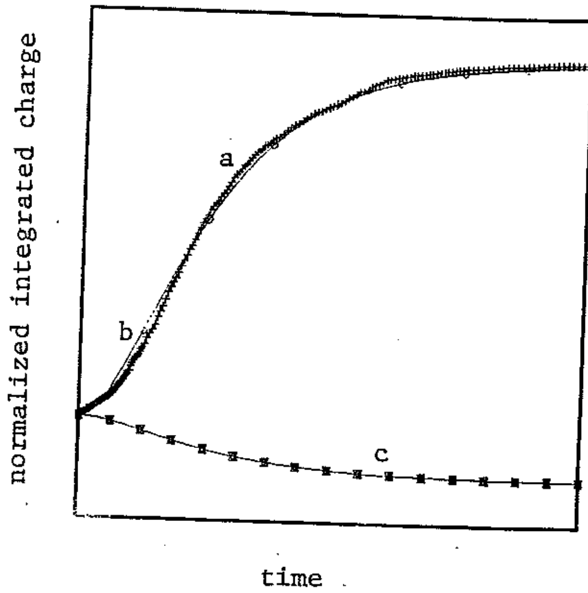

Figure 7.12: Comparison of results for integrated collection of track electron charge at n^+-contact vs. time, from (a) computational results, (b) radioactive decay model [7.8], and (c) Messenger model [7.7]. Identical constants used for both equations, for comparison.

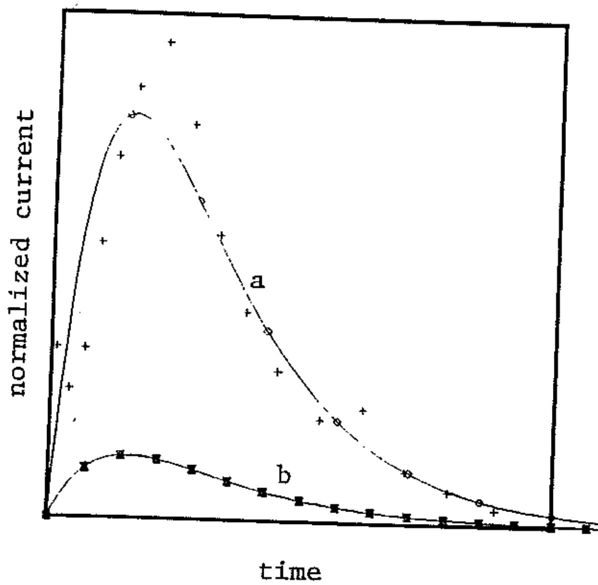

Figure 7.13: Comparison of results for electron current at n^+-contact vs. time, using (a) radioactive decay model [7.8], and (b) Messenger model [7.7]. Identical constants used for both equations, for comparison. Computational results given by (+).

Figure 7.12 takes on positive values while curve (b) of Figure 7.13 takes on negative values, but the curves obtained by the radioactive decay model remain fundamentally unchanged. From these results, we can conclude the pre-exponential term of equation (7.5) gives better consistency for Q(t) and I_t evaluations.

Although Messenger mentions that the value of β has little effect on subsequent transient calculations, we found β to have a significant effect on the time to peak current. This dependency raises questions about Messenger's explanation of β as related to the time for initial track formation because of the rapid development of the track relative to charge collection times. Another phenomenological explanation for α and β might relate to the time constants for drift of electrons to the n^+-contact and for their diffusive motion within the heavily-doped n^+-contact until their escape at the device boundary. Speculation as to the use of a third time constant to represent, e.g., the funneling time or the diffusion of charge carriers to the contacts after field restoration holds promise for more refined modeling of the transient current pulse. In Wagner et al.'s charge collection experiments, some delay time is apparent before the rapid increase in the current pulse [7.3]; they are not able to simulate this leading edge of the peak with the use of equation (7.1). By introducing a third time constant analogous to the radioactive decay equations, a better fit with the experimental data could be pursued.

Further study of these analytical representations for I_t vs. time holds promise for contributions to the radiation effects

engineering community both in terms of simple portrayal of transient current pulses within circuitry and in obtaining better understanding of the physical meaning and phenomena involved in these time constants. Use of our code to study Q(t) and I_t for different ions in different devices affords an ideal opportunity for future studies in this area.

7.4 Effects of Track Structure

To test the effects of track density on transient charge collection, we introduced tracks into a silicon diode for the same conditions as in Section 7.1, except that the track radius is now taken to be 0.1 μm and N_α of 10^{18}, 10^{19}, and 10^{20} cm^{-3} are introduced uniformly across the track width, for total track charges of electrons and holes of 0.0227 pC, 0.227 pC, and 2.27 pC, respectively. The density of 10^{20} cm^{-3} is higher than any reported track simulation, with only one simulation for N_α of 10^{19} cm^{-3} previously reported [7.9]. Simulations of 70 to 100 ps were conducted for parametric evaluations, using time steps of 0.05 to 0.1 ps and 5000 to 10,000 track particles.

Figure 7.14 shows the track electron and hole charge collection at the n^+-contact for the three cases. Although potential perturbations along the track axis become pronounced as the track density increases and considerably exceed the applied contact potentials for the largest densities, the curves for Q(t) show smooth profiles. Charge collection does not appear to be adversely

affected, as the perturbations develop within the interior of the device during track particle motion and charge separation. Our choice of direct matrix solution methods for Poisson's equation appears to be justified as the potentials do not continue to diverge despite the perturbations. Use of iterative solution methods would surely not guarantee convergence under these severe conditions. Time steps of 0.05 to 0.1 ps may also contribute to perturbations for the larger densities, as the criterion of dielectric relaxation time is violated more severely as densities increase. A track density of 10^{18} cm^{-3} should require a time step on the order of 0.01 ps according to this criterion as given in Section 5.5, and increasing

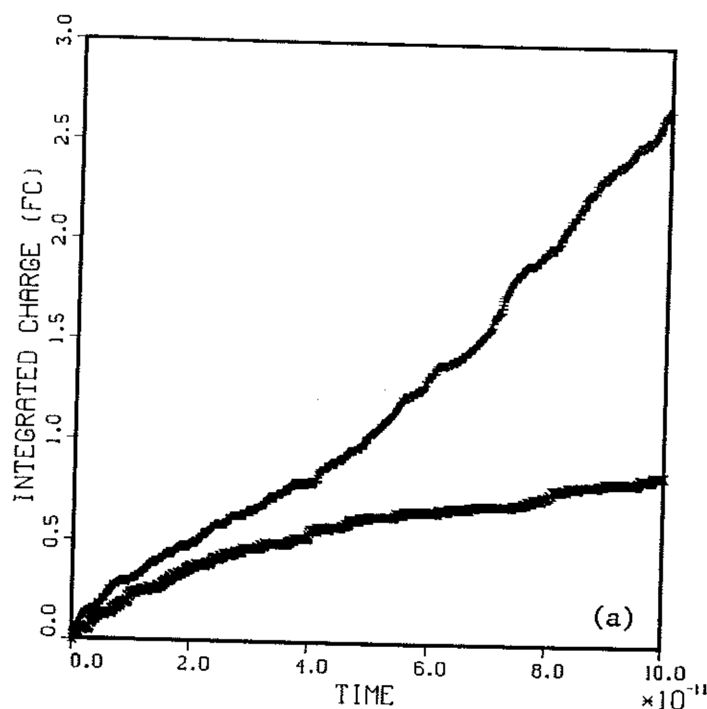

Figure 7.14: Integrated collection of track electron charge (n) and hole charge (p) at n^+-contact vs. time, for uniform track densities of (a) 10^{18} cm^{-3}, (b) 10^{19} cm^{-3}, and (c) 10^{20} cm^{-3}. Track is 4.5 μm long, with 0.1 μm radius.

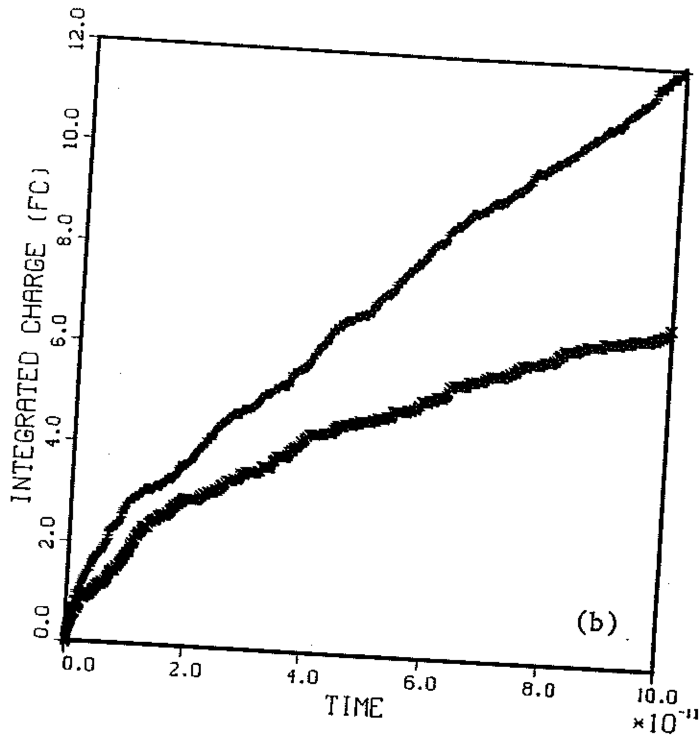

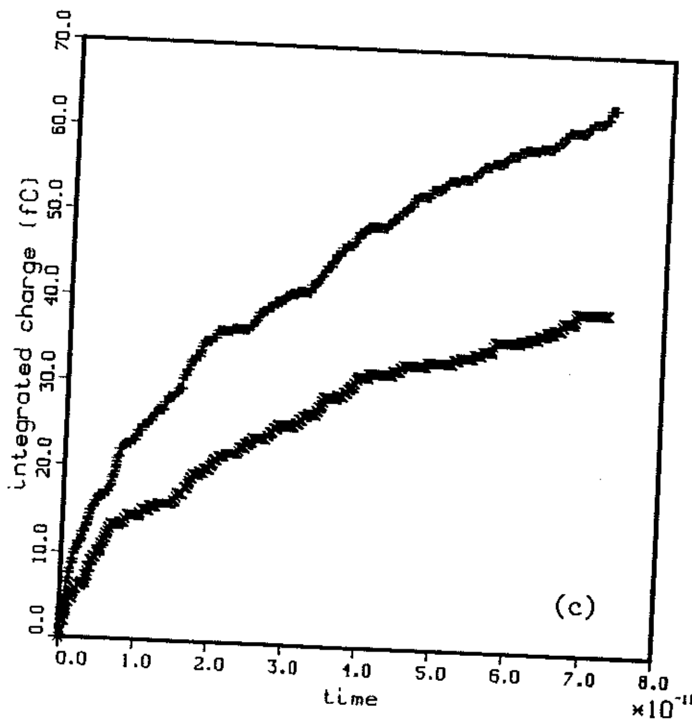

Figure 7.14: Integrated collection of track electron charge (n) and hole charge (p) at n^+-contact vs. time, for uniform track densities of (a) 10^{18} cm^{-3}, (b) 10^{19} cm^{-3}, and (c) 10^{20} cm^{-3}. Track is 4.5 μm long, with 0.1 μm radius.

the density by an order of magnitude should reduce the time step by an order of magnitude. Femtosecond time steps are computationally prohibitive, so some perturbation of potential must be tolerated at very large N_α as long as charge collection can be reasonably simulated.

Figure 7.15 normalizes the charge collection of Figure 7.14 by plotting the fraction of total charge collected with respect to the total track charge generated. Despite the tenfold increases in track charge, the fraction of charge collected over 70 ps actually decreases as N_α increases. This trend is explained by Figure 7.16, which gives the fraction of track charge recombining over time. For $N_\alpha = 10^{20}$ cm^{-3}, Auger recombination becomes very significant and dominates charge collection at the contacts as a charge removal mechanism. Auger recombination is not significant at $N_\alpha = 10^{18}$ cm^{-3}.

These effects of recombination for high-density ion tracks have not been studied in detail or seriously considered in SEU simulations. Auger recombination must be considered for SEU simulation of realistic tracks and heavy ions. Disregarding such details in simulations should give poorer agreement with experiment for heavier and more energetic ions.

In addition to demonstrating the importance of Auger recombination in SEU phenomena, these results demonstrate the ability of our numerical method to simulate realistic track densities up to 10^{20} cm^{-3}. Such densities represent a very difficult computational regime. The numerical approaches to SEU simulation employed up to

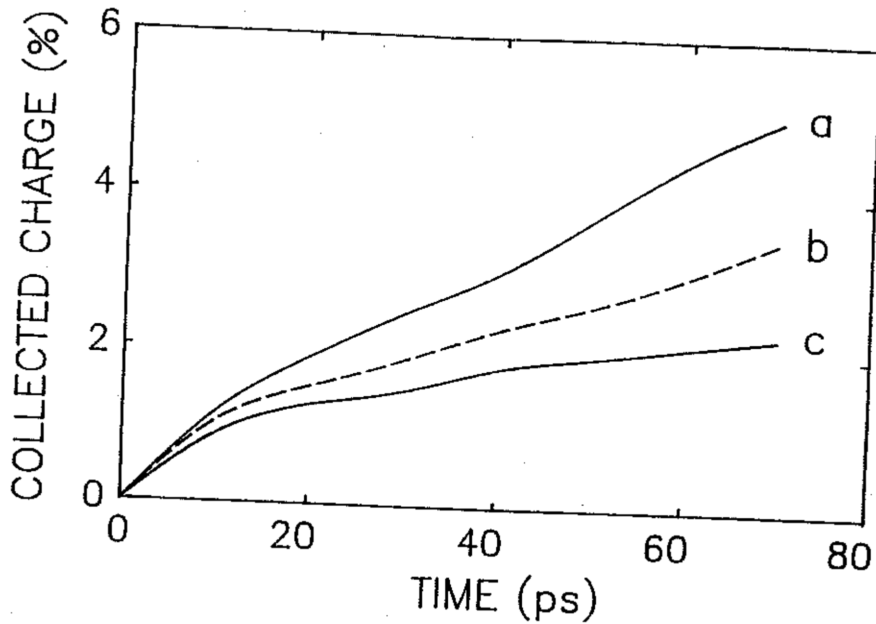

Figure 7.15: Fraction of total track charge collected at n^+-contact vs. time, for uniform track densities of (a) 10^{18} cm^{-3}, (b) 10^{19} cm^{-3}, and (c) 10^{20} cm^{-3}. Track is 4.5 μm long, with 0.1 μm radius.

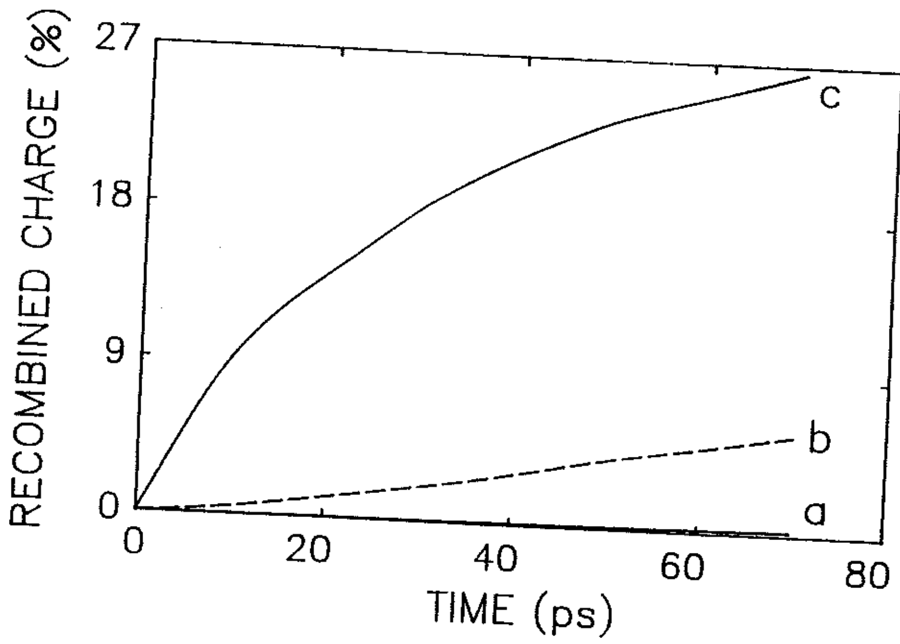

Figure 7.16: Fraction of total track charge recombined vs. time, for uniform track densities of (a) 10^{18} cm^{-3}, (b) 10^{19} cm^{-3}, and (c) 10^{20} cm^{-3}. Track is 4.5 μm long, with 0.1 μm radius.

the present have not been able to penetrate such a regime, and this simulation demonstrates a major strength of our method.

7.5 Simulation of Alpha Particle Effects

A simulation of charge collection from a 5 MeV alpha particle (helium ion) was performed using the device geometry of Figure 6.10: a 5 μm reverse-biased silicon diode. The initial track profile was obtained from TRIPOS-E. The core densities were approximately 10^{20} cm^{-3}, and decreased to 10^{15} to 10^{16} cm^{-3} at a radial distance of 0.1 μm. The ion penetrated through the length of the device. A test run was perfomed with a total diode voltage of 3 volts, then the applied voltage was increased to 15 volts, comparable to some charge collection experiments using silicon detectors.

The current pulse resulting from collection of track electrons at the n^+-contact for 15 volts reverse bias is shown in Figure 7.17. The current peak is very distinct, occurring at approximately 160 ps, with a maximum current on the order of 100 μA. As could be expected, the current peak for 3 volts reverse bias was not as sharp, with a maximum of about 50 μA at 200 ps.

These alpha-induced current pulses agree well with experiment. An experimental current pulse for a 5 MeV alpha particle is shown in Figure 7.18, in which a large silicon detector was used with a substrate of comparable doping to our simulation, but 25 volts reverse bias applied [7.10]. Comparison of Figures 7.17 and 7.18 show good agreement in all main features. Although our device

geometry and operating characteristics do not duplicate exactly the experimental parameters, our results give satisfactory agreement with the range of results from several experiments, as listed in Table 7.1. This duplication of experimental results provides confidence in our method, and gives better agreement with experimental ion-induced current pulses than other simulations of alpha-like tracks, e.g., reference [7.1].

Table 7.1. Comparison of FE/PS simulation results with experimental results for 5 MeV alpha particles.

device	substrate doping (cm^{-3})	applied voltage (volts)	time to current peak (ps)	maximum current (μA)	Ref.
large Si detector	1.4×10^{15}	25	148	180	[7.10]
CMOS n^+-contact in p-well	6×10^{15}	5	100	58	[7.11]
		10	96	89	
		15	108	148	
		20	112	212	
Si n^+-p diode	1×10^{15}	3	200	50	this work
		15	160	100	

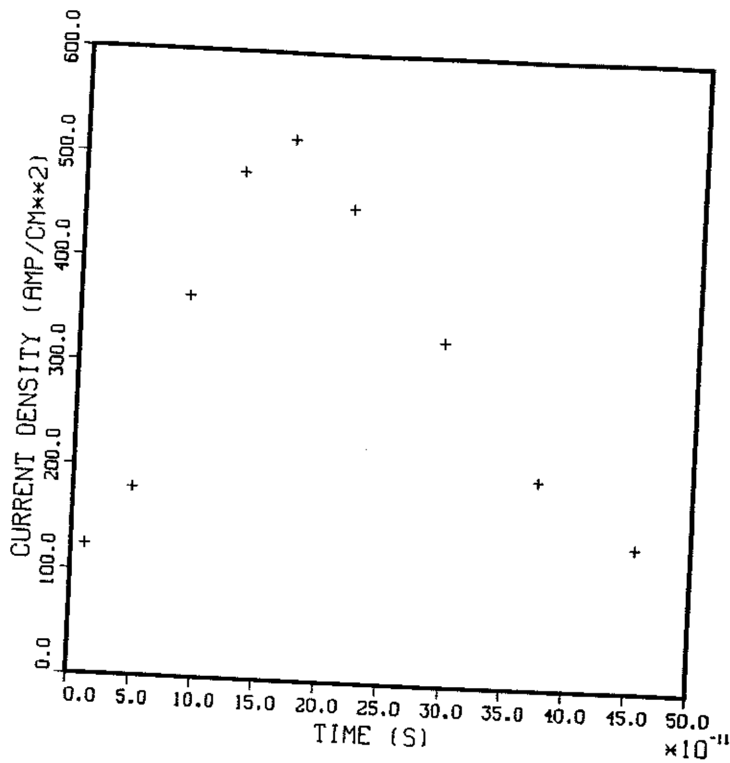

Figure 7.17: Track electron current vs. time at n^+-contact for 5 MeV alpha particle. 15 volts reverse-bias applied to 5 μm silicon diode.

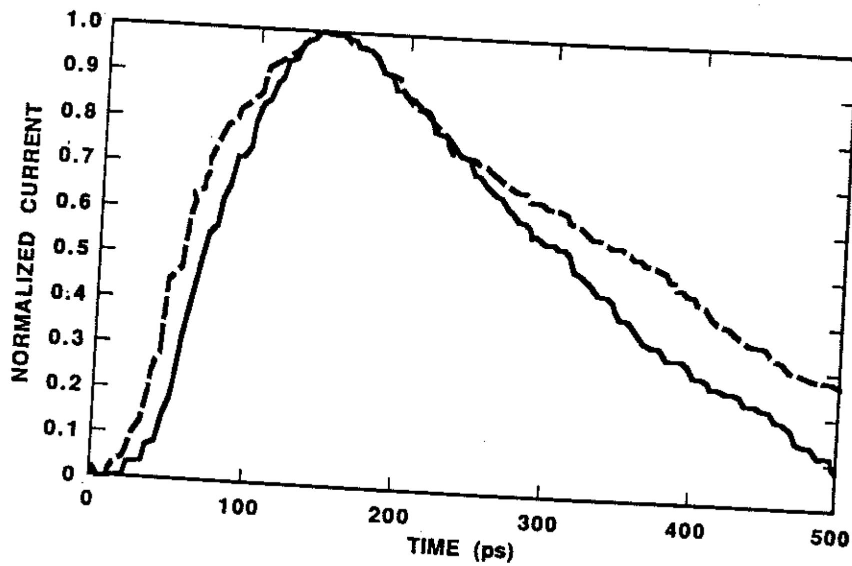

Figure 7.18: Experimental current pulses from 5 MeV alpha particle. Large silicon detector reverse-biased at 25 volts [7.10].

7.6 References

[7.1] J. P. Kreskovsky and H. L. Grubin, J. Comput. Phys., 68 (1987) 420.

[7.2] J. P. Kreskovsky and H. L. Grubin, Solid-St. Electron., 29 (1986) 505.

[7.3] R. S. Wagner, J. M. Bradley, N. Bordes, C. J. Maggiore, C. N. Sinha, and R. B. Hammond, IEEE Trans. Nucl. Sci., NS-34 (1987) 1240.

[7.4] J. A. Zoutendyk, H. R. Schwartz, and L. R. Nevill, IEEE Trans. Nucl. Sci., NS-35 (1988) 1644.

[7.5] D. Lippens, J.-L. Nieruchalski, and E. Constant, IEEE Trans. Electron Devices, ED-32 (1985) 2269.

[7.6] J. J. Barnes and R. J. Lomax, IEEE Trans. Electron Devices, ED-24 (1977) 1082.

[7.7] G. C. Messenger, IEEE Trans. Nucl. Sci., NS-29 (1982) 2024.

[7.8] I. Kaplan, Nuclear Physics, Addison-Wesley, Reading, Mass. 1963 (ch. 10).

[7.9] H. L. Grubin, J. P. Kreskovsky, and B. C. Weinberg, IEEE Trans. Nucl. Sci., NS-31 (1984) 1161.

[7.10] R. S. Wagner, N. Bordes, J. M. Bradley, C. J. Maggiore, A. R. Knudson, and A. B. Campbell, IEEE Trans. Nucl. Sci., NS-35 (1988) 1578.

[7.11] S. J. Heileman, W. R. Eisenstadt, R. M. Fox, R. S. Wagner, N. Bordes, and J. M. Bradley, IEEE Trans. Nucl. Sci., NS-26 (1989) 2287.

Chapter 8

SUMMARY AND CONCLUSIONS

The passage of energetic ions through semiconductor devices generates excess charge which can produce logic upset, memory change, and device damage. This single event upset phenomenon is increasingly important for satellite communications because of the high energy cosmic ion environment in space. The continuing reduction in semiconductor device sizes makes them more susceptible to ion-induced upset, and increases the probability of multiple-bit upset by single ions, a major concern for data error detection and correction techniques. For earth-based simulation of SEUs, cyclotrons are used to accelerate heavy ions until their LET characteristics are comparable to cosmic ions. However, the charge tracks for different ions may vary significantly in their profiles and widths, impacting the reliability of such testing.

Experimental and numerical simulation of SEUs is difficult because of the subnanosecond times and large charge densities within the ion track. Computational simulations typically employ simplified assumptions about the track profiles such as uniform density across the track. Track densities of 10^{18} cm^{-3} are usually assumed, with a track radius of 0.1 μm commonly used. Realistic peak densities within a track are expected to be in the range of 10^{20} cm^{-3}. Two-dimensional computer simulations tend to lose the detail of the transient current pulse, and ion track profiles and spreading are adversely affected. Three-dimensional simulations provide more

detail, but they are computationally expensive and do not necessarily provide results in good agreement with the time and duration of experimental ion-induced current pulses. Parametric evaluations of the transient current pulse as a function of ion energy and LET, applied device voltage, doping density, etc. would be useful for the development of engineering design equations for the use of the radiation effects community.

The objective of this work is twofold: (1) the determination of the track structure and electron-hole pair generation profiles following the passage of an energetic ion through silicon; (2) the development and application of a new numerical method for transient charge transport in semiconductor devices. By developing the methodology to determine detailed ion track profiles, we can achieve several objectives: a better understanding of the physics of track formation, evaluation of the comparability of cyclotron vs. cosmic ion track profiles, evaluation of the assumptions of track profiles frequently used as initial conditions for SEU computational simulations, and avoidance of these assumptions in our SEU simulations. By developing a numerical method specifically designed for transient simulations, we can pursue broader studies of the effects of ion and device parameters in simulations of SEU charge collection and transient current, and obtain better understanding of the physical phenomena involved in SEU effects.

A secondary electron generation and transport model, based on the Monte Carlo method, was developed and coupled to an ion transport code to simulate ion track formation in silicon. The result was the

TRIPOS-E code for coupled ion-electron transport. Secondary electrons are created using the binary collision approximation and slow down as a result of elastic and inelastic scattering, core electron ionization and dielectric energy loss, ultimately depositing energy and creating electron-hole pairs far from the ion's path.

TRIPOS-E results indicate an energetic ion leaves in its wake an exponential charge generation profile which can extend a significant fraction of a micron from the ion path, resulting in a track much wider than typically assumed. To model this profile, the previously-postulated Gaussian charge profile has been retained to represent the core of the charge track, but an exponential term has been added to reflect the track broadening resulting from the secondary electrons. Parameters have been evaluated to provide analytical expressions for the charge density profiles along the ion path. These expressions provide more detail compared to previous assumptions for radial charge profiles. Charge profiles obtained for cosmic ion tracks are found to differ significantly from those of cyclotron ions used in cosmic-effect simulations. The results from TRIPOS-E are used as input for the second part of our study, simulation of the transient charge transport and collection at device contacts.

A new numerical method is developed for the study of transient charge transport. The numerical method combines an axisymmetric quadratic finite-element formulation for the solution of Poisson's equation for the potential with particle simulation methods for electron and hole transport. The use of quadratic finite-element interpolation relaxes the restriction on maximum element size, and

provides continuity of the electric field across element boundaries. The axisymmetric formulation is ideal for studying the evolution of ion charge tracks as well as reducing the computational requirements for realistic results relative to full 3-D simulations.

This formulation offers several advantages over previous finite element and particle simulation methods for semiconductor analysis, in addition to its capabilities for studying the evolution of device operation with time. The generality of the code is enhanced by simulation of the transport of both majority and minority carriers, and includes recombination and thermal generation effects. Decoupling Poisson's equation from the current continuity equations reduces the computational requirements for matrix solutions, but also simplifies the solution for highly nonequilibrium conditions which could prevent more conventional solution methods from achieving convergence.

To assess the finite element/particle simulation method, transient one-dimensional solutions for silicon diodes were compared to analytical solutions and to a fully iterative finite-element method based on conventional solution methods, and good agreement was obtained between the different methods. Simulations of charge collection from ion tracks in 3-D axisymmetric devices were performed and compared to a previous simulation, with good agreement obtained and all significant features of the SEU phenomenon reproduced: potential field distortion, transient current pulse, and field restoration as the track decays.

The finite element/particle simulation method enables us to simulate larger ion track densities than previously reported, permitting study of more realistic track profiles and evaluation of recombination effects. Charge track densities as high as 10^{20} cm^{-3} have been simulated, one to two orders of magnitude higher than previously reported. Carrier recombination effects become very significant in this regime, a factor that has not received emphasis in previous simulations which have typically assumed track densities of 10^{18} cm^{-3}. This method allows quantification of the effects of recombination: at track densities of 10^{19} cm^{-3}, loss of transient charge by recombination can be comparable to charge collection at the contacts, and at 10^{20} cm^{-3} recombination is predominant.

The results of this work for transient current pulses following charged ion passage are in agreement with recent experimental data with respect to the time frame and magnitude of the current pulse. Our time frame for the current pulse gives better agreement with experiment than many SEU simulations which show peak current occurring in tens of picoseconds. Experiments indicate times to peak current are typically in the range of 100 to 200 ps. These simulation results are used in the development of simple analytical equations for circuit design to represent the current pulse and integrated charge collection from the ion track. These design equations may represent improvement over commonly accepted analytical representations of the transient current pulse.

The finite element/particle simulation method offers versatility in the simulation of transient device conditions and in studies of

the physics of nonequilibrium transport. The effects of processing and device variables on the SEU response can be addressed with the present method. TRIPOS-E holds promise for future studies of radiation track formation and electron-and charged-particle-induced radiation effects in semiconductor and other materials. This FE/PS method shows promise for further studies of radiation effects in materials other than semiconductors, and specifically for studies of the physical and chemical evolution of track structures and subsequent radiation-induced phenomena in a variety of materials.